Aerodynamic Databank Modeling

for Development of a Short-Haul Electric Airliner

Master's thesis in Applied Mechanics

ANNA JOHANSSON

DEPARTMENT OF MECHANICS AND MARITIME SCIENCES

CHALMERS UNIVERSITY OF TECHNOLOGY
Gothenburg, Sweden 2022
www.chalmers.se

Master's thesis 2022

Aerodynamic Databank Modeling

for Development of a Short-Haul Electric Airliner

ANNA JOHANSSON

CHALMERS
UNIVERSITY OF TECHNOLOGY

Department of Mechanics and Maritime Sciences
Division of Fluid Dynamics
Chalmers University of Technology
Gothenburg, Sweden 2022

Aerodynamic Databank Modeling
for Development of a Short-Haul Electric Airliner
ANNA JOHANSSON

Supervisor: André Gama de Almeida, Head of Flight Science, Heart Aerospace
Examiner: Lars Davidson, Professor at Department of Mechanics and Maritime Sciences, Division of Fluid Dynamics

Master's Thesis 2022:54
Department of Mechanics and Maritime Sciences
Division of Fluid Dynamics
Chalmers University of Technology
SE-412 96 Gothenburg
Telephone +46 31 772 1000

Cover: The ES-19.

Typeset in LaTeX
Printed by Chalmers Reproservice
Gothenburg, Sweden 2022

Aerodynamic Databank Modeling
for Development of a Short-Haul Electric Airliner
ANNA JOHANSSON
Department of Mechanics and Maritime Sciences
Chalmers University of Technology

Abstract

To the support development of a new airplane, an aerodynamic databank model was developed. The airplane's performance, stability, control, and handling qualities are analyzed by using a six degrees of freedom airplane model. One of the subsystems to this flight simulation model is the aerodynamic databank model which provides the aerodynamic forces and moments acting on the airplane. Essentially, the aerodynamic databank model is composed of different contributions to the six total aerodynamic coefficients which determine the loads on the airplane. This component buildup method gives a modular architecture of the databank model and makes it easy to add aerodynamic effects to specific airplane components and aerodynamic coefficients. The total aerodynamic coefficients are the aggregate of the coefficient contributions of individual airplane components due to the relevant aerodynamic effects. In general, the aerodynamic coefficients are functions of a large number of variables, including the angle of attack, side slip angle, speed, deflection of flaps and control surfaces, deployment of landing gear, and proximity to the ground. To cover an entire arbitrary flight, the computational fluid dynamics (CFD) data is combined with mathematical, semi-empirical, and empirical methods for modeling additional aerodynamic effects which were not considered in the CFD simulations. In the design phase of the airplane, this approach is particularly advantageous as it reduces the computational cost related to CFD and allows for rapid evaluations of design updates.

Keywords: aerodynamic databank, aerodynamic modeling, flight dynamics, aircraft development, component buildup method, stability derivatives, aerodynamic coefficients, in-flight icing, electric airplane.

Acknowledgements

Firstly, I would like to thank Heart Aerospace for giving me the opportunity to conduct this master's thesis work in collaboration with the future of aviation. Thanks to my supervisor André Gama de Almeida for the guidance of this work. Thanks to Alexandre Antunes for the support with the CFD simulations. Thanks to Rodrigo Suguimati for support with the flight dynamics and modeling of the airplane aerodynamics. Thanks to the entire Flight Science team at Heart Aerospace for the outstanding crash course in aerospace engineering. Finally, thanks to my supervisor and examiner, Prof. Lars Davidson, and to all professors at Chalmers University of Technology for all knowledge and skills that I have gained during my five years at Chalmers.

Anna Johansson, Gothenburg, June 2022

List of Acronyms

Below is the list of acronyms that have been used throughout this thesis listed in alphabetical order.

AC	Aerodynamic Center
CFD	Computational Fluid Dynamics
CoG	Center of Gravity
CoP	Center of Pressure
DNS	Direct Numerical Simulation
ISA	International Standard Atmosphere
KCAS	Knots Calibrated Airspeed
LES	Large Eddy Simulation
LWC	Liquid Water Content
MAC	Mean Aerodynamic Chord
MOW	Minimum Operating Weight
MTOW	Maximum Takeoff Weight
MVD	Median Volume Diameter
RANS	Reynolds-Averaged Navier-Stokes
SLD	Supercooled Large Droplets
TAS	True Airspeed
VLM	Vortex Lattice Method
2D	Two-Dimensional
3D	Three-Dimensional
6DOF	Six Degrees of Freedom

Nomenclature

Below is the nomenclature of suffixes, sets, parameters, and variables that have been used throughout this thesis.

Suffixes

b	body reference frame
F	fin
G	in proximity to the ground
HT	horizontal tail
nac	nacelle
s	stability reference frame
tot	total
VT	vertical tail
W	wing
WB	wings and body

Sets

$\{X_b, Y_b, Z_b\}$	basis representing the body coordinate system
$\{X_s, Y_s, Z_s\}$	basis representing the stability coordinate system
$\{X_w, Y_w, Z_w\}$	basis representing the wind coordinate system

Parameters

$\left(\frac{\partial \alpha}{\partial \delta}\right)_f$	2D lift effectiveness parameter
$\frac{\Delta C_{n,p}}{\left(\frac{\partial \alpha}{\partial \delta}\right)_f \delta_f}$	effect of symmetric flap deflection
$\frac{\Delta C_{n,p}}{\theta}$	effect of linear wing twist on $C_{n,p}$

$\frac{\Delta C_{n,p}}{dC'_D/d\alpha}$	nonlinear contribution to $C_{n,p}$ due to the effects of flow separation over the wing at moderate to high lift coefficients
$(\Delta C_{r,p})_{drag}$	difference in roll damping derivative due to drag
$\frac{\Delta C_{r,r}}{\left(\frac{\partial\alpha}{\partial\delta}\right)_f \delta_f}$	effect of flap deflection on $C_{r,r}$
$\frac{\Delta C_{r,r}}{\Gamma}$	difference in $C_{r,r}$ due to dihedral
$\frac{\Delta C_{r,r}}{\theta}$	difference in $C_{r,r}$ due to wing twist
$(\Delta C_{r,r})_{C_L}$	correction factor used to extrapolate the potential flow values of $C_{r,r}$ to higher lift coefficients
Γ	dihedral angle (positive for wing tip above the plane of the root chord), Section 3.6
θ	wing twist between root and tip (negative for washout), Section 3.6
κ	the von Karman constant, Section 3.7
λ	taper ratio
$\Lambda_{c/4}$	sweepback angle of the wing quarter-chord line
$\frac{\partial\sigma_\alpha}{\partial(pb/V)}$	sidewash parameter
$\frac{\partial\sigma_W}{\partial(pb/V)}$	wing sidewash parameter
A	wing aspect ratio
b	wing span
b'_f	parameter, Section 3.5.10
b'_w	parameter, Section 3.5.10
$C_{D,0}$	zero-lift drag coefficient
$C_{D,gear,L=0}$	landing gear zero lift drag coefficient
$(C_{D,q})_0$	contribution to $C_{D,q}$ due to loading at zero angle of attack
C_f	skin friction coefficient
$\left(\frac{C_{n,p}}{C_L}\right)_{L=0,M=0}$	slope of the low-speed yawing moment due to rolling at zero lift
$\frac{(C_{n,r})_0}{C_{D,0}}$	contribution to $C_{n,r}$ due to wing drag at zero lift
$\frac{(C_{n,r})_v}{C_L^2}$	contribution to $C_{n,r}$ arising from lift-dependent drag due to trailing vortices
$(C_{r,r})_\Gamma$	dihedral contribution to $C_{r,r}$
$(C_{r,r})_\theta$	twist contribution to $C_{r,r}$
$\left(\frac{C_{r,r}}{C_L}\right)_{L=0,M=0}$	slope of low-speed rolling moment due to yawing at zero lift
$(\frac{C_{y,p}}{C_L})_{L=0,M=0}$	slope of the low-speed side force due to rolling at zero lift
c	chord length
$\overline{c}$	MAC length
c_r	wing root chord length

E	log law offset
e	1. span efficiency factor, Section 2.10
	2. Oswald efficiency factor, Section 2.10 and Section 2.11.1.1
FF	form factor
g	gravitational acceleration
h_F	fin height
K	drag polar factor, Section 3.5
K_1	factor, Section 3.6.3.2
K_2	factor, Section 3.6.3.2
K_3	factor, Section 3.6.3.2
$K_{performance}$	drag polar factor based on performance drag polar data
p_1	constant in polynomial, Section 3.5
p_2	constant in polynomial, Section 3.5
p_3	constant in polynomial, Section 3.5
r	constant, Section 2.11.1.1
S_F	fin planform area
S_{gear}	landing gear reference area
S_{HT}	horizontal tail planform area
S_H/S_W	ratio of horizontal tail area to wing area
S	reference area
S_W	wing reference area
S_{wet}	wetted area
W	airplane weight

Variables

α	angle of attack
$\dot{\alpha}$	time derivative of the angle of attack
α_{eff}	effective angle of attack
α_i	induced angle of attack
$\alpha_{L=0}$	angle of attack at zero lift
$\alpha_{l=0}$	2D angle of attack at zero lift
β	1. side slip angle
	2. Mach number parameter, Section 3.6

$\dot{\beta}$	time derivative of the side slip angle
$(\frac{\beta C_{r,p}}{\kappa})_{L=0}$	roll damping parameter at zero lift
Γ	circulation, Section 2.6 and Section 2.9.1
γ	vortex sheet strength
$\Delta(\Delta C_L)_{flap}$	factor accounting for effect of flap deflection
$\Delta\alpha$	difference in angle of attack
$\Delta\alpha_{\dot{\alpha}}$	difference in angle of attack due to rate of change of the angle of attack
$\Delta\alpha_{gust}$	difference in angle of attack due to wind gust
$\Delta\alpha_p$	difference in angle of attack due to roll rate
$\Delta\alpha_q$	difference in angle of attack of due to pitch rate
$\Delta\beta_{\dot{\beta}}$	difference in side slip angle due side slip rate
$\Delta\beta_{gust}$	difference in side slip angle due to wind gust
$\Delta\beta_p$	difference in side slip angle due to roll rate
$\Delta\beta_r$	difference in side slip angle due to yaw rate
$\Delta\epsilon$	difference in downwash
ΔC_D	difference in drag coefficient
$\Delta C_{D,\dot{\alpha}}$	difference in drag coefficient due to rate of change of the angle of attack
$(\Delta C_D)_{prop}$	difference in drag coefficient due to propeller effect
$(\Delta C_D)_q$	change in drag coefficient due to pitch rate
ΔC_L	difference in lift coefficient
$\Delta C_{L,\dot{\alpha}}$	difference in lift coefficient due to rate of change of the angle of attack
$C_{L,\dot{\beta}}$	difference in lift coefficient due to side slip rate
$\Delta C_{L,f}$	difference in lift coefficient due to flap deflection
$(\Delta C_L)_{prop}$	difference in lift coefficient due to propeller effect
$(\Delta C_L)_q$	difference in lift coefficient due to pitch rate
ΔC_m	difference in pitching moment coefficient
$\Delta C_{m,\dot{\alpha}}$	difference in pitching moment coefficient due to rate of change of the angle of attack
$(\Delta C_m)_{prop}$	difference in pitching moment coefficient due to propeller effect
$(\Delta C_m)_q$	difference in pitching moment coefficient due to pitch rate
ΔC_n	difference in yawing moment coefficient
$C_{n,\dot{\beta}}$	difference in yawing moment coefficient due to side slip rate

$(\Delta C_n)_p$	difference in yawing moment coefficient due to roll rate
$(\Delta C_n)_{prop}$	difference in yawing moment coefficient due to propeller effect
$(\Delta C_n)_r$	difference in yawing moment coefficient due to yaw rate
ΔC_r	difference in rolling moment coefficient
$(\Delta C_r)_p$	difference in rolling moment coefficient due to roll rate
$(\Delta C_r)_{prop}$	difference in rolling moment coefficient due to propeller effect
$(\Delta C_r)_r$	difference in rolling moment coefficient due to roll rate
ΔC_y	difference in side force coefficient
$C_{y,\dot{\beta}}$	difference in side force coefficient due to side slip rate
$(\Delta C_y)_p$	difference in side force coefficient due to roll rate
$(\Delta C_{y,p})_\Gamma$	difference in $C_{y,p}$ due to dihedral effect
$(\Delta C_y)_{prop}$	difference in side force coefficient due to propeller effect
$\Delta x_{HT\,ref}$	longitudinal distance from airplane's CoG to horizontal tail reference point
$\Delta x_{nac\,ref}$	longitudinal distance from airplane's CoG to nacelle reference point
$\Delta y_{nac\,ref}$	lateral distance from airplane's CoG to nacelle reference point
$\Delta z_{nac\,ref}$	vertical distance from airplane's CoG to nacelle reference point
$\Delta z_{VT\,ref}$	vertical distance from airplane's CoG to vertical tail reference point
δ_f	flap deflection angle
ϵ	downwash
Θ	first Euler angle
θ	angular location along airfoil surface, Section 2.6
κ	ratio of the 2D lift curve slope at appropriate Mach number to $2\pi/\beta$, Section 3.6
Λ_β	compressible sweep parameter
μ_∞	freestream dynamic viscosity
ρ_∞	freestream air density
σ	Prandtl interference coefficient
Φ	second Euler angle
ϕ	velocity potential
Ψ	third Euler angle
a_1	lift curve slope
$a_{1,0}$	spanwise average 2D lift curve slope of wing section normal to quarter-chord line
a_∞	freestream speed of sound

B	Mach number paramter
b_{eff}	effective wing span
C_D	drag coefficient
C'_D	viscous lift coefficient
$C_{D,0}$	wing profile drag, Section 3.6.11
$C_{D,\alpha}$	drag versus angle of attack slope
$C_{D,corrected}$	corrected drag coefficient
$C_{D,e}$	parasitic drag coefficient including parasitic drag of wing and pressure and friction drag of the other airplane components
$C_{D,gear}$	landing gear drag coefficient
$C_{D,i}$	induced drag coefficient
$C_{D,main\,gear}$	main gear drag coefficient
$C_{D,nose\,gear}$	nose gear drag coefficient
$C_{D,performance}$	drag coefficient based on performance drag polar data
$C_{D,q}$	derivative of the drag coefficient with respect to the pitch rate
$\frac{\partial C_{D,q}}{\partial \alpha_{WB}}$	angle of attack contribution to $C_{D,q}$
$\frac{\partial C_{D,q}}{\partial\left(\frac{qc}{2V}\right)}$	contribution to $C_{D,q}$ due to rate of change of pitch
$C_{D,V}$	speed damping
C_L	lift coefficient
$C_{L,\alpha}$	lift curve slope
$(C_{L,\alpha})_{L=0}$	lift curve slope at zero lift
$(C_{L,\alpha})_{C_L}$	lift curve slope at any C_L below stall
$C_{L,\dot{\alpha}}$	lift acceleration derivative
$C_{L,0}$	lift at zero angle of attack
$C_{L,f}$	lift coefficient including flap effects
$C_{L,q}$	derivative of the lift coefficient with respect to the pitch rate
$C_{L,V}$	lift versus speed slope
C_m	pitching moment coefficient
$C_{m,\alpha}$	pitch stiffness
$C_{m,\dot{\alpha}}$	derivative of the pitching moment coefficient with respect to the rate of change of the angle of attack
$C_{m,gear}$	landing gear pitching moment coefficient
$C_{m,q}$	pitch damping
$(C_{m,q})_{M\approx 0.2}$	low-speed pitch damping
$(C_{m,q})_{M>0.2}$	subsonic pitch damping

$C_{m,V}$	Mach tuck derivative
C_n	yawing moment coefficient
$C_{n,\beta}$	yaw stiffness
$C_{n,\dot{\beta}}$	yawing moment coefficient due to side slip rate
$C_{n,p}$	derivative of the yawing coefficient with respect to the roll rate
$\left(\frac{C_{n,p}}{C_L}\right)_0$	linear contribution to the wing contribution to $C_{n,p}$
$\left(\frac{C_{n,p}}{C_L}\right)_{L=0,M}$	slope of the yawing moment due to rolling at zero lift
$C_{n,r}$	yaw damping
$\frac{C_{n,r}}{C_{D,0}}$	low-speed profile drag yawing parameter
$\frac{C_{n,r}}{C_L^2}$	low-speed drag-due-to-lift yaw damping parameter
C_p	1. propeller power coefficient
	2. pressure coefficient
C_R	aerodynamic force coefficient
C_r	rolling moment coefficient
$C_{r,\beta}$	dihedral derivative
$C_{r,\dot{\beta}}$	rolling moment coefficient due to side slip rate
$C_{r,p}$	roll damping
$(C_{r,p})_{\Gamma=0,L=0}$	roll damping derivative of wing without dihedral
$\frac{(C_{r,p})_\Gamma}{(C_{r,p})_{\Gamma=0}}$	dihedral effect parameter
$\frac{(C_{r,p})_{C_D,L}}{C_L^2}$	drag-due-to-lift roll damping parameter
$C_{r,r}$	derivative of the rolling moment coefficient with respect to the yaw rate
$(C_{r,r})_f$	trailing edge flaps contribution to $C_{r,r}$
$(C_{r,r})_p$	planform contribution to $C_{r,r}$
C_y	side force coefficient
$C_{y,\beta}$	derivative of side force coefficient with respect to the side slip angle
$C_{y,\dot{\beta}}$	side force coefficient due to side slip rate
$C_{y,p}$	derivative of the side force coefficient with respect to the roll rate
$(\frac{C_{y,p}}{C_L})_{L=0,M}$	slope of the side force coefficient due to rolling at zero lift
$C_{y,r}$	derivative of the side force coefficient with respect to the yaw rate
c_d	2D drag coefficient
c_l	2D lift coefficient
$(c_{l,\alpha})_M$	2D lift curve slope at considered Mach number
dl	infinitely small section of vortex filament

ds	length of vortex sheet section
$\mathbf{dV}$	induced velocity
F	empirical correction factor
$F'_{D,i}$	lift-induced drag force per unit span
$F_{D,i}$	lift-induced drag force
F_D	drag force
$F_{D,induced}$	induced drag force
$F_{D,interference}$	interference drag force
$F_{D,parasitic}$	parasitic drag force
$F_{D,wave}$	wave drag force
F_L	lift force
F'_L	lift force per unit span
F_y	side force
H	height of the wing mean quarter-chord above ground
H_H	height of horizontal tail mean quarter-chord above ground
h	1. altitude
	2. perpendicular distance from vortex filament to reference point, Section 2.6
I_{xx}	mass moment of inertia about the roll axis
I_{yy}	mass moment of inertia about the pitch axis
I_{zz}	mass moment of inertia about the yaw axis
K	factor used for accounting for variation of profile drag with lift coefficient, Section 3.6
k	lift-induced drag coefficient factor
$L/L_0 - 1$	parameter accounting for ground effect on lift due to bound vortices
l_F	location of fin CoP measured normal to the parallel to the longitudinal body axis
l_{HT}	distance from quarter chord point of horizontal tail MAC to moment reference center
$l_{main\,gear}$	vertical distance from main gear CoP to wing reference point
$l_{nose\,gear}$	vertical distance from nose gear CoP to wing reference point
M_x	rolling moment
M_y	pitching moment
M_z	yawing moment
M	Mach number

M_∞	freestream Mach number
n	distance from wing apex to moment reference center measured in wing MAC
p	roll angular velocity
p_0	stagnation pressure
p_∞	freestream static pressure
q	pitch angular velocity
q_∞	freestream dynamic pressure
q_H/q_∞	effective dynamic pressure ratio
R	aerodynamic force
Re	Reynolds number
R_{WB}	rotation matrix from wing reference frame to body reference frame
R_{WS}	rotation matrix from wind reference frame to stability reference frame
r	1. yaw angular velocity
	2. distance from ds, Section 2.6
	3. parameter for ground effect on lift due to bound vortices, Section 3.5.10
$\mathbf{r}$	radius between **dl** and reference point
s	location on airfoil contour line
T	factor accounting for reduction of longitudinal velocity
TAS	true air speed
u	velocity in the x-direction
$\frac{\partial u}{\partial y}$	variation of the u-velocity with respect to the y-direction
V_∞	freestream velocity
V_S	stall speed
$\mathbf{v}$	flow velocity vector
v_{gust}	wind velocity in y-direction
w_{gust}	wind velocity in z-direction
x	1. x-location, Section 2.6
	2. variable in polynomial, Section 3.5
	3. parameter accounting for effects on lift due to trailing vortices, Section 3.5.10
	4. longitudinal distance measured along wake center line from wing root chord trailing edge, Section 3.5.10
$\overline{x}$	longitudinal distance from CoG to AC (positive for AC aft of CoG)

x_0	longitudinal distance from leading edge of aerodynamic mean chord to moment reference point (positive aft of leading edge of aerodynamic mean chord)
x_{AC}	1. distance between AC and wing apex, parallel to the MAC (positive for AC aft of wing apex), Section 3.5.10 and 3.6, methods from [1]
	2. longitudinal distance from leading edge of aerodynamic mean chord to wing AC, Section 3.6, methods from [2]
x_{CoG}	distance between CoG and quarter-chord point of wing MAC, parallel to MAC (positive for CoG aft of MAC)
x_E	x-coordinate of the airplane CoG with respect to some Earth-fixed coordinate system
x_{HT}	longitudinal distance from the quarter-chord point of the MAC of the horizontal tail measured parallel to the body axis (positive aft of the moment reference point)
y	y-location
y_0	spanwise location of airfoil section
y_E	y-coordinate of the airplane CoG with respect to some Earth-fixed coordinate system
y_{prop}	lateral distance from CoG to propeller AC
z	1. z-location, Section 2.6
	2. vertical distance from vortex sheet to quarter-chord point of MAC, Section 3.5.10
	3. vertical distance between the CoG and the wing root quarter-chord point (positive for CoG above wing root chord), Section 3.6
z_F	vertical distance between the longitudinal body axis and the CoP of the fin, measured normal to the longitudinal body axis
z_{prop}	vertical distance from CoG to propeller AC
$z_{r,\,F}$	height of fin root chord measured from longitudinal body axis in direction normal to it
z_w	half-width of wing wake

Contents

List of Figures

List of Tables

1
Introduction

This chapter gives an introduction to the study performed in this master's thesis work. It describes the background, problem, aim, and limitations of the study. A description of the airplane type that was considered in this study is also included in this chapter. Additionally, an outline is given as guidance to the reader.

1.1 Background

Air travel accounts for 2.4% of the global CO_2 emissions, of which 40% comes from short-haul flights [3]. In line with the objectives of the Paris agreement to limit global warming to 1.5 °C, the International Air Transport Association (IATA) member airlines have committed to achieve net-zero carbon emissions from their operations by 2050 [4]. Sweden aims to make all domestic flights fossil-free by 2030 [5], and by 2040, Norway is aiming for all its short-haul flights to be entirely electric [6]. Electric propulsion powered aircraft is of great importance in order to make sustainable air travel possible. This master's thesis work is conducted as a collaboration between Chalmers University of Technology and Heart Aerospace, which is a Swedish electric aviation startup aiming to electrify regional air travel.

Designing an airworthy, efficient, and competitive airplane requires understanding of the aerodynamics. Flight simulations require the aerodynamic forces and moments acting on the aircraft. Hence, the aerodynamic analysis must cover various flight conditions and airplane configurations, including e.g., different angles of attack and deflections of flaps and control surfaces. Due to temporal, economic, and computational power limitations, computational fluid dynamics (CFD) and wind tunnel testing are insufficient. Mathematical, semi-empirical, and empirical methods in combination with CFD and experimental data may however provide the required information to cover the aerodynamics of an extensive set of flight scenarios. This is the main idea behind this study.

1.2 Aim

The aim of this study is to develop an aerodynamic databank model to support the development of a new airplane. The databank should combine the CFD data with mathematical, semi-empirical, and empirical models of aerodynamic effects to calculate the total aerodynamic forces and moments for various flight conditions. It is a subsystem of a full six degrees of freedom (6DOF) model of the airplane. Flight

simulations based on the 6DOF model will be used for analysis of the performance, stability, control, and handling qualities of the airplane.

1.3 Limitations

This study covers only development of the aerodynamic databank model and not the entire 6DOF model of the airplane. Specifically, the analysis of the performance, stability, control, and handling qualities of the airplane is excluded from this study. The input and output data to and from the aerodynamic subsystem must however be structured such that it is compatible with the other subsystems of the 6DOF model. Furthermore, the CFD simulations of the air flow around the considered airplane, performed to obtain the aerodynamic coefficients of respective airplane component as well as of the total airplane, were not a part of this thesis. The temporal limitation of five months of this study affects the complexity of the aerodynamic databank model. For this reason, the calculation of the hinge moments based on CFD data as well as control derivatives are not included in this study. Furthermore, as the wind tunnel testing was not yet carried out at the time this study was conducted, these data was not included in the aerodynamic databank. Nevertheless, the level of breakdown and accuracy of the aerodynamic databank model should be adequate to support the development of a new airplane.

1.4 A short-haul electric airplane

The airplane type considered in this study is a fully electric airplane for commercial short-haul flights. The maximum operating airspeed is assumed to be 190 knots calibrated airspeed (KCAS), corresponding to approximately 350 kph. The electric propulsion system consists of four wing-mounted nacelles, each including an electric motor and a propeller. Furthermore, the airplane is assumed to have a high-wing configuration with high aspect ratio wings. The airplane's landing gear is retractable. To allow for operation on short runways and in regions with complex topography, the airplane is designed for short takeoff and landing operations and has a steep approach capability. The airplane is assumed to be certified to the European Aviation Safety Agency (EASA) CS-23 Level 4 certification standards. The maximum certified operating altitude is 20,000 ft, corresponding to approximately 6700 m.

1.5 Outline

In Chapter 2, the theories behind the flight dynamics and fluid dynamics relevant for this study are discussed. It also includes explanations of the theories behind the computer programs and software that is of importance in this study. A brief introduction to airplane stability and control is also included in Chapter 2, which provides understanding of the relevance of the aerodynamic derivatives. In Chapter 3, the methods that were used in this study are described. These includes the

architecture of the aerodynamic databank, data collection, postprocessing, interpolation and extrapolation, modeling of the aerodynamics, and prediction of the icing effects. In Chapter 4, the numerical results of the aerodynamic databank modeling performed in this study are presented, including curves of the aerodynamic coefficients considering the different aerodynamic effects, and the predicted icing effects. The results as well as the choice of methods are discussed in Chapter 5. In Chapter 6, the conclusions of this study are found.

2
Theory

In this chapter, flight dynamics and aerodynamics relevant for this study are discussed. Furthermore, the theories behind the computer programs and software that were used in this study are explained. An introduction to aircraft stability control is also given as a broader context of the aerodynamic derivatives. Finally, the physics related to in-flight icing is explained.

2.1 Flight dynamics and fluid dynamics

Flight dynamics is the science of an aircraft's orientation and control in three dimensions, associated with its six degrees of freedom. The primary problem to solve in flight dynamics is to determine the position and velocity of an aircraft at some arbitrary time. The equations of motion consist of nonlinear ordinary differential equations, referred to as the Newton-Euler equations. These are the governing equations of the flight dynamics. The solution of the Newton-Euler equations for the aircraft yields its 6DOF motion. The position and velocity variables are referred to as states of the aircraft and are the minimum set of variables which describe the aircraft's position, orientation, and velocity, and are seen in Table 2.1. The information that describes an aircraft's position and velocity is usually expressed relative to some external reference frame. The aerodynamic forces and moments are determined by the aircraft's position and velocity relative to the atmosphere.[7]

The Euler angles Θ, Φ, and Ψ are used to keep track of the orientation of the gravity vector relative to the aircraft body and do not need to be taken into consideration in this study. The variables x_E and y_E can also be ignored in this study since the location of the aircraft with respect to the Earth's surface does not affect the forces and moments acting on it. The altitude must be retained since it defines the atmospheric properties which affects the aerodynamic forces and moments.[7]

To accurately describe the forces and moments, also the rates of change of the angle of attack and side slip angle need to be accounted for. This is due to the fact that there is a time lag in the flow field as the angle of attack and side slip angle varies with time. In addition to the state variables, the effects of the flight controls needs to be considered as well as the thrust control. In flight dynamics, the aerodynamic forces and moments in particular create difficulties due to their complex dependencies on various quantities.[7]

Table 2.1: The state variables

Variable	Symbol
freestream velocity vector	V_∞
angle of attack	α
side slip angle	β
roll angular velocity	p
pitch angular velocity	q
yaw angular velocity	r
First Euler angle	Θ
Second Euler angle	Φ
Third Euler angle	Ψ
x-coordinate of the aircraft CoG with respect to some Earth-fixed coordinate system	x_E
y-coordinate of the aircraft CoG with respect to some Earth-fixed coordinate system	y_E
altitude	h

To evaluate an aircraft's performance and response to control inputs and to simulate a flight, the forces and moments acting on the aircraft, and their dependence on the flight variables, need to be determined. The forces acting on an aircraft in flight are the gravitational, propulsive, and aerodynamic forces. A force that does not act through the center of gravity (CoG) of the aircraft will generate a moment about the CoG.

The fluid dynamics, i.e., the air flow, is governed by the Navier-Stokes equations. In this study, the 6DOF rigid body dynamics and the fluid dynamics are decoupled. The aerodynamic forces and moments are computed for specific airplane orientations and velocities. These flow calculations are repeated for a large number of different airplane configurations, resulting in a comprehensive aerodynamic databank. The database can then be used to simulate a flight by using the Newton-Euler equations and continuously updating the aerodynamic loads from the databank.

2.2 Reference systems

The primary reference system used in the aerodynamic databank model is the wind reference frame. The aerodynamic forces and moments acting on the airplane are produced by the airplane's motion relative to the air and depend on the orientation of the airplane with respect to the airflow. Assuming that the gravity field is constant, the wind reference frame has its origin fixed to the CoG of the airplane. A Cartesian coordinate system given by the basis $\{X_w, Y_w, Z_w\}$ is defined by superimposing the X_w-axis to the relative velocity vector, see Figure 2.1. The Z_w-axis is

perpendicular to the X_w-axis in the plane of symmetry of the airplane and is positive in the downward direction. The Y_w-axis is determined by the right hand rule.[7]

The body-fixed Cartesian coordinate system given by the basis $\{X_b, Y_b, Z_b\}$ has its origin in the center of mass of the airplane. Assuming that the gravity field is constant, the center of mass coincides with the CoG. It is oriented such that the X_b-axis is aligned with the fuselage in the direction from the tail to the nose, the Y_b-axis points towards the pilot's right side of the airplane, and the Z_b-axis is normal to the airplane body and is directed downward, see Figure 2.1. The angle formed by the instantaneous direction of the relative velocity vector and its projection on the plane given by $\{X_b, Z_b\}$ gives the side slip angle, denoted by β. The plane given by $\{X_b, Z_b\}$ defines the plane of symmetry of the airplane.[7]

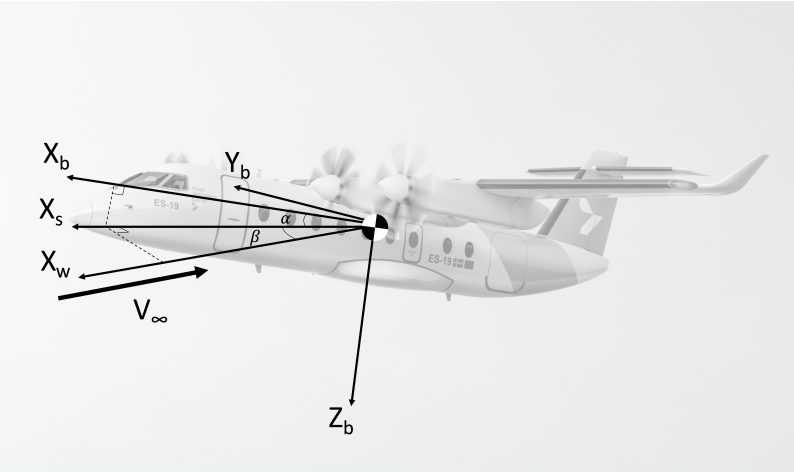

Figure 2.1: The airplane reference systems

The Cartesian stability coordinate system given by the basis $\{X_s, Y_s, Z_s\}$ is determined by the equilibrium flight condition and has the origin fixed to the aircraft's CoG. The X_s-axis is given by the instantaneous relative wind vector projected onto the , see Figure 2.1. The Y_s-axis points in the direction towards the pilot's right side of the airplane and coincides with the body axis Y_b. The Z_s-axis is given by the right hand rule and lies in the plane given by $\{X_b, Z_b\}$. The angle between the X_b and X_s is the airplane's angle of attack, denoted by α. If the relative velocity vector lies in airplane's plane of symmetry, i.e., in the case of no side slip, the wind axes coincide with the stability axes. The wind axes deviate from the stability axes when side slip is present.[7]

The rotations of the aircraft are defined using the terms roll, pitch, and yaw, which correspond to rotation about the X_b-axis, Y_b-axis, and Z_b-axis, respectively. The angular displacement of the aircraft about the X_b-axis is referred to as the bank angle. The pitch angle is the angular displacement about the Y_b-axis. The angle between the Y_b-axis and the nose of the airplane is the yaw angle, or the heading of the airplane.

The geometrical input to the databank is given in the structural reference system.

The origin is located near the nose of the airplane, the structural x-axis is parallel to the fuselage and points towards the tail, the structural y-axis points from the fuselage towards the pilot's right side of the airplane, and the structural z-axis points upwards.

2.3 Incompressible flow over airfoils

The wings, stabilizers, and propeller blades of an airplane feature airfoil-shaped cross-sections. The purpose of an airfoil is to change the air flow such that it generates a reaction force. Due to its streamlined shape, the airfoil is capable of producing significantly more lift than drag. Lift is the force that is produced by this dynamic effect of the air acting on the wings in the direction perpendicular to the freestream flow direction. In level flight, the lift force opposes the gravitational force. The lift force is always accompanied by a drag force, which is the component of the aerodynamic force parallel to the freestream flow direction.

As stated in [8], a streamline is a path traced out by a massless particle moving with the flow. Moreover, at every point along the streamline, the velocity is tangent to the path. Since the normal component of the velocity along the path is zero, mass cannot cross a streamline, i.e., the mass is constant throughout the flow field. Considering an airfoil, no mass can pass through its surface, hence the surface of the airfoil is a streamline. In [9], a streamlined body is defined as a body for which most of the drag is skin friction drag. By streamlining a body, the drag is reduced due to delayed boundary-layer separation and a smaller wake, which minimizes the pressure drag and decreases the skin friction drag.

For an airfoil, the angle of attack is defined as the angle between the airfoil chord line and the freestream velocity vector. At low to moderate angles of attack, the two-dimensional (2D) lift coefficient c_l varies linearly with the angle of attack. The slope of this straight line is called the lift slope. In this region, the flow is attached over most of the airfoil surface. As the angle of attack increases, viscous effects causes the flow to separate from the top surface of the airfoil. In the separated region the flow is recirculating. If the separation region is sufficiently large, it leads to a rapid decrease in lift and a large increase in drag and the airfoil is said to be stalled. The maximum lift occurs at the stall angle of attack.[10]

The fluid pressure is a scalar quantity related to the momentum of the molecules of a fluid. The far field stagnation pressure, also referred to as the total pressure, is defined as

$$p_0 = p_\infty + \frac{\rho_\infty V_\infty^2}{2}, \tag{2.1}$$

where p_∞ is the freestream static pressure, and V_∞ is the freestream velocity. This is Bernoulli's equation, assuming incompressible flow. The term associated with the velocity of the flow is referred to as the freestream dynamic pressure and is defined as

$$q_\infty = \frac{1}{2}\rho_\infty V_\infty^2, \tag{2.2}$$

where ρ_∞ is the density of the freestream flow.[11]

The flow that reaches the airfoil leading edge, stagnates. Accordning to Bernoulli's equation, the pressure at this point is equal to the total pressure. As the distance between the streamlines decreases, the continuity equation yields an increased flow velocity near the front surface of the upper airfoil surface and a decreased pressure. By the continuity equation, the maximum velocity is reached at the thickest point on the airfoil. Hence, the static pressure is at its minimum at this point. Behind this point, the velocity decreases and the static pressure increases until the flow reaches the trailing edge, where the static pressure equals the total pressure. Behind the trailing edge of the airfoil, the flow velocity increases until the freestream velocity and the freestream static pressure are reached.[9]

The lift force is determined by the difference in static pressure between the upper and lower airfoil surfaces. By tilting the airfoil at an angle of attack relative to the freestream, the pressure distribution becomes asymmetric between the upper and lower surfaces, which generates a lift force. In nature, the airflow over the airfoil is slightly different due to viscous and compressible effects. More specifically, the viscosity of the air gives rise to drag forces and reduces the lift force compared to the ideal fluid flow.[10]

The freestream Reynolds number is defined as

$$Re = \frac{\rho_\infty V_\infty c}{\mu_\infty}, \tag{2.3}$$

where c is the reference length taken as the chord length of the airfoil, and μ_∞ is the freestream dynamic viscosity. It is a dimensionless quantity defining the ratio of the inertial forces to the viscous forces in a flow. In general, flows with low Reynolds number are laminar and flows with high Reynolds number are turbulent. The inertial forces are due to a fluid's natural resistance to acceleration. The viscous forces are due to internal friction of the fluid. At low Reynolds numbers, the inertial forces are negligible compared to the viscous forces. At high Reynolds numbers, the viscous forces are instead much smaller than the inertial forces. Inviscid flow is approached as $Re \to \infty$.[9][10]

The surface roughness affects the flow field around the airfoil such that if the roughness is increased, the transition to turbulent flow occurs further upstream. However, at very high Reynolds numbers, the flow will be turbulent even though the surface roughness is low. The transition from laminar to turbulent flow is also affected by the pressure gradient. The static pressure of the flow over an airfoil decreases up to the point of maximum thickness, hence the flow will tend to remain laminar. Behind the point of maximum thickness, the static pressure increases and the flow may transit to turbulent flow before the leading edge.[9]

The no-slip condition states that the flow velocity is zero at the surface of the airplane. Within the boundary layer, where the fluid velocity is gradually increasing, friction is present due to the relative velocities between the fluid particles. This

force is referred to as the skin friction drag. At a certain distance away from the airplane, the velocity takes a constant value referred to as the freestream velocity. Near the airplane surface, a turbulent boundary layer has a greater gradient of the velocity in the x-direction with respect to the direction tangential to the freestream velocity direction, i.e., $\frac{\partial u}{\partial y}$. Furthermore, a turbulent boundary layer has a greater thickness compared to a laminar boundary layer. For most airplanes in flight, the boundary layer flow is turbulent over most of the airfoil except for near the leading edge. At low-speed subsonic flight, the shear force caused by viscous flow over the surface of the airplane, i.e., the skin friction force, is an important aerodynamic force. The skin friction force is strongly dependent on the Reynolds number. Laminar shear stress is smaller than turbulent shear stress, meaning that laminar flow yields a smaller skin friction force.[10]

In an ideal fluid (i.e., an inviscid fluid), the static pressure acting on the front surfaces of the airfoil, that is the region from the leading edge to the shoulder, parallel to the freestream is perfectly balanced by the static pressure acting on the rear surfaces of the airfoil. Considering a viscous fluid, this symmetry and cancellation of forces are no longer valid. The static pressure force acting on the front surfaces of the airfoil is greater than the static pressure force acting on the rear surfaces of the airfoil. This asymmetric pressure distribution, which causes the flow to separate, is referred to as pressure drag. Similarly, compared to an ideal fluid, the static pressure distribution in viscous flow gives a decrease in the lift.[9]

2.4 Governing equations of aerodynamics

The Euler equations are a set of coupled differential equations describing how the velocity, pressure and density of a moving fluid are related. In general, an equation of state that relates the pressure and the density of a fluid is required in order to solve the Euler equations. For a given flow problem, the Euler equations can be solved by using methods from calculus. These equations do not include effects of viscosity, hence a solution of the Euler equations is only an approximation to a real fluid flow problem. However, the lift of a thin airfoil at low angle of attack can be relatively accurately approximated by a solution of the Euler equations.[12]

The Navier-Stokes equations are extensions of the Euler equations and take viscous effects into account. The three-dimensional unsteady Navier-Stokes equations describe how the velocity, pressure, temperature, and density of a moving fluid are related. To solve the Navier-Stokes equations, an equation of state that relates the pressure, temperature, and density of the fluid, is required. Additionally, all of the terms of the stress tensor need to be specified. The Navier-Stokes equations are a set of highly nonlinear, coupled differential equations that have not yet been solved analytically. However, if certain simplifying assumptions are made, an approximate analytical solution can be obtained. A numerical solution to the Navier-Stokes equations can be obtained by using computational fluid dynamics (CFD).[13]

2.5 Computational fluid dynamics

In CFD, the flow field is divided into discrete cells. The governing flow equations, e.g., the Euler or Navier-Stokes equations, are discretized by using some discretization method. The stress tensor terms in the Navier-Stokes equations can be approximated by a turbulence model.

In a direct numerical simulation (DNS), the instantaneous Navier-Stokes equations are numerically solved without any turbulence model such that the entire range of spatial and temporal scales of turbulence are resolved. Because of the high number of mesh points and time steps which grows rapidly with the Reynolds number, the computational cost of DNS is very high. For the Reynolds numbers encountered in airplane aerodynamics, the computational requirements of a DNS cannot be met with today's computers. Also Large Eddy Simulation (LES) is a too computationally expensive method for simulation of the flow field around an entire airplane. Therefore, various approximations of the flow field around the airplane are required. Approximations which reduce the time it takes to perform calculations of the flow field are particularly important when developing an airplane. Since the computational cost also limits the number of simulations, an aerodynamic databank model is an important instrument for covering entire flight scenarios.[14]

2.6 Potential flow theory

Potential flow is a model of fluid flow that assumes inviscid and irrotational flow. The full potential equations are obtained by neglecting the vorticity terms in the Euler equations. They are valid for sub-, trans- and supersonic flow at arbitrary angles of attack, as long as the assumption of irrotationality is applicable. In incompressible flow around an airfoil at small angles of attack, the boundary layer and the wake are thin. Hence, potential flow methods are applicable in a large part of the flow, since the flow is approximately inviscid in these regions.

Considering incompressible potential flow over an airfoil or any smooth 2D body, at a given angle of attack, there are an infinite number of valid theoretical solutions, corresponding to an infinite choice of circulation Γ. However, nature adopts a particular circulation for which the flow is smoothly leaving the trailing edge of the airfoil. In addition, if the trailing edge angle is finite, the trailing edge is a stagnation point. If instead the trailing edge is cusped, that is the angle between the surfaces is zero, then, in accordance with Bernoulli's equation, the velocities of the flow leaving the airfoil surfaces at the trailing edge are finite and equal in magnitude and direction. This is referred to as the Kutta condition.[10]

According to the potential flow theory, the flow velocity is equal to the gradient of the velocity potential which is a function of space and time, i.e.,

$$\mathbf{v} = \nabla\phi. \tag{2.4}$$

Since the curl of a gradient is equal to zero, i.e.,

$$\nabla \times \nabla\phi = \mathbf{0}, \tag{2.5}$$

the potential flow must be irrotational. Hence, in flow regions where vorticity is important, such as wakes and boundary layers, the potential flow theory does not give accurate predictions of the flow.[10]

In case of 2D incompressible flow, the velocity has zero divergence, i.e.,

$$\nabla \cdot \mathbf{v} = 0. \tag{2.6}$$

Hence, the velocity potential has to satisfy Laplace's equation,

$$\nabla^2\phi = 0. \tag{2.7}$$

The potential flow in 2D can be analyzed using complex variables. If in addition to 2D and incompressibility, assuming small angles of attack and thin lifting-surfaces, the velocity potential can be split into an freestream velocity and a small perturbation velocity, which gives the so-called small-perturbation potential equation. This is a linear equation that is much easier to solve than the full potential equation.[10]

It is the pressure and shear stress distributions exerted on a surface of a body that gives an aerodynamic force. Circulation is a quantity determined from the surface pressure distribution. In the case of incompressible 2D potential flow, it is in general easier to determine the circulation around the body rather than the surface pressure distribution. Once the circulation is obtained, the lift can be calculated using the Kutta-Joukowski theorem which relates the lift per unit span to the circulation as

$$F_L' = \rho_\infty V_\infty \Gamma. \tag{2.8}$$

The shear stress distribution is not covered by the potential flow theory as it assumes inviscid flow. In nature, any body immersed in a flow will experience drag due to viscous effects that produces a nonzero drag due to skin friction and flow separation.[10]

2.7 The vortex sheet

The concept of vortex sheet plays an important role in the analysis of the flow around airfoils. A vortex sheet is formed by an infinite number of straight vortex filaments of infinitesimally small strength that are placed side by side. A vortex filament is the line along which vorticity with rotation about the line itself occurs. The tangent of the vortex filament is everywhere parallel to the local vorticity vector. According to the Hermann von Helmholtz theorem, the circulation along one vortex filament is constant in time. Furthermore, Helmholtz stated that any vortex filament cannot end in the fluid but must either end at a solid surface or form a closed path.[10]

Considering inviscid, incompressible flow over an airfoil with freestream velocity

V_∞. The airfoil can then be replaced by a vortex sheet of strength $\gamma(s)$, where s is the location on the airfoil contour line. Then, the induced velocity field from the vortex sheet based on $\gamma(s)$ added to V_∞ makes the vortex sheet a streamline of the flow. The circulation around the airfoil is then given by

$$\Gamma = \int \gamma(s)ds, \tag{2.9}$$

where the integral is taken around the entire airfoil surface. Finally, the lift force is obtained by (2.8).[10]

Considering a small section of the vortex sheet of strength $\gamma(s)ds$, an infinitesimally small velocity dV is induced at a point $P(x, z)$ located at a distance r from ds, then the velocity is given by

$$dV = -\frac{\gamma(s)ds}{2\pi r}, \tag{2.10}$$

in accordance with the definition of vortex flow. This equation is particularly useful in analysis of thin airfoils, as in the vortex lattice method. The velocity induced by the entire vortex sheet is obtained by adding the contributions from the different sections of the vortex sheet using vector addition as dV changes direction. In panel methods, it is instead the velocity potential that is calculated, which yields a more straightforward integration. The velocity potential at $P(x, z)$ due to the entire vortex sheet from a to b is obtained as

$$\phi(x, z) = -\frac{1}{2\pi}\int_a^b \theta\gamma(s)ds, \tag{2.11}$$

where θ is the angular location along the surface. The circulation of a section of the vortex sheet of length ds is

$$\Gamma = \gamma(s)ds, \tag{2.12}$$

in accordance with the definition of circulation. Furthermore, the local jump in tangential velocity across the vortex sheet is equal to the local sheet strength.[10]

The philosophy of replacing the airfoil surface with a vortex sheet has physical significance in the sense that it can be seen as a way of modeling the vorticity in the boundary layer of the airfoil in an inviscid flow. According to the thin airfoil theory, a thin airfoil can be approximated with a single vortex sheet as the top and bottom surfaces nearly coincide. The strength of this vortex sheet combined with the freestream velocity and the airfoil camber line forms a streamline of the flow.[10]

2.8 Downwash

The change in direction of the flow that occurs over a lifting wing creates the lift force but also bound vorticity within the airfoil. Since the circulation must be conserved, the circulation of the bound vortex is equal to the circulation of the wing vortex but must spin in the opposite direction. Additionally, vortices are formed near the wing

tips due to the pressure difference between the upper and lower surfaces of the wing. Near the tips of the wing, the air is free to move from the region of high pressure below the wing to the region of low pressure above the wing. This trailing vortex system, consisting of the bound vortex and the tip vortices, gives rise to what is referred to as downwash. The vortex sheet is shed from the trailing edge of a lifting wing as the airplane is moving forward. Due to the direction of circulation, the vortex sheet is deflected downward by a downward pointing force that is proportional in magnitude to the upward pointing lift force acting on the airplane wings. The vortex sheet is convected downstream behind the airplane and eventually dissipated.[15]

Typically, the wing tip vortices do not experience as strong vertical displacement as the vortices in the trailing vortex sheet that are located inboard. Instead, the tip vortices are shed downstream in the horizontal direction behind the airplane. The tip vortices also tend to move inboard as the vortex sheet is convected downstream, while the vorticity in the inboard trailing vortex sheet tends to be transferred to the wing tips. The shape of the trailing vortex sheet has a significant influence on the downwash experienced by the horizontal tail.[15]

Ahead of the wing, the air is in subsonic flight pulled upward due to reduced pressure above the wing. This induced flow is referred to as upwash. The aerodynamic forces acting on the nacelles are influenced by the upwash.[15]

2.9 Numerical methods based on potential flow

Both the vortex lattice method and the panel method are based on the full potential equation, which assume inviscid and irrotational flow. This means that turbulence, dissipation, and boundary layers are not resolved. The vortex lattice method also assumes thin lifting surfaces and a small angle approximation. The panel method covers airfoil thickness effects and varies the orientation of the wake with the angle of attack to more accurately predict the downwash. Despite the fact that it is a highly idealized model, the potential flow theory is, due to the low computational cost and sufficient accuracy, of great importance for aerodynamic and flight dynamic analysis.[16]

2.9.1 The vortex lattice method

The vortex lattice method (VLM) is an extension of the Prandtl lifting line thoery which is a mathematical model that predicts the lift distribution over a wing. As a first attempt to model a finite wing of span b, Prandtl used a bound vortex, extending from $y = -b/2$ to $y = b/2$. Applying Helmholz's theorem, the vortex filament cannot end in the fluid, hence the vortex filaments must continue as two free vortices downstream from the wing tips to infinity. This vortex, consisting of one bound vortex of constant circulation that is shed downstream, and two semi-infinite trailing wingtip vortices, has the shape of a horseshoe, and is therefore called a horseshoe vortex. A single vortex filament does however not realistically describe the flow around the wing as it gives an infinite downwash at the wing tips.[10]

In the lifting line theory, a large number of horseshoe vortices are superimposed along a so-called lifting line along the wing span. The strength of each trailing vortex is equal to the change in circulation along the lifting line. If the number of horseshoe vortices superimposed along the lifting is infinite, a continuous vortex sheet is obtained. The vortex sheet is parallel to the direction of the freestream velocity. The velocity field induced by the horseshoe vortices is calculated based on the Biot-Savart law. According to the Biot-Savart law, in an arbitrary point P with a radius $\mathbf{r}$ from an infinitely small section of a vortex filament $\mathbf{dl}$, the velocity induced at P by the vortex filament is

$$\mathbf{dV} = \frac{\Gamma}{4\pi} \frac{\mathbf{dl} \times \mathbf{r}}{|\mathbf{r}|^3}, \tag{2.13}$$

where Γ is the circulation, that is, the strength of the vortex. The Biot-Savart law is a general result of potential theory describing inviscid, incompressible flows. Using the Biot-Savart law, it can be shown that the magnitude of the velocity for an semi-infinite, straight vortex filament is

$$V = \frac{\Gamma}{4\pi h}, \tag{2.14}$$

where h is the perpendicular distance from P to the vortex filament.[10]

The Prandtl lifting line theory applies the Kutta-Joukowsky theorem, and (2.8) gives the lift produced by a local airfoil section as

$$F'_L = \rho_\infty V_\infty \Gamma(y_0), \tag{2.15}$$

where $\Gamma(y_0)$ is the vortex strength as a function of the spanwise location of the airfoil section. Hence, the unknown is the distribution of the circulation over the wing span, rather than the lift distribution. The circulation around the airfoil is equal to the integral of the strengths of elemental vortices forming the vortex sheet around the complete airfoil surface. Furthermore, the local sheet strength is equal to the local jump in tangential velocity across the vortex sheet. Returning to the Kutta condition, it can be shown that the strength of the vortex sheet is zero at the trailing edge of the airfoil.[10]

Using (2.15), the fundamental equation of Prandtl's lifting-line theory can be derived. It states that the geometric angle of attack is equal to the sum of the effective angle of attack and the induced angle of attack, i.e.,

$$\alpha(y_0) = \frac{\Gamma(y_0)}{\pi V_\infty c(y_0)} + \alpha_{L=0}(y_0) + \frac{1}{4\pi V_\infty} \int_{-b/2}^{b/2} \frac{(d\Gamma/dy)dy}{y_0 - y}, \tag{2.16}$$

where $c(y_0)$ is the chord length at y_0, and b is the wing span. For a finite wing of given design at a given geometric angle of attack and a given freestream velocity, all quantities in (2.16) except Γ are known.[10]

Once (2.16) is solved, the lift distribution can be obtained from (2.15). Furthermore, the total lift force is calculated as

$$F_L = \int_{-b/2}^{b/2} F'_L(y)dy = \rho_\infty V_\infty \int_{-b/2}^{b/2} \Gamma(y)dy. \tag{2.17}$$

The lift coefficient is then obtained as

$$C_L = \frac{F_L}{q_\infty S} = \frac{2}{V_\infty S} \int_{-b/2}^{b/2} \Gamma(y)dy, \tag{2.18}$$

where S is the reference area.[10]

The induced velocity from all trailing vortex filaments is known as downwash. The downwash flow results in a particular rotation of each panel's lift vector relative to the freestream direction. Lift-induced drag is found where the local lift vectors are rotated backwards and is obtained as

$$F'_{D,\,i} = F'_L \sin \alpha_i, \tag{2.19}$$

where α_i is the induced flow angle calculated from the velocities induced on the bound vortex of the panel by other panels and the freestream. The total induced drag is obtained by integrating (2.19) over the span, i.e.,

$$F_{D,\,i} = \int_{-b/2}^{b/2} F'_L(y) \sin \alpha_i(y)dy = \rho_\infty V_\infty \int_{-b/2}^{b/2} \Gamma(y) \sin \alpha_i(y)dy, \tag{2.20}$$

according to [10]. The lift-induced drag coefficient is calculated as

$$C_{D,\,i} = \frac{F_{D,\,i}}{q_\infty S} = \frac{2}{V_\infty S} \int_{-b/2}^{b/2} \Gamma(y) \sin \alpha_i(y)dy. \tag{2.21}$$

The Prandtl lifting line theory assumes that all of the action associated with the bound vortex occurs at the quarter chord point of the wing. As a consequence, the moment coefficients are not calculated. By using VLM, e.g., Athena Vortex Lattice (AVL), the pressure distribution over the wing can be calculated and thus also the moment coefficients. In AVL, the wing is divided into a finite number of panels in both the spanwise and the chordwise directions. In the limit of an infinite number of infinitesimally weak trailing vortices superimposed in the chordwise direction, another continuous vortex sheet is formed. Due to the variation of lift in the spanwise direction, the strength of the trailing vortices is in general different also in the spanwise direction. The two vortex sheets form a lifting surface distributed over the entire planform of the wing. The wake consists of only chordwise vortices as there are no spanwise vortices downstream of the trailing edge. Furthermore, the trailing vortices in the wake do not cross any vortex lines and the strength of the trailing vortices is therefore constant in the longitudinal direction and equal to its value at the trailing edge.[10]

On each panel, the flow is modeled with a horseshoe vortex located at the panel quarter chord at the midpoint in the wingspan direction. The normal velocity induced by all the horseshoe vortices at an arbitrary control point is obtained from the Biot-Savart law. The solution of the equation system from which the vortex strength is solved for must fulfill the flow-tangency condition on the wing surface, i.e., the sum of the induced normal velocity component and the normal component of the freestream velocity must be zero for all control points on the wing. Once the unknown, i.e., the vortex strength Γ_n, is solved for, the lift distribution over the wing can be solved for by using the Kutta-Joukowsky theorem. The total lift force of the wing is the sum of all panel lift components. The lift coefficient of the wing at a given angle of attack is obtained by integration of the panel lift distribution.[10]

The Trefftz plane analysis, derived from the momentum equations, is an alternative approach which provides a more accurate prediction of the induced drag force than the wake integral method [17]. As described in [18], the Trefftz plane gives the induced drag force by integration of the kinetic energy across the wake on the Trefftz plane which is a a vertical plane located at an infinite distance downstream of the airplane. By using Munk's minimum induced drag theorem, the induced drag can be calculated in the Trefftz plane rather than in the real plane. The theorem allows lumping of the chordwise distribution of vorticity into a single chordwise load and translation of the loads into the Trefftz plane. Furthermore, it allows computations to be performed in the Trefftz plane. According to Munk, the downwash produced by the longitudinal vortices must be uniform at all points on the airfoil in order for a minimum drag for a given total lift to exist. If the chordwise distribution of vorticity is lumped into a single chordwise load, the component of the induced velocity perpendicular to the wings must be proportional to the cosine of the local dihedral angle. This boundary condition is used to find the minimum induced drag and hence the optimal aerodynamic efficiency. AVL calculates the alternative induced drag coefficient based on the Trefftz plane, and in [19] it is stated that this drag coefficient is generally more reliable than the drag coefficient calculated by surface force integration.

2.9.2 Panel methods

Panel methods are numerical schemes for calculation of the flow over bodies of arbitrary shape at subsonic or supersonic freestream Mach numbers, assuming linear, inviscid and irrotational flow. In these methods, surface distributions of vorticity singularities are superimposed over panels of the airplane surface. The resulting distribution satisfies the Prandtl-Glauert equation which is the simplest equation governing the motion of fluids that accounts for compressibility effects. It is obtained from the Navier-Stokes equations by neglecting viscous, heat transfer, and nonlinear terms and assuming that the flow is irrotational. In conclusion, the Prandtl-Glauert equation assumes inviscid, irrotational, and linear flow, and neglects separation, skin friction drag, and transonic shock waves. To obtain a unique solution, a Kutta condition must be enforced at sharp trailing edges by adding wake panels downstream from the lifting surface trailing edges. Boundary conditions are imposed at control

points of the panels. In particular, the normal component of the flow velocity is zero at all the control points. Lower order panel methods, e.g. the Hess-Smith code, have singularity distributions with constant strength over each panel, which are usually flat. Higher order codes have e.g. linear or quadratic singularity distribution and may have curved panels.[20]

2.10 Lift distribution

A general lift distribution can be found by using a Fourier series combined with the fundamental equation of Prandtl's lifting-line theory. The final equation for the general lift distribution, which is derived in [10], is

$$C_{D,i} = \frac{C_L^2}{\pi e\, A}, \tag{2.22}$$

where $e \geq 1$ is the span efficiency factor. As stated in [10], the lift-induced drag coefficient can be calculated as

$$C_{D,i} = \frac{C_L^2}{\pi A}, \tag{2.23}$$

where A is the aspect ratio. By comparing (2.23) with (2.22), it can be seen that the lift distribution which gives the minimum induced drag is the elliptical lift distribution.

The thrust required for an airplane to overcome the lift-induced drag is the power required to generate the lift of the airplane. Because the induced drag coefficient is proportional to the square of the lift coefficient, the induced drag coefficient increases rapidly as the lift coefficient increases. At a slow speed, e.g. during takeoff or landing, the induced drag coefficient is a significant part of the total drag coefficient. Also, because the induced drag coefficient is inversely proportional to the aspect ratio, a finite wing with the highest possible aspect ratio is desired in order to reduce the induced drag. The aspect ratio is a compromise between aerodynamic and structural requirements.

Considering a wing with no geometric twist, i.e., a constant geometric angle of attack along the span, and no aerodynamic twist, then it can be shown that the induced angle of attack is constant along the span [10]. As a consequence, also the effective angle of attack, defined as

$$\alpha_{eff} = \alpha - \alpha_i, \tag{2.24}$$

is constant along the span. The induced angle of attack corresponds to the downwash behind the wing. The local section lift coefficient is calculated as

$$c_l = a_0(\alpha_{eff} - \alpha_{l=0}), \tag{2.25}$$

where a_0 is the lift slope and $\alpha_{l=0}$ is the angle of attack at zero lift. Hence, also c_l must be constant along the span. The lift per unit span is obtained as

$$F'_L(y) = q_\infty c c_l. \tag{2.26}$$

Solving for the chord gives

$$c(y) = \frac{F'_L(y)}{q_\infty c_l}, \tag{2.27}$$

where q_∞ and c_l are constant along the span. For an elliptic lift distribution, the chord must vary elliptically along the span, according to (2.27). An elliptic lift distribution causes the downwash across the span to be a constant, resulting in minimum induced drag. Due to manufacturing costs, a compromise between the optimal lift distribution and a simple rectangular wing is commonly selected. A wing with a taper ratio, i.e., a certain ratio between the tip chord and the root chord, such that the lift distribution approximates the elliptic case, is called a tapered wing. The straight tapered wing is one of the most common wing planforms. For standard subsonic airplanes, optimizing the lift distribution is less important than optimizing the aspect ratio, which typically varies from 6 to 22, as the latter has a much stronger effect on the induced drag coefficient.[10]

2.11 Aerodynamic forces and moments

The aerodynamic force on a body immersed in a flow is produced by the net effect of the pressure and shear stress distributions integrated over the body surface. These are the only two sources of aerodynamic forces and moments. The aerodynamic moments are due to aerodynamic forces which do not act through the airplane's CoG.[10]

The resultant aerodynamic force R acting on a body at a given orientation depends on the following parameters.

- freestream velocity (V_∞)
- freestream density (ρ_∞)
- freestream dynamic viscosity (μ_∞)
- reference length of the body, e.g. chord length (c)
- compressibility of the fluid related to the freestream speed of sound (a_∞)

Furthermore, the resultant dimensionless aerodynamic force coefficient corresponding to R is obtained as

$$C_R = \frac{R}{\frac{1}{2}\rho_\infty V_\infty^2 S} = \frac{R}{q_\infty S}. \tag{2.28}$$

As seen in (2.28), the aerodynamic forces and moments acting on the airplane as it moves through the air are directly proportional to the dynamic pressure.

As shown in [10], the resultant aerodynamic force coefficient can be expressed as a function of only the freestream Reynolds number and the freestream Mach number, i.e.,

$$C_R = f(Re,\, M_\infty). \tag{2.29}$$

Since the Reynolds number, as well as the dynamic pressure, depend on the freestream density, the aerodynamic coefficients depend on the altitude, as it determines the

air density. The freestream Mach number is defined as

$$M_\infty = \frac{V_\infty}{a_\infty}, \tag{2.30}$$

and is the ratio of the flow velocity to the speed of sound. The dimensionless parameters Re and M_∞ govern the flow and are the dominating similarity parameters in this study. Additional similarity parameters are needed to cover e.g. the thermodynamics and heat transfer of the flow.[7]

The resultant aerodynamic force can be divided into drag, side, and lift force. The drag force is the component of the resulting force parallel to the freestream velocity, i.e., the relative wind. The side force is defined as the force perpendicular to the freestream in the lateral direction. The lift force is the component of the resulting force perpendicular to the freestream velocity in the vertical direction. The aerodynamic moments acting on the airplane is a measure of the airplane's tendency to turn about its CoG. Rolling, pitching, and yawing are the moments about the longitudinal, lateral, and vertical axis, respectively.[10]

The velocity of the air varies around the surface of the airplane. This velocity variation produces a variation of pressure on the airplane surface. The center of pressure (CoP) is the average location of the pressure acting on the airplane. The total force vector acting at the CoP is equal to the value of the integrated pressure vector field. The aerodynamic moments are zero if the CoP is taken as the reference point. The CoP does not remain in a constant location of the airplane. As the angle of attack changes, the pressure distribution over the airfoil changes, which leads to a change in the location of the CoP. Hence, for convenience, another location referred to as the aerodynamic center (AC) is defined. The AC is the point at which the aerodynamic moment tends to be invariant with respect to the angle of attack. At subsonic speeds, the AC is usually defined as the quarter-chord location from the leading edge, aligned with the chord line.[10]

The AC is of great importance for the stability of the airplane. If the pivot axis is moved forward of the AC, a negative pitching moment will become more negative as the angle of attack is increased. If the pivot axis is placed behind the AC, the pitching moment increases with the angle of attack. A stable equilibrium point is usually associated with a negative slope of the pitching moment curve and an unstable equilibrium with a positive slope. The condition of a steady state moment which tends to restore equilibrium is referred to as positive stiffness.[21]

The aerodynamic coefficients are the nondimensionalized aerodynamic forces and moments and each of them is the ratio of the certain force to the force produced by the dynamic pressure times the area. The airplane drag coefficient is defined as

$$C_D = \frac{F_D}{q_\infty S_W}, \tag{2.31}$$

where F_D is the drag force, and S_W is the wing reference area. The side force coefficient is defined as

$$C_y = \frac{F_Y}{q_\infty S_W}, \tag{2.32}$$

where F_y is the force in the lateral direction. The lift coefficient is defined as

$$C_L = \frac{F_L}{q_\infty S_W}, \tag{2.33}$$

where F_L is the force in the vertical direction. The rolling moment coefficient is defined as

$$C_r = \frac{M_x}{q_\infty S_W b}, \tag{2.34}$$

where M_x is the moment about the longitudinal axis. The pitching moment coefficient is defined as

$$C_m = \frac{M_y}{q_\infty S_W c}, \tag{2.35}$$

where M_y is the moment about the lateral axis, and c is the wing chord length. The yawing moment coefficient is defined as

$$C_n = \frac{M_z}{q_\infty S_W b}, \tag{2.36}$$

where M_z is the moment about the vertical axis.

If not assuming a given orientation, the aerodynamic coefficients are functions of not only the freestream Reynolds number and the freestream Mach number, but also the angle of attack and the side slip angle. Additionally, the aerodynamic coefficients are affected by deflections of the control surfaces and the propulsion system. Other factors that may change the aerodynamic coefficients are e.g., the landing gear, proximity to the ground, and ice accretion.[21]

The angle of attack of the airplane has a great influence on the flow field around the airplane. In symmetric flight, that is, no side slip, the effects of the angle of attack is the same on both sides of the airplane, hence the side force, rolling moment, and yawing moment coefficients are unaffected. The drag, lift, and pitching moment have a strong dependence on the angle of attack in both symmetric and asymmetric flight.[7]

Flying with a side slip angle is aerodynamically inefficient due to the reduced lift-to-drag ratio [7]. The fuselage alters the air flow to surfaces on its downstream side in side slip conditions. Furthermore, the vertical tail is not symmetric about the X_bY_b-plane and will therefore generate additional aerodynamic forces. Side slip can be required to keep the airplane aligned with the runway during a crosswind landing or in the case of flight with asymmetric power, as stated in [22]. Intentional side slip can also be used to increase the descent rate without increasing the airspeed. An airplane possessing static directional stability has a vertical tail which will produce

a restoring yawing moment that will rotate the airplane back to its equilibrium condition, i.e., a zero side slip angle, when being disturbed from its equilibrium such that it is flying with a side slip angle [23]. Hence, an intentional side slip maneuver requires cross-controlling of the ailerons and the rudder [22].

2.11.1 Drag force

The drag force is the component of the resultant aerodynamic force that is parallel to the freestream velocity, and opposes the airplane's motion through the air. This force is composed of pressure drag and skin friction drag, which is consistent with the fact that the only sources of aerodynamic force acting on a body are the pressure and shear stress distributions over the surface of the body. In steady state, except the general dependencies of the aerodynamic coefficients, the drag coefficient strongly depends on the airplane wetted area and the airplane average skin friction coefficient. The drag coefficient of the entire airplane is important for the performance in terms of range and maximum speed.[24]

The pressure drag is due to the pressure distribution over the surface of the airplane. Adverse pressure gradients cause separation of the boundary layer, and formation of a turbulent wake behind the airplane body. The pressure drag is present when there is a difference in pressure across the surface of a body. Hence, it is related to the difference between the high stagnation pressure in front of the body and the low pressure of the wake behind the body. The difference in pressure across a surface implies a difference in force which, by Newton's second law of motion, results in an acceleration if no other force is balancing it. The direction of the force is from the region of high pressure to the region of low pressure. As the angle of attack increases, also the pressure gradient increases. Hence, at high angles of attack, the contribution to the total drag force due to the pressure drag is increased. In absence of flow detachment, the pressure drag is relatively low compared to the skin friction drag. Thus, at subsonic speeds and low angles of attack, the skin friction drag is the dominating drag force component.[10]

The skin friction drag is due to the viscosity of the air, which causes shear stresses within the boundary layer, as explained in [21]. In laminar flow, the skin friction coefficient is inversely proportional to the square root of the Reynolds number, while it in turbulent flows decreases more slowly as the Reynolds number increases. Since the Reynolds number increases with the airspeed and the dynamic pressure increases with the square of the airspeed, the skin friction will be a smaller fraction of the total drag at higher speeds. Several techniques to decrease the skin friction coefficient are presented in [25].

The total drag force is composed by parasitic drag, lift-induced drag, wave drag, and interference drag, i.e.,

$$F_{D,tot} = F_{D,parasitic} + F_{D,induced} + F_{D,wave} + F_{D,interference}. \tag{2.37}$$

The parasitic drag, also referred to as profile drag, is a combination of pressure drag and skin friction drag. The parasitic drag is compromised by the pressure drag of the

wing, and the pressure and skin friction drag of the fuselage, nacelles, empennage, and possibly other components. It also includes the trim drag, that is the pressure and skin friction drag caused by the flight control surfaces when those are used to produce a condition of net zero moments on the airplane, as well as pressure and skin friction drag caused by e.g., flaps, landing gear. In conclusion, the parasitic drag comprises all types of drag except lift-induced drag.[10]

The lift-induced drag is the pressure drag caused by the adverse aerodynamic effects of lift-producing finite wing. The presence of wing tip vortices is the source of the lift-induced drag. The induced drag coefficient is directly proportional to the square of the lift coefficient. Thus, the induced drag is a substantial part of the total drag as the lift increases. Even at relatively high cruising speeds, induced drag stands for about 25% of the total drag. Furthermore, the induced drag is inversely proportional to the aspect ratio which implies that the highest possible aspect ratio is desirable in order to minimize the induced drag. Airplanes can also have winglets to reduce the induced drag by reducing the strength of the tip vortices.[10]

When shock waves are present over the surface of the airplane, an additional pressure drag, referred to as wave drag, is present. Jet engines and cooling inlets give an additional drag component referred to as ram drag which occurs when the airflow continues inside the airplane. The interference drag is defined as the difference between the sum of the drag of the separate airplane components and the total drag of these parts combined. It is caused by the influence of the flow around neighboring components and can be minimized by using fairings and filleting, which induce smooth mixing of the airflow over the components.[9]

2.11.1.1 Drag polar

A measurement of the aerodynamic efficiency is the ratio of the produced lift to drag. The total drag coefficient for the airplane is given by

$$C_D = C_{D,e} + \frac{C_L^2}{\pi e A}, \tag{2.38}$$

where $C_{D,e}$ is the parasitic drag coefficient including the parasitic drag of the wing, and the pressure and friction drag of the other airplane components, and the second term is the lift-induced drag coefficient defined by (2.23). An approximation of $C_{D,e}$ is

$$C_{D,e} = C_{D,0} + rC_L^2, \tag{2.39}$$

where $C_{D,0}$ is the parasitic drag at zero lift, commonly referred to as the zero-lift drag coefficient, and r is a constant. Combining (2.38) and (2.39), and redefining the span efficiency factor to also include the effect of the variation of parasitic drag with lift, gives

$$C_D = C_{D,0} + \frac{C_L^2}{\pi e\, A}, \tag{2.40}$$

where the second term is the drag coefficient due to lift, compromised by both the induced drag and the parasitic drag due to lift, and e is the Oswald efficiency factor.

This parabolic variation of the drag coefficient with the lift coefficient is referred to as the airplane drag polar. It is a fundamental equation in conceptual design and performance analysis of airplanes.[10]

The Oswald efficiency factor is a function of the wing aspect ratio and taper ratio and typically takes a value between 0.7 and 0.85 [10]. In [26], an empirical expression for the Oswald efficiency factor for straight-wing airplanes, based on data obtained from actual airplanes, is given as

$$e = 1.78(1 - 0.045A^{0.68}) - 0.64. \tag{2.41}$$

2.11.2 Lift force

The lift force is the component of the resultant aerodynamic force that is perpendicular to the freestream velocity in the vertical direction. The airplane's total lift coefficient is based on contributions from the wings, fuselage, horizontal tail, and interference effects between these components.

The lift on an airfoil is primarily due to the surface pressure distribution. The shear stress has negligible effect on the lift as it acts mainly in the horizontal direction, that is, the direction of the drag force. Hence, the lift force acting on an airfoil below stall can be approximated by inviscid flow theory. On the contrary, without viscosity there is no lift force. If a boundary layer does not exist, the Kutta condition cannot be fulfilled. In nature, viscosity ensures that the boundary layer remains attached to the airfoil surface until it smoothly leaves the trailing edge.[10]

The derivative of the lift coefficient with respect to the angle of attack is linear up to the stall angle of attack, where the maximum value of the lift coefficient is found. This derivative is of major importance to stability, control, and response to turbulence. At small side slip angles, the dependence of lift on side slip is small. According to [27], maximum lift is affected by the compressibility at Mach numbers of 0.15 and higher. In the lower subsonic region, the maximum lift coefficient is in general decreasing with increasing Mach number.

2.11.3 Side force

If the airplane is symmetric, the side force is mainly due to side slip motion and rudder deflection. The side slip is positive if the relative wind is coming from the right of the nose of the airplane. Hence, a positive side slip angle gives a negative side force. The derivative of the side force coefficient with respect to the side slip angle, i.e., $C_{y,\beta}$ plays an important role in dutch roll dynamics.[24]

The vertical tail size relative to the wing size, as well as the lift curve slope of the vertical tail determines the contribution to C_y due to rudder deflection. A positive rudder deflection produces a positive side force, according to the definitions used in this study.[24]

2.11.4 Rolling moment

The rolling moment is essentially caused by side slip, deflections of the ailerons and rudder, and as damping moments resist rolling and yawing motion. Additionally, except the general dependencies of the aerodynamic coefficients, the rolling moment coefficient depends on the CoG position, as any of the aerodynamic moments. For symmetrical airplane configurations, the rolling moment is approximately zero at zero side slip angle.

The derivative of the rolling moment with respect to the side slip angle, i.e., $C_{r,\beta}$, plays a major role in determining the airplane stability. In the lower subsonic region and at small side slip angles, the rolling moment varies approximately linearly with the side slip angle. However, if the angle of attack changes, the slope of the rolling moment can change significantly. For positive stiffness in roll, $C_{r,\beta}$ must be negative. If a disturbance causes the right wing to roll downwards, the effect of the gravity will yield a positive side slip. Thus, in order to avoid that the roll angle increases further, the rolling moment needs to be negative for a positive side slip. An airplane with high-mounted wings, as the considered airplane, has wings that are located above the airplane's CoG. This gives a dihedral effect, i.e., a rolling moment created from side slip, due to the keel effect. Such designs may have an excessive dihedral effect, making the airplane excessively stable in the spiral mode and difficult to maneuver. Hence, a negative dihedral angle, referred to as an anhedral angle, is usually added to cancel out the excessive dihedral effect.[28]

A wing with sweepback gives a negative rolling moment for a positive side slip angle as the relative wind is closer to being perpendicular to the leading edge of the wing located furthest upwind. For an airplane with high-mounted wings, the angle of attack of the wing located furthest upwind in case of side slip is increased (assuming an initial positive angle of attack) because some of the lateral airflow is redirected up, on top of the fuselage and some is redirected downwards, below the fuselage. Additionally, the lateral component of the relative wind acting on the vertical tail produces a rolling moment about the CoG, which direction depends on the angle of attack and the location of the CoP of the vertical tail. Typically, a positive side slip angle gives a negative rolling moment contribution from the vertical tail.[21]

A rolling moment is produced by deflection of the ailerons. In addition to the aileron deflection angle, this contribution to C_r depends on the aileron chord to wing chord ratio, the wing sweep angle, the Mach number, and the aileron inboard and outboard location. Furthermore, since the CoP of the rudder typically is located above the airplane's CoG, the rudder has a secondary effect of roll.[24]

2.11.5 Pitching moment

For a low-speed propeller airplane, the baseline pitching moment coefficient is essentially a function of the thrust coefficient and the CoG position, except the general dependencies of the aerodynamic coefficients. An increase of the angle of attack gives an increase of the restoring, nose-down moment. At low angles of attack and

high thrust coefficients, the pitching moment curve has a relatively small negative slope because the propeller wash makes the effective angle of attack independent of the freestream direction. The derivative $C_{m,\alpha}$ is of great importance to airplane stability and control.[21] [24]

The pitching moment is controlled by deflection of the elevator. Additionally, a propeller airplane's dynamic pressure at the tail is strongly dependent on the thrust coefficient. To model this effect, the elevator control power can be multiplied with a tail efficiency factor which is a function of the angle of attack, the thrust coefficient, flap deflection, and ground effect. At high values of the thrust coefficient, this factor may exceed two in order to account for a significant increase in the dynamic pressure.[21]

2.11.6 Yawing moment

The yawing moment is caused by side slip, rudder deflection, propeller effects, unbalanced thrust, differences in drag between the ailerons, and asymmetric aerodynamic effects caused by e.g., vortex shedding at high angles of attack.[21] The yawing moment coefficient also depends on the airplane CoG, except the general dependencies of the aerodynamic coefficients. For symmetrical airplanes, C_n is approximately zero at zero side slip angle. The derivative $C_{n,\beta}$ is important in dutch roll and spiral dynamics.[24]

The wing contribution to $C_{n,\beta}$ is usually negligible. The fuselage contribution to $C_{n,\beta}$ depends on the projected side area of the fuselage. The vertical tail contribution to $C_{n,\beta}$ depends on the size of the vertical tail relative to the wing, the lift curve slope of the vertical tail, and the longitudinal distance from the airplane's CoG to the vertical tail's AC.

The yawing moment depend on the side slip via the wing sweep, the fuselage, and the vertical tail. For low side slip angles, this dependence is approximately linear. The wing sweep component is explained by the fact that a positive side slip gives a positive yawing moment as the right wing is closer to being perpendicular to the freestream direction, hence developing more lift and drag. In a positive side slip, a negative yawing moment is produced by the fuselage. In order to achieve directional stability, a yawing moment of the same sign as the side slip angle needs to be provided by the vertical tail. Additionally, the yawing moment is affected by the thrust coefficient.[21]

Deflection of the rudder causes a strong yawing moment which is used to create or counteract the sideslip. The rudder contribution to C_n depends on the size of the rudder relative to the vertical tail size, the vertical tail size relative to the wing, the lift curve slope of the vertical tail, and the longitudinal distance between the airplane's CoG and the AC of the vertical tail [15]. Wing downwash and blanketing can affect the vertical tail and the rudder at high angles of attack, as stated in [21]. The downwash affecting these components can also change due to deflection of the

wing flaps. Furthermore, because of the difference in drag between the ailerons on each side, a yawing moment is produced if the ailerons are deflected.

2.12 Local angles

As explained in Section 2.8, the downwash changes the effective angle of attack. This angle is called the induced angle of attack, and is defined as the angle between the local relative wind and the freestream velocity vector [29]. It is the change in direction of the streamlines caused by a lift-producing wing. The resulting angle of attack considering the upwash effect is determined by adding an upwash, corresponding to the slope of the streamlines ahead of the wing, to the freestream angle of attack [26]. The upwash pushes upwards against the bottom of the fuselage and turns the flow prior to reaching the propellers which are located ahead of the wing.

Wingtip vortices also induce sidewash which affects the static yaw stability of the airplane. The vertical tail is mounted above the wing and will therefore have a negative sidewash gradient. Hence, it increases the stabilizing effect of the vertical tail.

The horizontal tail provides stability about the lateral axis. In order to achieve equilibrium, the lift of the tail is generally in the downward direction. The flow field downstream of the wing changes the aerodynamic coefficients of the airplane's horizontal tail and has to be accounted for in the stability and control analysis of the airplane. The downwash behind the wing affects the angle at which the flow approaches the tail. At high angles of attack, the wake behind the wings decreases the local dynamic pressure at the horizontal tail which may cause the flow to separate. This leads to a reduced horizontal tail contribution to the pitching moment.

The rate of change of angle of attack arises primarily from the time lag associated with the downwash of air behind the wing affecting the horizontal tail. Since the vorticity are convected with the local fluid velocity behind the wing, there is a time lag for the vorticity to convect from the wing to the tail. The instantaneous angle of attack seen by the horizontal tail is thus different from the angle of attack seen by the wing. In a similar way, the rate of side slip angle due to the sidewash causes the instantaneous side slip angle seen by the vertical tail to deviate from the instantaneous side slip angle seen by the wing.

If the aircraft is rolling, the wing tip that moves downwards produces more lift than the wing tip that moves upwards. These forces opposes the rolling motion. The rolling motion of the airplane causes adverse yaw, which generates side slip. Hence, the roll rate will also change the local side slip angle at the vertical tail as well as the local aerodynamic angles at the nacelles. The pitch rate yields a translational rate of the horizontal tail perpendicular to the freestream velocity. This changes the angle of attack of the horizontal tail, and hence its lift and pitching moment coefficients. For small induced translational rates compared to the true airspeed, the change in the horizontal tail angle of attack varies approximately linearly

with the pitch rate. Also the local angle of attack at the nacelles will change due to the pitching motion. When an airplane is yawing, the airflow reaches the airplane at an angle relative to the X_b-axis. The yawing motion changes the local side slip angle at the vertical tail and nacelles due to the change in the airflow behind the wing.[21]

Wind disturbances gives additional aerodynamic loads on the airplane and need to be accounted for in the aerodynamic databank model. The aerodynamic angles will change if the airplane is subject to a wind gust, which in turn changes the aerodynamic coefficients.

2.13 High-lift devices

During cruise flight, the wing should have low camber and should operate at high wing loading in order to maximize the aerodynamic efficiency. For takeoff and landing, to allow for flight at a lower speed, a large lifting force is desired at the same time as the drag is not objectionable. This is associated with a high camber and low wing-loading. The trailing-edge flap is the most common type of high-lift device and increases the lift at a given angle of attack by increasing the camber of the wing. The stall angle of attack is only slightly affected by the flaps.[26]

The flaps affect both the parasitic drag and the lift-induced drag. The contribution to the parasitic drag due to deflection of the flaps is caused by the flow separation above the flap. The induced drag is minimized when the wing has an elliptical lift distribution, as mentioned in Section 2.10. Deflecting the flaps means that the lift distribution is further away from being elliptical and hence the lift-induced drag is increased.[26]

2.14 Control surfaces

Aircraft flight control surfaces are used to control the roll, pitch, and yaw. The primary control surfaces for roll are the ailerons, and the secondary control surface is the rudder. The primary control surface for pitch is the elevator. The primary control surface for yaw is the rudder, and the secondary effect is due to deflection of the ailerons.[26]

2.14.1 Ailerons

The ailerons are located on the outboard trailing edge of each wing and are interconnected such that they move in the opposite direction to each other. A downward deflection of the aileron gives increased lift of the wing and vice versa. This action produces a rolling moment acting on the airplane and is used to change its heading. This maneuver is called a banking turn. An undesirable side effect of the aileron deflection is the adverse yaw, that is, a yawing moment in the opposite direction to the roll. In a coordinated turn, a rudder deflection is applied to counteract the

adverse yaw. A downward deflection of the aileron surface is in this study defined as a positive deflection angle.[26][21]

2.14.2 Rudder

The rudder is a primary flight control surface mounted on the trailing edge of the vertical tail. It is used to generate and control the yawing moment of the airplane. A deflection of the rudder gives a horizontal force acting on the vertical tail in the opposite direction due to the alteration of the airflow around the rudder. This force gives a yawing moment about the airplane's CoG. The rudder is used to coordinate a banking turn of the airplane by counteracting the adverse yaw induced by the aileron deflections. Deflecting the rudder to the left is in this study equivalent to a positive deflection angle.[26][21]

2.14.3 Elevator

The elevator is mounted on the trailing edge of the horizontal tail. It is used to control the pitching moment about the airplane's CoG and hence the angle of attack. An upward deflection of the elevator is in this study defined as a negative deflection angle. This action increases the drag and decreases the lift of the horizontal tail. The resulting force that is acting downward on the horizontal tail gives a positive pitching moment which increases the angle of attack of the airplane's wings. If instead the elevator is deflected downwards, in this study corresponding to a positive deflection angle, a negative pitching moment is produced and the angle of attack will be reduced.[26][21]

2.15 Mach effect

In Section 2.11, it was stated that the aerodynamic coefficients can be expressed as functions of Re and M_∞. The dependence on M_∞ is primarily due to compressibility. For instance, other effects occur in the transonic region but are however not relevant in this study [7]. In subsonic flow, i.e., $M_\infty < 1$, the streamlines are smooth and disturbances in the flow propagate in all directions, as stated in [10]. The condition $M_\infty < 1$ does however not guarantee that the entire flow field is subsonic.

At Mach numbers less than about 0.3, the flow can be assumed to be incompressible [10]. The considered airplane is assumed to have a top speed of about 215 kts, which means that the Mach number can exceed 0.3. Hence, the dependence of the aerodynamic coefficients on the Mach number needs to be considered in the aerodynamic databank model.

2.16 Propeller effect

The most direct effect of the propellers are the thrust forces they produce which moves the airplane forward through the air. On the considered airplane, the pro-

pellers are located above the airplane CoG, resulting in a nose down pitching moment. This pitching moment is additive to the aerodynamic moment and the total pitching moment is trimmed to zero by adjusting the elevator. A high power coefficient gives an increase of the maximum lift coefficient and a shift of the peak to a higher angle of attack.[21]

Indirect effects of the propellers are due to the induced flow associated with a propeller and the slipstream behind it. The propeller slipstream causes the skin friction to increase due to a higher local dynamic pressure on the surfaces within the slipstream region. The propeller turns the flow such that a normal force is produced, causing a nose up pitching moment. This normal force depends on the angle of attack and the increase of the kinetic energy by the propeller blades. The wake behind the propeller changes the flow over the wing and empennage. The effectiveness of the horizontal tail is increased because of the increased flow velocity and the reduction in downwash angle. The effects due to the induced flow associated with propeller-driven airplanes can have significant influence on the longitudinal static stability.[30]

2.17 Ground effect

The ground effect is of importance at a height above ground of approximately one wing span and increases in magnitude as the height above ground decreases. In proximity to the ground, the induced downwash is restricted by the ground, reducing the lift-induced drag. The air pressure on the lower wing surface is increased near the ground, which improves the lift-to-drag ratio of the airplane. The wings require a lower angle of attack to produce the same amount of lift in proximity to the ground. Furthermore, the reduction in downwash affects the pitching moment and a a greater deflection of the elevator to hold the nose up is required.[1]

2.18 Aerodynamic derivatives

The aerodynamic forces and moments are in general not linear functions of their states, hence the dynamic derivatives changes as flight conditions change. A dynamic derivatives measures the change in a force or moment acting on the airplane due to a change in a flight condition parameter. The dynamic derivatives that are due to a change in a parameter related to the airplane's stability are called stability derivatives. The relevant parameters are the rate of angle of attack, rate of side slip angle, roll rate, pitch rate, and yaw rate.

The aerodynamic derivatives provide information about the stability and maneuverability of the airplane, and the effectiveness of the control surfaces [21]. As they correlate with the geometrical properties of the airplane, they are important in the preliminary design process. Methods for estimating the stability derivatives are found in e.g., the United States Air Force (USAF) Stability and Control DATCOM [1], ESDU [2], and Airplane Design Part VI [24]. Later in the development of the

airplane, the stability derivatives are obtained from a flight test.

The most important derivatives of the aerodynamic forces and moments due to a constant roll, pitch, or yaw rate are seen in Table 2.2. The other derivatives are in general small and have negligible effect on the airplane dynamics.[21]

Table 2.2: The aerodynamic derivatives with respect to roll, pitch, and yaw rate

Roll derivatives	Pitch derivatives	Yaw derivatives
$C_{y,p}$	$C_{D,q}$	$C_{y,r}$
$C_{r,p}$	$C_{L,q}$	$C_{r,r}$
$C_{n,p}$	$C_{m,q}$	$C_{n,r}$

The aerodynamic derivatives also includes the acceleration derivatives. The main reason for accounting for changes of the aerodynamic angles is that, as the flow around the airplane changes, there is a small delay in the downwash and sidewash effects experienced by the airplane's tail. As a first-order approximation of these effects, the resulting forces and moments can be modeled as being directly proportional to the aerodynamic angular rates. The acceleration derivatives that are most commonly included are $C_{L,\dot{\alpha}}$ and $C_{m,\dot{\alpha}}$. The other acceleration derivatives are in general small and have negligible effect on the airplane dynamics.[21]

2.19 Aircraft stability and control

In steady-state flight, the angular rates must be zero or constant, implying that the aerodynamic moments acting on the airplane are constant. Furthermore, the airspeed, angle of attack, and side slip angle must be constant in steady-state flight, implying that the aerodynamic forces are constant. The tendency of the airplane to return to its equilibrium, following an external disturbance, is related to its stability. The instantaneous response of a perturbed system, in this case the airplane, is referred to as the static stability. Analysis of the static stability neglects rate-dependent effects. The dynamic stability describes how the airplane responds over time. A dynamically stable airplane will return to its equilibrium but not necessarily immediately. An aircraft may be statically stable, but dynamically unstable. Static instability, however, implies dynamic instability.[21]

If the pilot wants to change the state of the airplane, control is required. Stability and control of the airplane is essentially setting and maintaining an equilibrium, i.e., to trim the airplane. A body is in equilibrium when the net force and net moment acting on it are both zero. Up to the stall angle of attack, the lift curve slope is linear. Within this region, the pilot expects linear response to the control inputs.[31]

Airplane trimming is equivalent to searching for global optima in the airplane dynamics. The optimization method should find the steady state for a set of input data and the control surface positions to keep the aircraft stable in a certain maneuver. The set of flight conditions, including e.g., the altitude, the airspeed, and the angle

of attack, is called a trim condition if these variables are in steady state. When the flight conditions are steady, the dynamic derivatives are constant. A stability analysis including maneuvers that span a great range of flight conditions requires the dynamic derivatives to change.[21]

For an aircraft certified under EASA CS-23 [32], static longitudinal, lateral, and directional stability in normal operations is a requirement. Regarding the longitudinal stability, the airplane must not exhibit any divergent longitudinal stability characteristic so unstable as to increase the pilot's workload or in other ways cause any danger. Hence, a requirement for an equilibrium to be stable is that when the airplane is pitched nose-up by a perturbation, the change in moment must be such as to pitch it nose-down, and vice versa [31].

The AC of the entire aircraft is referred to as the neutral point. By analyzing the total lift on the airplane acting at the neutral point, a relationship between the CoG position and the static stability can be obtained. The sign of the pitching moment depends on the relative positions of the neutral point and the CoG. If the CoG is located forward of the neutral point, the airplane is longitudinally static stable. In this case, an increase of angle of attack creates a negative (nose-down) pitching moment on the airplane such that the angle of attack decreases, and vice versa. If the CoG is too far forward, it may cause difficulty for the pilot to bring nose-up as for landing. If instead the CoG is located aft of the neutral point, the airplane is longitudinally static unstable.[31]

The airplane has six degrees of freedom. The difficulty in the analysis of the dynamic behavior of the airplane is that its motion is coupled between the different degrees of freedom. To decouple the longitudinal and lateral-directional motions, linearity is assumed, i.e., the perturbations are of first order. The nonlinear states equations are expanded in a Taylor series about the equilibrium point, keeping only the first-order terms, referred to as the aerodynamic derivatives, as described in [21]. If these constants are known, as well as the state of the airplane, its motion can be determined by Newton's laws of motion. The assumptions made when linearizing the state equations are as follow.

- The forces and moments depend on the velocities but not on the accelerations, except the pitching moment, which depends on the acceleration in the vertical direction.
- Lateral symmetry, i.e., that a pitch disturbance cannot cause roll or yaw.
- The symmetric response to an asymmetric input is symmetric.
- There is no inertial coupling between roll and yaw.

The linearization yields two sets of equations, one for the longitudinal motion, e.g., phugoid oscillation, and one for the lateral-directional motion, e.g., the Dutch roll mode and the spiral mode. These equation systems are now uncoupled and the longitudinal and lateral-directional dynamics can be treated separately as two systems with three degrees of freedom each.[31][21]

The solutions to the equations of motion for the airplane, that is the eigenvalues, are the dynamic modes. The dynamic modes are the time-dependent behavior of the system in response to an impulsive input. The dynamic stability is of critical importance as the pilot's ability to control the airplane is linked to the dynamic modes.[21]

The responsiveness of the airplane to maneuvering commands is connected to the the natural frequencies of the short-period, roll subsidence, and Dutch roll modes. These modes are determined by the moments of inertia of the airplane and the aerodynamic moments acting on the airplane. The damping of these modes is determined by the rate-dependent aerodynamic moments. Usually, a stability augmentation system is used to give these modes desirable damping and frequencies. The phugoid and spiral modes have lower frequencies and are controllable by a pilot. However, an autopilot, i.e., an automatic control system, is used to reduce the workload of the pilot and reduce operation errors.[21]

2.19.1 Longitudinal stability

As the pilot most of the time wants to maintain steady level flight, the longitudinal stability of the airplane is important in determining whether the pilot will be able to control the aircraft without it requiring excessive workload.

The longitudinal control involves the ability to maintain or change the airplane's angle of attack. The angle of attack controls the lift of the airplane. Steady level flight, change of incidence, change of height, and recovery from stall are all cases when the pilot controls the airplane's motion about the pitching axis. Flying the airplane at steady level flight requires static longitudinal stability.

The longitudinal stability derivatives of importance are in Table 2.3 presented in order of importance according to [21].

Table 2.3: The longitudinal stability derivatives in order of importance [21]

Derivative	Description
$C_{L,\alpha}$	lift curve slope
$C_{m,\alpha}$	pitch stiffness
$C_{m,q}$	pitch damping
$C_{m,V}$	Mach tuck derivative
$C_{m,\dot{\alpha}}$	derivative of pitching moment with respect to the rate of angle of attack
$C_{D,V}$	speed damping
$C_{D,\alpha}$	drag versus angle of attack slope
$C_{L,V}$	lift versus speed slope
$C_{L,\dot{\alpha}}$	lift acceleration derivative
$C_{L,q}$	lift versus pitch slope

The Mach tuck derivative as well as the other speed derivatives are negligible at low subsonic speeds. Furthermore, the derivatives with respect to the rate of angle of

attack are usually small and negligible.[21]

2.19.1.1 Lift curve slope

The lift curve slope $C_{L,\alpha}$ affects the maneuverability, damping of the pitching motion, and comfort of the airplane. Low-speed airplanes, as the airplane considered in this study, usually have wings with high aspect ratio and low sweep angle, which gives a large value of $C_{L,\alpha}$. In the linear region of the lift curve, its slope is approximately independent of the angle of attack. When a large amount of lift is produced by the wings, the twist reduces the local angle of attack near the wingtips which gives a reduction of the lift curve slope as the angle of attack increases.[21]

For static stability against perturbations in vertical velocity, the lift curve slope of the airplane must be positive. As long as the angle of attack is below the stall angle of attack, this criterion is fulfilled. The lift curve slope plays an important role in the response to turbulence. In the case of turbulence, the angle of attack is continuously changing. The derivative of the load factor n, defined as

$$\frac{\partial n}{\partial \alpha} = \frac{\partial F_L}{\partial W} \approx \frac{\partial (C_{L,0} + C_{L,\alpha}\alpha) q_\infty S}{\partial W} = \frac{q_\infty C_{L,\alpha}}{W/S}, \tag{2.42}$$

is referred to as the load factor due to gust induced angle of attack. If the value of $\frac{\partial n}{\partial \alpha}$ is large, the flight through turbulence will be more rough, while it will be more smooth if the value of $\frac{\partial n}{\partial \alpha}$ is small.[15]

2.19.1.2 Pitch stiffness derivative

The derivative $C_{m,\alpha}$ is called the pitch stiffness derivative or the static longitudinal stability derivative. A stable equilibrium and positive stiffness are associated with a negative $C_{m,\alpha}$. This criterion is fulfilled as long as the AC is located aft of the CoG. The distance between the AC and the CoG varies with the Mach number and the lift curve slope of the wing. The second most important parameter affecting $C_{m,\alpha}$ is the lift curve slope of the horizontal tail.[21]

The pitch stiffness derivative is important for the airplane's pitch stability and the dynamic behavior due to pitching motion. The purpose of the horizontal tail is to create a stabilizing pitching moment such that it allows the CoG to be located further aft. Furthermore, as the AC moves aft with increasing Mach number, depending on the CoG position, the pitch stiffness will increase.[21]

2.19.1.3 Pitch damping derivative

The derivative $C_{m,q}$ is the slope of the curve of the pitching moment and determines the moment that opposes any pitch rate. It is therefore called the pitch damping derivative and is important for the airplane's pitch stability and its dynamic pitch behavior. It is negative as long as the flow is attached, which means that the pitch rate stability is fulfilled. Aeroelasticity and the Mach number both affects this derivative.[15]

The main contribution to $C_{m,q}$ is from the horizontal tail but also the wing gives a small contribution to $C_{m,q}$ [33]. As described in [21], a pitching motion changes the angle of attack and lift of the tail, and hence its moment about the airplane's CoG. At small pitch rates, the tail pitch damping moment varies linearly with the pitch rate. When the wing is pitching about the CoG, local changes of the angle of attack occur, causing the angle of attack for the entire wing to increase. This leads to an increase of the pitching-moment and is equivalent to the wing pitching derivative $C_{m,q}$.

2.19.1.4 Drag versus angle of attack slope

The drag curve is related to the two regions of command referred to as the region of normal command, and the region of reversed command. In the region of normal command, power must be added to increase the speed of the airplane. This region is defined as the region where the speed is higher than the speed corresponding to the minimum drag. Flight in the region of normal command gives a relatively strong tendency of the airplane to maintain the trim speed.[34]

If the airplane is flying in steady level flight, the lift force equals the gravitational force, and the available power equals the required power. If increasing the airspeed while keeping the same power setting, there is a lack of power. The natural tendency of the airplane will cause the airplane to return to the initial speed to balance power and drag. If reducing the airspeed while keeping the same power setting, an excess of power exists. The airplane's natural tendency will speed up the airplane to regain the balance between power and drag. In conclusion, the static longitudinal stability of the airplane tends to return the aircraft to the original trimmed condition if the flying is conducted in the region of normal command.[34]

2.19.1.5 Lift coefficient versus pitch

The wing pitching derivative $C_{L,q}$ is the lift due to pitching velocity at a constant angle of attack. This derivative is in general small compared to the other terms in the equations of motion and is thus frequently neglected.

2.19.2 Lateral-directional stability

The lateral-directional stability derivatives are presented in Table 2.4 in order of importance according to [21].

The derivatives with respect to the side slip angular rate are usually neglected because, as stated in [21], they are usually of little importance and are difficult to measure.

Table 2.4: The lateral-directional stability derivatives in order of importance [21]

Derivative	Description
$C_{r,\beta}$	dihedral derivative
$C_{n,\beta}$	yaw stiffness
$C_{r,p}$	roll damping
$C_{n,r}$	yaw damping
$C_{n,p}$	yawing moment due to roll rate
$C_{r,r}$	rolling moment due to yaw rate
$C_{y,\beta}$	side force due to side slip
$C_{y,r}$	side force due to yaw rate
$C_{y,p}$	side force due to roll rate
$C_{n,\dot{\beta}}$	yawing moment due to side slip rate
$C_{y,\dot{\beta}}$	side force due to side slip rate
$C_{r,\dot{\beta}}$	rolling moment due to side slip rate

2.19.2.1 Dihedral derivative

The dihedral derivative $C_{r,\beta}$ is the derivative of the rolling moment with respect to the side slip curve. To obtain positive stiffness in roll, $C_{r,\beta}$ should be negative. This can be provided by having a positive wing dihedral. On the contrary, too much roll stiffness reduces the damping of the airplane's dynamic behavior in the dutch roll mode.[15]

2.19.2.2 Yaw stiffness derivative

The yaw stiffness derivative $C_{n,\beta}$, commonly referred to as weathercock stability, is the tendency of the airplane to point towards the relative wind, as described in [21]. For directional stability, it is desirable that the airplane should tend to return to an equilibrium after being subjected to a yawing disturbance. The yaw stiffness derivative $C_{n,\beta}$ is the slope of the curve of the yawing moment due to sideslip. For positive yaw stiffness, this derivative must be positive. The vertical tail is the primary surface that determines the yaw stiffness derivative. The yaw stiffness is also important in the Dutch roll mode. However, if $C_{n,\beta}$ is too large, the aircraft may be spirally unstable [31].

2.19.2.3 Roll damping derivative

The main contribution to $C_{r,p}$ is from the wing and is a function of the wing-tip helix angle [1]. When the airplane is rolling, there is a variation in angle of attack along the wing span, as explained in [21]. In the linear region of the lift curve, the difference in lift between the wings is linearly proportional to the roll rate. The roll damping derivative is normally positive and provides a damping rolling moment. For that reason, it is important for the handling qualities of the airplane, and more specifically in the response to aileron deflection. For airplanes with high aspect ratio wings and modest sweep, the $C_{r,p}$ derivative is large compared to the other rolling derivatives [35].

2.19.2.4 Yaw damping derivative

The yaw damping derivative $C_{n,r}$ is mainly determined by the vertical tail. As long as the flow over the airplane is essentially attached, $C_{n,r}$ is negative and linearly proportional to the yaw rate. The total $C_{n,r}$ derivative is important in lateral dynamics, Dutch roll damping, and spiral mode damping. The main contribution to the Dutch roll damping is provided by this derivative. In general, a large negative value of $C_{n,p}$ is desired.[21]

2.19.2.5 Yawing moment due to roll rate

The wing rolling derivative $C_{n,p}$ is, as $C_{r,p}$, a function of the wing tip helix angle, as stated in [1]. It is due to an unsymmetrical lift distribution that causes a difference in drag between the wing panels when the wing is rolling. For an airplane with positive weathercock stability, $C_{n,p}$ tends to turn the airplane in the direction towards which is sideslipping, as mentioned in [35]. The $C_{n,p}$ derivative and the $C_{n,\beta}$ derivative opposes each other, and the direction of yawing depends on which of these derivatives that has the strongest effect. The total $C_{n,p}$ derivative affects the Dutch roll damping and a positive value of $C_{n,p}$ increases the Dutch roll damping characteristics [21].

2.19.2.6 Rolling moment due to yaw rate

If the airplane has positive weathercock stability, the side slip velocity creates a yawing moment which turns the airplane in the direction in which it is sideslipping. Since a yawing moment causes an increase of the velocity over one wing relative to the other, there is a rolling moment associated with yawing. If there is no opposing moment, the airplane will take a tighter turn, referred to as spiral instability. The rolling moment due to side slip, $C_{r,\beta}$, is the restoring moment which must overbalance the rolling moment due to yaw rate, $C_{r,r}$. The sign of the $C_{r,r}$ derivative is the same as that of the yaw rate.[35]

2.19.2.7 Side force due to sideslip

The wing contribution to $C_{y,\beta}$ depends primarily on the geometric dihedral angle of the wing. For small geometric dihedral angles, the wing contribution is generally small and can be neglected. The contribution to $C_{y,\beta}$ from the fuselage depends strongly on its shape and size relative to the wings and the location where the wings are attached to the fuselage. In general, the fuselage contribution to C_y is small. The vertical tail's contribution to $C_{y,\beta}$ depends on its size relative to the wings as well as its lift curve slope.[15]

2.19.2.8 Side force due to yaw rate

The vertical tail is the dominating contribution to the derivative $C_{y,r}$, according to [33]. The wing contribution to $C_{y,r}$ is generally small relative to the vertical tail contribution and is thus commonly neglected. Since the effect of $C_{y,r}$ on the stability and control characteristics of the airplane is small, $C_{y,r}$ is in many cases neglected completely [36].

2.19.2.9 Side force due to roll rate

The $C_{y,p}$ derivative is relatively unimportant in the airplane dynamics analysis. However, $C_{y,p}$ plays an important role in correcting the other rolling derivatives when the CoG location is changing. In particular, its contribution to $C_{n,p}$ can be significant. The main contributions to the roll rate derivative $C_{y,p}$ are the wing and the vertical tail.[33]

The wing rolling derivative $C_{y,p}$ is the change of the side force coefficient due to change in wing tip helix angle. It is a result of the angle of attack distribution and tip suction effects of rolling wings. This contribution to $C_{y,p}$ is, however, small compared to the contribution from the vertical tail. The vertical tail gives in general a negative contribution to $C_{y,p}$, but at high angles of attack the sign of the moment arm may change.[15]

2.20 Ice effect

In certain atmospheric conditions, ice formation on the airplane can occur. The accretion of ice affects the aerodynamic forces and moments by increasing the vertical load and changing the shape of the airfoils, as described in [37]. As a consequence, the drag is increased and the maximum lift and stall angle of attack are decreased. Additionally, icing may also affect the control surface effectiveness, hinge moments, and damping. For safety reasons, the airplane is thus equipped with an ice protection system. However, it is important to study how different types of icing affects the airplane's performance, stability, and control in order to prevent accidents. Furthermore, certification for flight in icing conditions requires definitions of the operation limitations and instructions on how to operate the airplane safely in such conditions [32].

Temperatures below 0 °C combined with high liquid water content (LWC) are the most important factors for aircraft icing, as stated in [38]. The LWC depends on the type of clouds in the atmosphere at a given spatial and temporal moment. Additionally, the droplet size distribution in clouds has a large impact on the possible ice accretion rate. The droplet size distribution in the cloud is typically represented by the median volume diameter (MVD) [39]. The MVD is the midpoint droplet size, i.e., the total water volume present in the assumed droplet distribution is divided by two such that half of the water volume is contained in droplets larger than the MVD value, and half in smaller. In [40], it is empirically and mathematically shown that the median volume diameter as a single droplet size approximation gives a more accurate estimation of the collision efficiency compared to the mean volume diameter and the mean diameter.

Supercooled large droplets (SLDs), with a size larger than 40 μm, can be particularly dangerous. SLDs have larger inertia, causing them to not follow the airflow around the airplane, which gives a higher collection efficiency compared to small

droplets. Furthermore, when large droplets impinge on the airplane surface they may not freeze immediately but flow along the surface, which gives a larger spread of the ice and a denser and harder ice. During takeoff and landing, freezing rain and drizzle containing SLDs near the ground can be particularly dangerous.[41]

To determine the risk of icing, the meteorological factors and airplane parameters needs to be defined. Based on these data, the ice shape and the change of the aerodynamic coefficients can be determined.

2.20.1 Ice accretion types

The main types of ice accretion are glaze ice, rime ice, and mixed ice. Typically, the rime icing occurs at temperatures about -15 °C and below, glaze ice occurs at temperatures near 0 °C, and mixed ice occurs at temperatures between these two [42].

The rime ice forms when flying through stratiform clouds and a low rate of small supercooled water droplets impinge on the airplane. The airplane skin temperature must be at a temperature below 0 °C, making the droplets freeze rapidly, hence their spherical shape is retained. This process gives a relatively brittle mixture of ice and air with an irregular shape.[38]

The glaze ice poses a risk in areas a with high concentration of SLDs, such as cumuliform clouds and freezing rain. Because the SLDs do not freeze instantly as they impinge on the airplane surface but freeze gradually as they move across the surface, a smooth, hard, and clear ice is formed over the surface. At temperatures just below freezing, horn ice accretion may occur. Gradually freezing droplets coalesce into a horn on only the upper airfoil surface or both the upper and lower airfoil surfaces, depending on the icing and flight conditions. The horn has a rough and irregular surface. The large discontinuity of the horn ice creates a local boundary layer separation behind it. Unless the angle of attack is large or the horn ice is significant, the separated air will reattach to the wing surface at a certain point after the ice formation. Due to its irregular shape, hardness, spread and density, the clear ice is the most hazardous type of icing. A mix of clear and rime icing can occur in situations when large and small supercooled droplets coexist, giving a combination of rime and clear ice characteristics.[38]

The potential ice shape in a certain atmospheric condition depends on the airfoil geometry as well as on the flight duration time, airspeed, angle of attack, altitude, etc. The efficiency of the ice protection system needs to be evaluated for various atmospheric conditions and flight configurations in order to define its limitations.

2.20.2 Atmospheric conditions

In general, supercooled droplets can occur in any cloud with a temperature below 0 °C and with a lack of ice nuclei [38]. When these droplets impinge on the exposed

airplane surfaces, they freeze to form ice unless the ice protection system is activated. In the U.S., icing is most frequently encountered around 10,000 ft above sea level, with few encounters above 20,000 ft [38]. Considering domestic flights in the U.S., the most severe icing is encountered in the winter at altitudes of 7000 to 9000 ft above ground level, according to flight data [39]. Important factors influencing the formation of supercooled droplets are temperature, LWC, ice nuclei concentration, orographic lift, lake-effect snow, and turbulence [43]. Furthermore, clouds in continental regions generally contain smaller droplets than clouds in maritime regions [38].

Stratiform and cumuliform is the general classification of clouds relevant for in-flight icing. The stratiform clouds are layer clouds that are not vertically developed. Regions ahead of warm fronts, associated with widespread lifting of air with high LWC, may provide icing if the temperature is below about 0 °C. The greatest icing risk in stratiform clouds is typically below 6500 ft since the LWC and horizontal extent are greater. Above 6500 ft, the stratiform clouds can extend over thousands of square miles but are typically thin. Flight in stratiform clouds can thus result in icing conditions of long duration. In stratiform clouds, rime ice is the most frequently observed type of ice. The LWC in stratiform clouds is in general moderate with a maximum value of 1.1 g/m^3.[39]

Cumuliform clouds are developed by atmospheric instabilities that causes vertical motions. These clouds can form wherever the air near the ground is colder than the ground or water surface. Ahead of cold fronts, the region of lifting air is generally more concentrated and intense, resulting in deep cumuliform clouds such as cumulonimbus (thunderstorms). Besides icing, strong convective updrafts can be hazardous due to turbulence, electrical disturbance, and hail precipitation. Cumuliform clouds have on average higher altitude coverage than stratiform clouds and can give icing conditions at altitudes up to 20,000 ft. The rapid development and a large LWC, which due to the adiabatic lifting process may be in a supercooled state, makes the cumuliform clouds an important icing hazard. Typically, the cumuliform clouds covers less horizontal area and give a shorter duration of exposure to icing than the stratiform clouds. Furthermore, the LWC is typically high and can reach up to 8 g/m^3 for large tropical cumulonimbus clouds. The icing in cumuliform clouds is usually clear or a mixture of clear and rime ice.[38] [39]

2.20.3 Certification of flight in icing conditions

The icing conditions are determined by the envelopes in Appendix C of Part 25 of Title 14 in the United States Code of Federal Regulations [44]. It is a widely used standard for airplane ice protection systems and defines the atmospheric icing conditions for certification of flight in icing conditions. EASA adopts FAA AC 23.1419-2 as acceptable means of compliance with the ice protection regulation CS 23.1419 [45].

The variables used for defining the icing envelopes specified in [44] are the the LWC, mean effective diameter of the droplets, the ambient air temperature, and the

relationship of these variables. In [44, Fig. 1], the continuous maximum atmospheric icing conditions for stratiform clouds and a cloud horizontal extent of 17.4 nautical miles is defined by the LWC as a function of the mean effective droplet diameter. It covers pressure altitudes from sea level to 22,000 ft. The continuous icing envelope for stratiform clouds is defined in [44, Fig. 2] as the ambient temperature as a function of the pressure altitude and in [44, Fig. 3] as the LWC as a function of the cloud horizontal extent. The intermittent maximum icing for cumuliform clouds is defined in [44, Fig. 4] as the LWC as a function of the mean effective droplet diameter, in the range 4000 to 22,000 ft and a horizontal extent standard distance of 2.6 nautical miles. In [44, Fig. 5], the intermittent icing envelope is specified using the ambient temperature as a function of the pressure altitude. In [44, Fig. 6], the intermittent icing envelope is defined by the LWC as a function of the cloud horizontal extent.

Typically, [44] is used by selecting a droplet MVD and a temperature appropriate to the flight level of concern, and then obtaining the LWC from [44, Fig. 1] and [44, Fig. 2] or [44, Fig. 4] and [44, Fig. 5] based on these parameters. The reference distances which [44, Fig. 1] and [44, Fig. 4] are valid for were recommended in [46] as appropriate distances for ice protection systems design. If another distance is desired, a factor obtained from [44, Fig. 3] or [44, Fig. 6] can be used to adjust the LWC value.

The objective of the icing certification is to verify that the airplane has functioning ice protection and to ensure that the airplane's performance and handling qualities within the icing envelopes are acceptable. Specifically, the certification includes testing and analysis of holding the airplane in significant icing conditions for up to 45 minutes. In [47], it is stated that a 45 minutes hold criterion in icing conditions should be evaluated based on the information given in [48]. To reduce the number of test configurations, only the most critical cases can be considered in the analysis.

In case an airplane arriving to the final destination cannot land immediately due to e.g., traffic congestion, poor weather conditions, or runway unavailability, the airplane needs to enter a holding procedure. During the holding, the airplane is kept within a specified airspace while awaiting further clearance. Due to the duration of exposure, the holding is a critical consideration for the design of ice protection systems and for the definition of the icing certification limitations.[48]

3
Methods

Firstly, the architecture of the databank is described. Secondly, the selection, gathering, and postprocessing of the CFD data are explained. Finally, the methods used to cover additional aerodynamic effects, which was not covered by the CFD simulations, are presented.

3.1 The architecture of the databank model

The software and programming language that was used for developing the aerodynamic databank model is MATLAB, including the extension Simulink. Simulink is a graphical programming environment for modeling, simulating and analyzing dynamic systems. As it is specifically useful for stability and control analysis, Simulink was considered as the most convenient choice of platform for developing the full 6DOF airplane model. For convenience, also the aerodynamic databank model was developed in Simulink, as it is a subsystem of the full 6DOF airplane model. By developing the aerodynamic databank model in Simulink, an overview of the model was automatically created. This made it easier to follow the calculations which are performed within the model. In addition, a MATLAB program for testing the aerodynamic databank model was developed. This program allows the user to define certain parameter values and run the aerodynamic databank model. For validation of the model, the program produces plots of the aerodynamic coefficients for e.g., varying angle of attack, which can be compared with the original CFD data.

Analysis of the stability and control, flight performance, and handling qualities of the considered airplane is performed using a 6DOF simulation model. In order to determine the motion of the airplane, flight simulations need information about the aerodynamic forces and moments, which in turn are determined based on the nondimensional aerodynamic coefficients. The aerodynamic data are discrete, whereas the 6DOF airplane model requires data at arbitrary values. This problem was solved by using an interpolation algorithm. Since the aerodynamic coefficients depend on a large number of variables, it is mathematically difficult to design an interpolation algorithm for such multidimensional lookup table. Additionally, it can be computationally expensive, and provide little physical insight. To make the aerodynamic databank more convenient to handle, a component build-up approach was adopted. The main idea behind the component build-up approach is that the total aerodynamic coefficients and the corresponding forces and moments are aggregates of the contributions from the individual airplane components. The relevant aerodynamic

effects are added to the appropriate airplane components.

The lowest level in the databank model is a value or a status indicator, which does not contain any other components. For instance, it can be the baseline lift coefficient of the wing or a flag for landing gear deployment. For interpolation and extrapolation of the lookup tables in the aerodynamic databank model, linear interpolation was used. An exception is the baseline drag coefficients which were extrapolated as described in Section 3.5.

The first block in the execution order of the aerodynamic databank model calculates the local angles of the different airplane components. The wing and body, nacelles, horizontal tail, and vertical tail are given individual changes in aerodynamic angles corresponding to wind gusts and angular rates. Next in the execution order is six parallel blocks, each covering one aerodynamic coefficient. These blocks may contain the baseline aerodynamic coefficients, and contributions due to the Mach number, side slip angle, control surface deflections, ground effect, and landing gear, depending on the coefficient. The following block calculates the dynamic coefficients using the implemented equation for each of them. Next, the propeller effect is executed. The total aerodynamic coefficients are then calculated by adding the different airplane components and contributions due to different aerodynamic effects. Transformation from the wind reference system to the stability reference system and body reference system, respectively, is then performed in two additional blocks. Finally, the aerodynamic forces and moments are calculated and sent to other subsystems in the 6DOF simulation model.

The input data to the aerodynamic databank were gathered from CFD simulations performed by engineers at Heart Aerospace. Certain postprocessing of the CFD data was performed in this study before the data were fed into the databank. Mathematical, semi-empirical, and empirical methods were used to model contributions to the aerodynamic forces and moments that were not covered by the CFD simulations. These models require the airplane's geometrical data and mass properties, so in addition to the CFD data, also this information is input to the databank. The different mass properties cases used in this study are seen in Figure 3.1, where the mass of the airplane is a function of the CoG location relative to the mean aerodynamic chord (MAC). These mass properties cases correspond to the limits of the CoG envelope of the considered airplane. The points referred to as forward (fwd) are located further ahead of the CoP in comparison to the points referred to as aft, which are located closer to the CoP. Due to confidentiality reasons, the values are removed from the CoG envelope.

Furthermore, in order to obtain an output from the aerodynamic databank, the variables presented in Table 3.1 need to be defined. When using the aerodynamic databank as a subsystem in the 6DOF simulation model, these variables are obtained from other subsystems which manage the equations of motion, flight controls, propulsion, flight conditions, and atmospheric conditions. The Euler angle θ is used for calculating the height above ground of the horizontal tail.

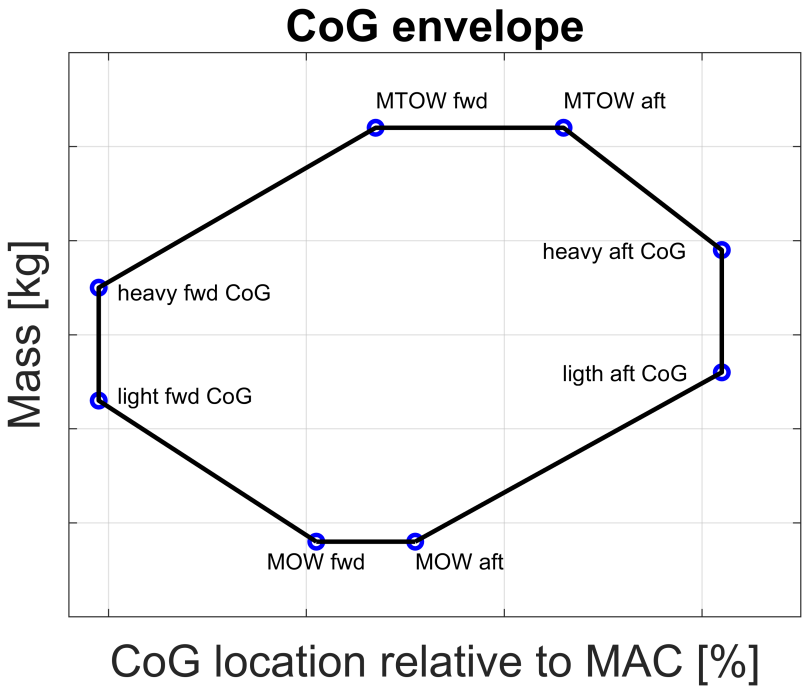

Figure 3.1: The CoG envelope of the considered airplane

Table 3.1: The input variables to the aerodynamic databank model

Quantity	Unit
altitude (h)	m
gravitational acceleration (g)	m/s^2
angle of attack (α)	$^\circ$
time derivative of the angle of attack ($\dot{\alpha}$)	$^\circ/s$
side slip angle (β)	$^\circ$
time derivative of the side slip angle ($\dot{\beta}$)	$^\circ/s$
Mach number (M)	
Roll angular velocity (p)	rad/s
Pitch angular velocity (q)	rad/s
Yaw angular velocity (r)	rad/s
Flap deflection left and right	$^\circ$
Aileron deflection left and right	$^\circ$
Elevator deflection	$^\circ$
Rudder deflection	$^\circ$
Euler angles ($\{\psi, \theta, \phi\}$)	rad
Wind velocity ($\{u, v, w\}$)	m/s
Landing gear deployment	
Propeller power coefficient (C_p)	

3.2 Conversion between reference systems

Input and output values to and from the aerodynamic databank model may require conversion between the wind reference frame and the body reference frame or the stability reference frame. One three-dimensional Cartesian coordinate system can, according to Euler's rotation theorem, be transformed to another three-dimensional Cartesian coordinate system that has a common origin with the former through a sequence of one to three rotations about the orthogonal axes. In aerospace, the rotations are performed using the Tait-Bryan convention, using the intrinsic rotation definition. Intrinsic rotations are rotations performed on the rotating coordinate system, which is initially aligned with the coordinate system that is fixed to the body. The rotations about the longitudinal, lateral, and vertical axes are referred to as yaw, pitch, and roll, respectively. Each rotation is represented by a rotation matrix. The multiplication of the rotation matrices must be performed in a specific order.[49]

The stability reference frame is obtained from the wind reference frame by rotation equal to the side slip angle about the X_W-axis. Hence, the transformation matrix from the wind coordinate system to the stability coordinate system is

$$R_{WS} = \begin{bmatrix} \cos\beta & -\sin\beta & 0 \\ \sin\beta & \cos\beta & 0 \\ 0 & 0 & 1 \end{bmatrix}. \tag{3.1}$$

The aerodynamic coefficients given in the stability reference system are

$$C_{D,\,s} = C_D \cos\beta + C_y \sin\beta, \tag{3.2}$$

$$C_{y,\,s} = C_y \cos\beta - C_D \sin\beta, \tag{3.3}$$

$$C_{L,\,s} = C_L, \tag{3.4}$$

$$C_{r,\,s} = C_r \cos\beta + \frac{c}{b} C_m \sin\beta, \tag{3.5}$$

$$C_{m,\,s} = C_m \cos\beta + \frac{b}{c} C_r \sin\beta, \tag{3.6}$$

and

$$C_{n,\,s} = C_n, \tag{3.7}$$

where the wing span and the chord length are used to nondimensionalize the stability moment coefficients.

The body reference system deviates from the wind reference system with both aerodynamic angles. Hence, the transformation from the wind coordinate system to the body coordinate system is obtained by rotating the stability reference system an angle equal to the angle of attack about the Y_S-axis, i.e.,

$$\begin{aligned} R_{WB} &= \begin{bmatrix} \cos\alpha & 0 & -\sin\alpha \\ 0 & 1 & 0 \\ \sin\alpha & 0 & \cos\alpha \end{bmatrix} R_{WS} = \begin{bmatrix} \cos\alpha & 0 & -\sin\alpha \\ 0 & 1 & 0 \\ \sin\alpha & 0 & \cos\alpha \end{bmatrix} \begin{bmatrix} \cos\beta & -\sin\beta & 0 \\ \sin\beta & \cos\beta & 0 \\ 0 & 0 & 1 \end{bmatrix} \\ &= \begin{bmatrix} \cos\alpha\cos\beta & -\cos\alpha\sin\beta & -\sin\alpha \\ \sin\beta & \cos\beta & 0 \\ \sin\alpha\cos\beta & -\sin\alpha\sin\beta & \cos\alpha \end{bmatrix}. \end{aligned} \tag{3.8}$$

The aerodynamic coefficients given in the body reference frame are

$$C_{D,b} = \sin\alpha C_L - \cos\alpha\cos\beta C_D - \cos\alpha\sin\beta C_y, \tag{3.9}$$

$$C_{y,b} = C_y\cos\beta - C_D\sin\beta, \tag{3.10}$$

$$C_{L,b} = -\cos\alpha C_L - \cos\beta\sin\alpha C_D - \sin\alpha\sin\beta C_y, \tag{3.11}$$

$$C_{r,b} = C_R\cos\beta\cos\alpha - C_m\sin\beta\frac{c}{b} - C_n\sin\alpha, \tag{3.12}$$

$$C_{m,b} = C_R\sin\beta\frac{b}{c} + C_m\cos\beta, \tag{3.13}$$

and

$$C_{n,b} = C_r\sin\alpha + C_n\cos\alpha, \tag{3.14}$$

where the wing span and the chord length are used to nondimensionalize the body moment coefficients.

3.3 CFD data

The CFD data serving as input data to the aerodynamic databank model were obtained from CFD simulations of the flow around the considered airplane, performed by engineers at Heart Aerospace. As mentioned in 1.3, these CFD simulations were not a part of this study.

3.3.1 CFD simulations

The software used for the CFD simulations was Star-CCM+. In the Reynolds-averaged Navier-Stokes (RANS) simulations, the flow around the airplane was computed by using a finite volume method in which the flow was assumed to be governed by the RANS equations. Furthermore, a coupled solver was used, i.e., the continuity, momentum, and energy equations were solved simultaneously. To model the turbulent stresses and thereby close the equation system, the turbulence model referred to as Menter's Shear Stress Transport (SST) model was used. In the case of an inviscid flow assumption, the RANS equations were reduced to the Euler equations. The aerodynamic coefficients were calculated for the entire airplane as well as for the airplane components, including the wings, fuselage, nacelles, horizontal, and vertical tail.

The baseline aerodynamic coefficients are functions of the angle of attack and the flap deflection and were obtained from CFD-RANS simulations using a half-model of the airplane. The sweep of side slip angle values was performed by CFD-RANS simulations and a full model of the airplane. The other contributions to the coefficients were obtained from CFD-Euler simulations, divided into longitudinal and lateral effects. The longitudinal contributions are due to deflection of the ailerons and the elevator at different angles of attack, Mach numbers, and altitudes. The sweep of the aileron deflection and elevator deflection, respectively, was performed using a half-span model of the airplane. The lateral contributions are due to deflection of

the ailerons for different side slip angles, and deflection of the rudder for different angles of attack and side slip angles. The rudder deflection sweep was performed using the full model of the airplane. All the contributions to the aerodynamic coefficients based on the CFD-Euler simulations are added as a componentwise difference to the componentwise baseline aerodynamic coefficients.

The simulations of the propellers were made in Star-CCM+ using a blade element method with a time averaged approach. The rotational speed and the pitch angle of the propeller were set to fixed values.

3.4 Friction drag

Due to insufficient resolution of the viscous effects in the CFD simulations, the minimum drag of the empennage was underestimated. The minimum drag coefficients for the horizontal and vertical tails were therefore corrected using a program called FRICTION from the Virginia Tech Aerodynamics and Design Software Collection [50]. The program gives an estimate of the laminar and turbulent skin friction and form drag and is suitable to use in aircraft preliminary design. The input parameters to FRICTION are either the Mach and altitude, or the Mach and Reynolds number, as well as relevant geometrical data, and the flow type. The output, i.e., the skin friction estimate, is based on flat plate skin friction formulas and form factors.

The zero-lift drag coefficient for a certain component is obtained as

$$C_{D,0} = \frac{FF\, C_f\, S_{wet}}{S_{ref}}, \tag{3.15}$$

where FF is the form factor accounting for the pressure drag of the component, C_f is the skin friction coefficient for either laminar or turbulent flow, calculated by using the Blasius formula and the van Driest method, respectively, and S_{wet} is the wetted area.[50]

3.5 Correction and extrapolation of the drag coefficient

The drag coefficient as a function of the angle of attack obtained from CFD simulations needed to be corrected since the flow close to the surfaces was not resolved, causing an underestimation of the drag. The total drag coefficient for each flap configuration was compared with the performance drag polar data. The parabolic drag polar expressed as (2.40) can be rewritten as

$$C_{D,tot} = C_{D,0} + KC_L^2, \tag{3.16}$$

where

$$K = \frac{1}{\pi Ae}. \tag{3.17}$$

The performance drag polar data include maximum lift coefficients for different flap configurations which correspond to targets which are required in order to fulfill the desired performance of the airplane. The zero-lift drag coefficient in the performance drag polar data was estimated using a parametric method including a study of similar airplanes combined with the principle of equivalent skin-friction. The factor K is was estimated based on the wing aspect ratio and by the empirical expression (2.41).

The zero-lift drag coefficient $C_{D,0}$ and the factor K based on the CFD data points were obtained by curve fitting of (3.16). Only the points in the domain corresponding to the linear region of the lift coefficient were included in the curve fitting. The corrected values of the total drag coefficient for each flap deflection were obtained as

$$C_{D,corrected} = C_{D,0} + (C_{D,performance} - C_{D,0}) + (K_{performance} - K)C_L^2. \tag{3.18}$$

The corrected values for each airplane component were then obtained as the proportion of each component's drag coefficient of the difference in the total drag coefficient.

Extrapolation was used to obtain drag coefficients for negative values of the angle of attack. This was achieved by performing curve fitting of a second order polynomial. The curve fitting considered only the points in the domain corresponding to the linear domain of the lift coefficient. Furthermore, the coefficients of the second order polynomial used for the curve fitting were limited to only take positive values in order to ensure that the curve of the drag coefficient is convex, i.e., that the drag coefficient is increasing for increasing magnitude of the angle of attack. For the same reason, the extrapolated curve for the 35° flap deflection uses the same equation as for the 15° flap deflection, as it proved to give more realistic results. A similar result can be obtained by performing the curve fitting of the data points for the 35° flap deflection, with the second term in the general form of the second order polynomial set to zero, i.e.,

$$f(x) = p_1x^2 + p_2x + p_3 = \{p_2 = 0\} = p_1x^2 + p_3. \tag{3.19}$$

For the horizontal tail, this method gave a more realistic result than the former. To obtain a realistic result for the drag coefficient of the vertical tail, it was instead the polynomial constants corresponding to 35° flap deflection that was used also for the drag coefficient curve for 15° flap deflection.

3.5.1 Baseline aerodynamic coefficients

The drag, lift, and pitching moment coefficients as functions of the angle of attack and flap deflection are the primary contributions to the aerodynamic forces and moments. For the individual components, i.e., the wing, fuselage, nacelle, horizontal tail, and vertical tail, the baseline aerodynamic coefficients were obtained for a set of angles of attack in degrees equal to {0, 6, 8, 10, 12, 14, 16, 18} and flap deflections of 0°, 15°, and 35°. These sweeps of the angle of attack and flap deflections were performed in CFD-RANS simulations. As the airplane is assumed to be symmetric

about the longitudinal axis, the baseline side force, rolling moment, and yawing moment coefficients were assumed to be zero.

3.5.2 Side slip contribution

The side slip effect on the aerodynamic forces and moments was based on CFD-RANS data for all six aerodynamic coefficients per component as functions of side slip angle and angle of attack. The set of side slip angle values in degrees is {0, 2, 4, 6, 8, 10} and the angle of attack values were 0° and 4°. The Mach number was set to 0.1512 in the CFD-RANS simulations. To cover also negative values of the side slip angle in the aerodynamic databank model, curves for the drag, lift, and pitching moment coefficients were mirrored about the y-axis, such that the value of the coefficients will be the same irrespective of the sign of the side slip angle value. The side force, rolling moment, and yawing moment coefficients have instead opposite sign for opposite sign of the side slip value.

3.5.3 Local angles

The contribution to the angle of attack due to gusts was obtained as

$$\Delta\alpha_{gust} = \arctan\left(\frac{w_{gust}}{TAS}\right), \tag{3.20}$$

where w_{gust} is the wind velocity in the vertical direction, and TAS is the true air speed. In a similar way, the change in side slip angle due to gusts was obtained as

$$\Delta\beta_{gust} = \arcsin\left(\frac{v_{gust}}{TAS}\right), \tag{3.21}$$

where v_{gust} is the wind velocity in the lateral direction.

The angle of attack of the airplane wing and body is obtained was

$$\alpha_{WB} = \alpha + \Delta\alpha_{gust} + (\Delta\alpha)_G, \tag{3.22}$$

where α is the angle of attack of the entire airplane, $\Delta\alpha_{gust}$ is the gust contribution, and $(\Delta\alpha)_G$ is change in the angle of attack due to the ground effect. The side slip angle of the airplane wing and body is the side slip angle of the entire airplane plus a possible contribution from gusts, i.e.,

$$\beta_{WB} = \beta + \Delta\beta_{gust}. \tag{3.23}$$

The horizontal tail angle of attack was calculated as

$$\alpha_{HT} = \alpha + \Delta\alpha_{gust} + \Delta\alpha_{q,\,HT} + \Delta\alpha_{\dot{\alpha},\,HT} + (\Delta\alpha_{HT})_G, \tag{3.24}$$

where α is the airplane angle of attack, $\Delta\alpha_{gust}$ is contribution due to wind gusts, $\Delta\alpha_{q,\,HT}$ is the contribution due to pitch rate, $\Delta\alpha_{\dot{\alpha},\,HT}$ is the contribution due to the

rate of change of airplane angle of attack, and $(\Delta\alpha_{HT})_G$ is the contribution due to ground effect. The change in angle of attack of the horizontal tail due to the pitch rate was obtained as

$$\Delta\alpha_{q,\,HT} = \frac{\Delta x_{HT\,ref}\, q}{TAS}, \tag{3.25}$$

where $\Delta x_{HT\,ref}$ is the longitudinal distance from the airplane's CoG to the reference point of the horizontal tail, q is the pitch rate. The change in angle of attack of the horizontal tail due to the rate of change of airplane angle of attack was obtained as

$$\Delta\alpha_{\dot{\alpha},\,HT} = \frac{\Delta x_{HT\,ref}\, \dot{\alpha}}{TAS}. \tag{3.26}$$

The contributions to the side slip angle of the vertical tail are the airplane side slip angle, gusts, roll rate, yaw rate, and rate of change of the airplane side slip angle and was calculated as

$$\beta_{VT} = \beta + \Delta\beta_{gust} + \Delta\beta_{p,\,VT} + \Delta\beta_{r,\,VT} + \Delta\beta_{\dot{\beta},VT}. \tag{3.27}$$

The change in side slip angle of the vertical tail due to the roll rate was obtained as

$$\Delta\beta_{p,\,VT} = \frac{\Delta z_{VT\,ref}\, p}{TAS}, \tag{3.28}$$

where $\Delta z_{VT\,ref}$ is the vertical distance from the airplane's CoG to the reference point of the horizontal tail, p is the roll rate. The change in side slip angle of the vertical tail due to the yaw rate was obtained as

$$\Delta\beta_{r,\,VT} = -\frac{\Delta x_{VT\,ref}\, r}{TAS}, \tag{3.29}$$

where $\Delta x_{VT\,ref}$ is the longitudinal distance from the airplane's CoG to the reference point of the horizontal tail. The change in side slip angle of the vertical tail due to the rate of change of airplane side slip angle was obtained as

$$\Delta\beta_{\dot{\beta},\,VT} = \frac{\Delta x_{VT\,ref}\dot{\beta}}{TAS}. \tag{3.30}$$

The angle of attack of each nacelle has contributions from the aircraft angle of attack, gusts, roll rate, pitch rate, and rate of change of the airplane angle of attack and was calculated as

$$\alpha_{nac} = \Delta\alpha_{gust} + \Delta\alpha_{p,\,nac} + \Delta\alpha_{q,\,nac} + \Delta\alpha_{\dot{\alpha},\,nac}. \tag{3.31}$$

The change in angle of attack of the nacelle due to the roll rate was obtained as

$$\Delta\alpha_{p,\,nac} = \frac{\Delta y_{nac\,ref}\, p}{TAS}, \tag{3.32}$$

where Δy_{nacref} is the lateral distance from the airplane's CoG to the reference point of the nacelle, p is the roll rate. The change in angle of attack of the nacelle due to the pitch rate was obtained as

$$\Delta\alpha_{q,\,nac} = \frac{\Delta x_{nacref,\,q}}{TAS}, \tag{3.33}$$

where Δx_{nacref} is the longitudinal distance from the airplane's CoG to the reference point of the nacelle, q is the pitch rate. The change in angle of attack of the nacelle due to the rate of change of airplane angle of attack was obtained as

$$\Delta\alpha_{\dot{\alpha},\,nac} = \frac{\Delta x_{nacref}\,\dot{\alpha}}{TAS}. \tag{3.34}$$

The side slip angle of each nacelle is the sum of the airplane side slip angle and the contributions due to gusts, roll rate, yaw rate, and rate of change of the airplane side slip angle and was calculated as

$$\beta_{nac} = \Delta\beta_{gust} + \Delta\beta_{p,\,nac} + \Delta\beta_{r,\,nac} + \Delta\beta_{\dot{\beta},\,nac}. \tag{3.35}$$

The change in side slip angle of the nacelle due to the roll rate was obtained as

$$\Delta\beta_{p,\,nac} = \frac{\Delta z_{nacref}\,p}{TAS}, \tag{3.36}$$

where Δz_{nacref} is the vertical distance from the airplane's CoG to the reference point of the nacelle, p is the roll rate. The change in side slip angle of the nacelle due to the yaw rate was obtained as

$$\Delta\beta_{r,\,nac} = -\frac{\Delta x_{nacref}\,r}{TAS}, \tag{3.37}$$

where Δx_{nacref} is the longitudinal distance from the airplane's CoG to the reference point of the nacelle. The change in side slip angle of the nacelle due to the rate of change of airplane side slip angle was obtained as

$$\Delta\beta_{\dot{\beta},\,nac} = \frac{\Delta x_{nacref}\,\dot{\beta}}{TAS}. \tag{3.38}$$

3.5.4 Rudder deflection

The effect on the aerodynamic forces and moments due to rudder deflection is accounted for by CFD-Euler data for all six aerodynamic coefficients per component as functions of rudder deflection, angle of attack, and Mach number. The CFD simulations were carried out for rudder deflections of 0°, 10°, and 20°. To cover rudder deflections in both directions in the aerodynamic databank model, the CFD data for the drag, lift, and pitching moment coefficients were mirrored about the y-axis, such that the value of the coefficients will be the same irrespective of the sign of the side slip angle value. The side force, rolling moment, and yawing moment coefficients valid for negative rudder deflection values were both mirrored about the lateral axis and have a switched sign. The CFD data have a range of the angle of attack in degrees equal to the set $\{-4,\ -2,\ 0,\ 2,\ 4,\ 8,\ 12,\ 16\}$ and the Mach numbers are 0.1512 and 0.4189.

3.5.5 Aileron deflection

The CFD aileron sweep was performed for aileron deflections of -20°, -10°, 10°, and 20°. The angle of attack values in degrees are $\{-4, -2, 0, 2, 4, 8, 12, 16\}$, and the Mach numbers are 0.1512 and 0.4189. At zero aileron deflection, the contribution to the aerodynamic coefficients is zero. The aileron effect has a contribution to all six aerodynamic coefficients and all individual airplane components.

3.5.6 Elevator deflection

The elevator contribution to each total aerodynamic coefficient was based on CFD data including the aerodynamic coefficients for each airplane component as functions of elevator deflection, angle of attack, and Mach number. The elevator deflections that were covered by the CFD simulations are -20°, -10°, 10°, and 20°. The angle of attack values in degrees are $\{-4, -2, 0, 2, 4, 8, 12, 16\}$ and the Mach numbers are 0.1512 and 0.4189. At 0° elevator deflection, the elevator contribution to the aerodynamic coefficients is zero. Furthermore, the elevator deflection is assumed to not affect the side force, rolling moment, and yawing moment coefficients.

3.5.7 Mach effect

The contribution to the total aerodynamic forces and moments due to the Mach effect was based on CFD-Euler simulations performed for Mach numbers of 0.1512 and 0.4189. A Mach factor was calculated for the drag, lift, and pitching moment coefficients per airplane component. The side force, rolling moment, and pitching moment coefficients were assumed to have a Mach effect contribution only to the wing component. The factor was set to 1 for a Mach number of 0.1512 and was linearly interpolated to the considered Mach number.

3.5.8 Propeller effect

The difference in the drag, lift, and pitching moment coefficients for respective components due to the propellers was determined by CFD simulations of an airplane configuration including the propellers. The propeller power coefficient was set to 0.61, the angle of attack values were taken as the integers from -4° to 18° and the Mach number was set to 0.1512. The propeller effect on the side force coefficient was neglected completely. The difference in wing rolling moment coefficient due to the propeller effect was calculated as

$$(\Delta C_{r,W})_{prop} = (\Delta C_{L,W})_{prop}\frac{y_{prop}}{b} - (\Delta C_{y,W})_{prop}\frac{z_{prop}}{b} = \{(\Delta C_{y,W})_{prop} \approx 0\} = (\Delta C_{L,W})_{prop}\frac{y_{prop}}{b}, \tag{3.39}$$

where y_{prop} is the lateral distance from CoG to the propeller AC, $(\Delta C_{L,W})_{prop}$ is the difference in wing lift coefficient due to the propeller slipstream, and z_{prop} is the vertical distance from CoG to the propeller AC. The difference in nacelle rolling

moment coefficient due to the propeller effect was calculated as

$$\begin{aligned}(\Delta C_{r,\,nac})_{prop} &= (\Delta C_{L,\,nac})_{prop}\frac{y_{prop}}{b} - (\Delta C_{y,\,nac})_{prop}\frac{z_{prop}}{b} \\ &= \{(\Delta C_{y,\,nac})_{prop} \approx 0\} = (\Delta C_{L,\,nac})_{prop}\frac{y_{prop}}{b}.\end{aligned} \tag{3.40}$$

The differences in the rolling moment coefficients for the other airplane components due to the propeller effect were neglected. The difference in wing yawing moment coefficient due to the propeller effect was calculated as

$$(\Delta C_{n,\,W})_{prop} = -(\Delta C_{D,\,W})_{prop}\frac{y_{prop}}{b}. \tag{3.41}$$

The difference in nacelle yawing moment coefficient due to the propeller effect was calculated as

$$(\Delta C_{n,\,nac})_{prop} = -(\Delta C_{D,\,nac})_{prop}\frac{y_{prop}}{b}. \tag{3.42}$$

The differences in the yawing moment coefficients for the other airplane components due to the propeller effect were neglected.

3.5.9 Change in coefficients due to landing gear deployment

The increase in drag due to deployment of the landing gear was estimated according to [24]. The considered airplane has a retractable landing gear consisting of a main gear with two legs and a nose gear. The drag coefficient for the landing gear is a function of the frontal area and the reference area of the landing gear. For the main gear, the reference area is the product of the width of the landing gear and the distance from the ground to the fuselage attachment point of the landing gear. The reference area of the nose gear is the product of the distance from the ground to the fuselage attachment point of the landing gear and the tire diameter. The total drag coefficient accounting for the landing gear alone was calculated as

$$C_{D,\,gear} = \frac{\sum_i \left(C_{D,\,gear,\,L=0}\right)_i \left(S_{gear}\right)_i}{S}, \tag{3.43}$$

where $C_{D,\,gear,\,L=0}$ is the zero-lift drag coefficient of the landing gear based on its reference area obtained from [24], and S_{gear} is the reference area for the specific landing gear type.

The landing gear gives a negative contribution to the pitching moment and was calculated as

$$C_{m,\,gear} = C_{D,\,nose\,gear}\frac{l_{nose\,gear}}{\overline{c}} + C_{D,\,main\,gear}\frac{l_{main\,gear}}{\overline{c}}, \tag{3.44}$$

where $l_{nose\,gear}$ is the vertical distance from the nose gear CoP to the wing reference point and $l_{main\,gear}$ is the vertical distance from the main gear CoP to the wing reference point.

3.5.10 Ground effect

The ground effects on lift, pitching moment, and drag were estimated according to the methods in [1].

The change in lift due to ground effects has two components, the change in wing-body lift and the change in tail-body lift due to the effects of downwash. The former component is generally small compared to the latter and is neglected in the method in [1]. The method for estimating the ground effects on lift includes the induced effects of the reflected bound vortex and wing thickness, and effects of taper ratio, sweep-back, dihedral, and flap deflection. The effects of the wing thickness are neglected. The change in wing-body angle of attack at a constant lift coefficient due to ground with respect to the out-of-ground-effect lift curve is given by

$$(\Delta\alpha)_G = -\left(\frac{9.12}{A} + 7.16\left(\frac{c_r}{b}\right)\right)(C_{L,f})_{WB}\, x - \frac{A}{2\,(C_{L,\alpha})_{WB}}\left(\frac{c_r}{b}\right) \left(\frac{L}{L_0} - 1\right)(C_{L,f})_{WB}\, r - \frac{(\delta_f/50)^2}{(C_{L,\alpha})_{WB}}\Delta\,(\Delta C_L)_{flap}\,, \tag{3.45}$$

where c_r is the wing root chord, $(C_{L,f})_{WB}$ is the wing-body lift coefficient including flap effects, x is a parameter accounting for the effects on lift due to trailing vortices obtained from [1, Fig. 4.7.1-14] as a function of wing geometry and the wing height above ground, $(C_{L,\alpha})_{WB}$ is the wing-body lift curve slope, $L/L_0 - 1$ is a parameter accounting for the ground effect on lift due to bound vortices obtained from [1, Fig. 4.7.1-15] as a function of wing geometry, lift coefficient, and the height of the quarter-chord point of the wing root chord above the ground, r is a parameter accounting for the effect of finite span obtained from [1, Fig. 4.7.1-16] as a function of wing height above the ground, δ_f is the flap deflection angle, and $\Delta\,(\Delta C_L)_{flap}$ is a factor accounting for the effect of flap deflection obtained from [1, Fig. 4.7.1-17] as a function of the height of the quarter-chord point of the wing root chord above the ground.

The change in downwash due to ground effects in the linear lift range is given by

$$(\Delta\epsilon)_G = \epsilon\left(\frac{b_{eff}^2 + 4\,(H_H - H)^2}{b_{eff}^2 + 4\,(H_H + H)^2}\right), \tag{3.46}$$

where $(\Delta\epsilon)_G$ is the difference between the downwash in free air and the downwash in ground effect, ϵ is the downwash out of ground effect, H is the height of the wing mean quarter chord above the ground, H_H is the height of the horizontal tail mean quarter chord above ground, and b_{eff} is the effective wing span defined as

$$b_{eff} = \frac{C_{L,WB} + \Delta C_{L,f}}{\frac{C_{L,WB}}{b'_w} + \frac{\Delta C_{L,f}}{b'_f}}, \tag{3.47}$$

where $C_{L,WB}$ is the wing-body lift coefficient for retracted flaps, $\Delta C_{L,f}$ is the change in lift coefficient due to flaps, b'_w is obtained from Figure [1, Fig. 4.7.1-18] as a function of aspect ratio and taper ratio, and b'_f is obtained from Figure [1, Fig. 4.7.1-18]

as a function of the ratio of flap span to wing span.

The ground effect on the horizontal tail lift curve was obtained using the following relationship.

$$(\Delta\alpha_{HT})_G = -(\Delta\epsilon)_G \tag{3.48}$$

The change in pitching moment due to ground effects is primarily due to to the change in lift on the horizontal tail due to the change in downwash. Additionally, the pitching moment is increased by the increased lift on the wing. Any possible change in the AC location due to the ground effect, which increases the pitching moment, is neglected. The total change in the pitching moment coefficient due to ground effects is the sum of the changes of the horizontal tail and the wing-body pitching moment components, i.e.,

$$(\Delta C_m)_G = (\Delta C_{m,\,HT})_G + (\Delta C_{m,\,WB})_G\,, \tag{3.49}$$

where

$$(\Delta C_{m,\,HT})_G = -(\Delta C_{L,\,HT})_G \frac{l_{HT}}{\overline{c}} \frac{S_H}{S_W} \frac{q_H}{q_\infty}, \tag{3.50}$$

where $(\Delta C_{L,\,HT})_G$ is the change in lift on the horizontal tail at given angle of attack due to the ground effect obtained from CFD data, l_{HT} is the distance from the quarter chord point of the horizontal tail MAC to the moment reference center, $\overline{c}$ is the wing MAC, S_H/S_W is the ratio of the horizontal tail area to the wing area, and q_H/q_∞ is the effective dynamic pressure ratio at the horizontal tail given by

$$\frac{q_H}{q_\infty} = 1 - \frac{2.42\,(C_{D,\,0})^{1/2}}{\frac{x}{\overline{c}} + 0.30} \cos^2\left(\frac{\pi}{2}\frac{z}{z_w}\right), \tag{3.51}$$

where $C_{D,\,0}$ is the wing zero-lift drag coefficient, x is the longitudinal distance measured along the wake center line from the wing root chord trailing edge, and z is the vertical distance from the vortex sheet to the point of interest, that is the quarter-chord point of the MAC. The half-width of the wing wake is given by

$$z_w = 0.68\sqrt{C_{D,\,0}\left(\frac{x}{\overline{c}} + 0.15\right)}. \tag{3.52}$$

The downwash was estimated by

$$\epsilon = \frac{1.62(C_{L,\,0} + C_{L,\,\alpha}\alpha)}{\pi A}. \tag{3.53}$$

The change in pitching moment coefficient of the wing-body due to ground effects is given by

$$(\Delta C_{m,\,WB})_G = \left(n - \frac{x_{AC}}{\overline{c}}\right)(\Delta C_{L,\,WB})_G\,, \tag{3.54}$$

where n is the distance from the wing apex to the moment reference center measured in wing MAC, x_{AC} is the wing-body AC location measured from the wing apex (positive for AC aft of wing apex), and $(\Delta C_{L,WB})_G$ is the change in lift due to the ground effect on the wing-body.

The ground effects on drag are divided into a decrease in drag due to lift, a change in the drag at zero lift, a pitching moment increment which changes the drag due to lift of the trimmed airplane. The second effect was neglected since it is small compared to the change in drag due to lift. The difference in drag due to lift is given by

$$(\Delta C_{D,L})_G = -\frac{\sigma C_L^2}{\pi A} - \left(C_D - \frac{\sigma C_L^2}{\pi A}\right)\frac{rTC_L}{57.3}, \tag{3.55}$$

where σ is the Prandtl's interference coefficient, and T is a factor accounting for the reduction of longitudinal velocity obtained from Figure [1, Fig. 4.7.1-20] as a function of wing height above ground.

3.6 Dynamic derivatives

While developing an airplane, the dynamic derivatives need to be obtained based on the airplane geometry. Furthermore, it is more cost-effective to estimate the dynamic derivatives estimated from the airplane geometry than by CFD simulations or flight testing. The initial estimation of the dynamic derivatives can be used to evaluate the airplane concept by predicting its stability and control qualities. These predictions can serve as a basis for decision-making regarding design modifications before performing more complex design evaluations.

In general, the main contributions to the dynamic derivatives are the wing and the tail. The wing dynamic derivatives were estimated using the semi-empirical methods presented in the USAF Stability and Control DATCOM [1]. The methods are valid for the considered airplane up to stall angles of attack, i.e., attached flow conditions. The tail contribution to the dynamic derivatives was calculated as a change in the local angle of the vertical and horizontal tail, respectively, due to a locally induced velocity, as described in [21].

The stability derivative models presented in DATCOM [1] were compared to the models presented in ESDU [2] as well as to values obtained by using the vortex lattice method called AVL. The theory behind this method is described in Section 2.9.1. AVL is a program for aerodynamic and flight dynamic analysis, employing an extended vortex lattice model for the lifting surfaces [51]. As any VLM, AVL assumes inviscid and irrotational flow, thin airfoils, small angles of attack, and small side slip angles. AVL serves well as a method for calculation of the lift distribution and induced drag of a wing with angles of attack corresponding to no significant flow separation. Components such as the fuselage and the nacelles are modeled using slender-body theory but, because of its limitations, it is recommended to neglect these components if it is expected that they have relatively small influence on

the aerodynamic forces and moments. AVL also assumes quasi-steady flow, thus neglecting unsteady vorticity shedding [19]. Consequently, the oscillation period must be much longer than the time it takes the flow to transverse the airfoil chord. Additionally, the roll, pitch, and yaw rates must be slow enough so that the resulting relative flow angles are small. These criteria are unlikely to be violated in any typical flight situation.

ESDU is an engineering advisory organization that provides data, methods, and software for solving complex engineering problems. All the products that ESDU offers are reviewed and approved by independent committees of industrial and academic experts. The Aerospace Engineering package is widely used by the aerospace industry, including e.g., Airbus and Boeing.

3.6.1 Rate of angle of attack derivatives

The rate of angle of attack derivatives are $C_{D,\dot{\alpha}}$, $C_{L,\dot{\alpha}}$, and $C_{m,\dot{\alpha}}$. The $C_{D,\dot{\alpha}}$ derivative is in general small and has negligible effect on longitudinal stability. Usually also the effect of $C_{L,\dot{\alpha}}$ on the longitudinal stability is unimportant and is therefore neglected. The $C_{m,\dot{\alpha}}$ derivative is important in longitudinal dynamics. Only the tail contributions to these derivatives are taken into account as it is typically much larger than the other contributions.[1]

3.6.1.1 Acceleration derivative $C_{D,\dot{\alpha}}$

The horizontal tail contribution to the derivative $C_{D,\dot{\alpha}}$ was calculated as

$$(\Delta C_{D,\dot{\alpha}})_{HT} = (\Delta C_D)_{HT} \frac{2\,\mathrm{TAS}}{\overline{c}}, \tag{3.56}$$

as suggested in [21]. The drag coefficient is a function of the airplane angle of attack and the local angle of attack at the horizontal tail. In the aerodynamic databank model, this drag coefficient is obtained from a lookup table with CFD data for the horizontal tail. The local angle of attack at the horizontal tail was calculated as (3.24).

3.6.1.2 Acceleration derivative $C_{L,\dot{\alpha}}$

The horizontal tail contribution to the derivative $C_{L,\dot{\alpha}}$ was calculated as

$$(\Delta C_{L,\dot{\alpha}})_{HT} = (\Delta C_L)_{HT} \frac{2\,\mathrm{TAS}}{\overline{c}}, \tag{3.57}$$

as suggested in [21]. The lift coefficient is a function of the airplane angle of attack and the local angle of attack at the horizontal tail. In the aerodynamic databank model, this lift coefficient is obtained from a lookup table with CFD data for the horizontal tail. The local angle of attack at the horizontal tail was calculated as (3.24).

3.6.1.3 Acceleration derivative $C_{m,\dot{\alpha}}$

The horizontal tail contribution to the derivative $C_{m,\dot{\alpha}}$ was calculated as

$$(\Delta C_{m,\dot{\alpha}})_{HT} = (\Delta C_m)_{HT} \frac{2\,\mathrm{TAS}}{\bar{c}}, \tag{3.58}$$

as suggested in [21]. The pitching moment coefficient is a function of the airplane angle of attack and the local angle of attack at the horizontal tail. In the aerodynamic databank model, this pitching moment coefficient is obtained from a lookup table with CFD data for the horizontal tail. The local angle of attack at the horizontal tail was calculated as (3.24).

3.6.2 Rate of side slip angle derivatives

The rate of change of the side slip angle yields the derivatives $C_{y,\dot{\beta}}$, $C_{L,\dot{\beta}}$, and $C_{n,\dot{\beta}}$. At low to moderate angles of attack, these derivatives are relatively small and have negligible effect on lateral stability. Only the vertical tail contributions to these derivatives are accounted for, as it is the largest contribution to these derivatives.[1]

3.6.2.1 Acceleration derivative $C_{y,\dot{\beta}}$

The vertical tail contribution to $C_{y,\dot{\beta}}$ was calculated as

$$(\Delta C_{y,\dot{\beta}})_{VT} = (\Delta C_y)_{VT} \frac{2\,\mathrm{TAS}}{b}, \tag{3.59}$$

as suggested in [21]. The side force coefficient is a function of the airplane angle of attack and the local side slip angle at the vertical tail. In the aerodynamic databank model, this side force coefficient is obtained from a lookup table with CFD data for the vertical tail. The local side slip angle at the vertical tail was calculated as (3.27).

3.6.2.2 Acceleration derivative $C_{L,\dot{\beta}}$

The vertical tail contribution to $C_{L,\dot{\beta}}$ was calculated as

$$(\Delta C_{L,\dot{\beta}})_{VT} = (\Delta C_L)_{VT} \frac{2\,\mathrm{TAS}}{b}, \tag{3.60}$$

as suggested in [21]. The lift coefficient is a function of the airplane angle of attack and the local side slip angle at the vertical tail. In the aerodynamic databank model, this lift coefficient is obtained from a lookup table with CFD data for the vertical tail. The local side slip angle at the vertical tail was calculated as (3.27).

3.6.2.3 Acceleration derivative $C_{n,\dot{\beta}}$

The vertical tail contribution to $C_{n,\dot{\beta}}$ was calculated as

$$(\Delta C_{n,\dot{\beta}})_{VT} = (\Delta C_n)_{VT} \frac{2\,\mathrm{TAS}}{b}, \tag{3.61}$$

as suggested in [21]. The yawing moment coefficient is a function of the airplane angle of attack and the local side slip angle at the vertical tail. In the aerodynamic databank model, this yawing moment coefficient is obtained from a lookup table with CFD data for the vertical tail. The local side slip angle at the vertical tail was calculated as (3.27).

3.6.3 Roll rate derivative $C_{y,p}$

3.6.3.1 Datcom

The wing contribution to the derivative $C_{y,p}$ was approximated as

$$(C_{y,p})_W = K\left(\left(\frac{C_{y,p}}{C_L}\right)_{C_L=0,\,M} C_L\right) + (\Delta C_{y,p})_\Gamma, \tag{3.62}$$

according to [1]. The slope of the side force due to rolling at zero lift,

$$\left(\frac{C_{y,p}}{C_L}\right)_{C_L=0,\,M} = \frac{A+4\cos\Lambda_{c/4}}{AB+4\cos\Lambda_{c/4}}\frac{AB+\cos\Lambda_{c/4}}{A+\cos\Lambda_{c/4}}\left(\frac{C_{y,p}}{C_L}\right)_{L=0,\,M=0}, \tag{3.63}$$

where $\Lambda_{c/4}$ is the quarter-chord sweepback angle, the Mach number parameter

$$B = \sqrt{1-M^2\cos^2\Lambda_{c/4}}\,, \tag{3.64}$$

and $\left(\frac{C_{y,p}}{C_L}\right)_{L=0,\,M=0}$ is the slope of the low-speed side force due to rolling at zero lift, obtained from [1, Fig. 7.1.2.1-9] as a function of the aspect ratio, sweep of the quarter-chord, and taper ratio. Furthermore, C_L is the wing lift coefficient, and $(\Delta C_{y,p})_\Gamma$ is the increment in $C_{y,p}$ due to dihedral effect given by

$$(\Delta C_{y,p})_\Gamma = \left(3\sin\Gamma\left(1-2\frac{z}{b/2}\sin\Gamma\right)\right)(C_{r,p})_{\Gamma=0,\,L=0}\,, \tag{3.65}$$

where Γ is the dihedral angle (positive for the wing tip above the plane of the root chord), z is the vertical distance between the CoG and the wing root quarter-chord point (positive for the CoG above the wing root chord), and $(C_{r,p})_{\Gamma=0,\,L=0}$ is the roll-damping derivative of the wing without dihedral given by

$$(C_{r,p})_{\Gamma=0,\,L=0} = \left(\frac{\beta C_{r,p}}{\kappa}\right)_{L=0}\frac{\kappa}{\beta}, \tag{3.66}$$

where $\left(\frac{\beta C_{r,p}}{\kappa}\right)_{L=0}$ was obtained from [1, Fig. 7.1.2.2-20] as a function of the compressible sweep parameter given by

$$\Lambda_\beta = \tan^{-1}\left(\frac{\tan\Lambda_{c/4}}{\beta}\right), \tag{3.67}$$

and $\beta A/\kappa$, where β is a Mach number parameter defined as

$$\beta = \sqrt{1-M^2}. \tag{3.68}$$

Furthermore, the ratio of the 2D lift-curve slope at appropriate Mach number to $2\pi/\beta$ is given by

$$\kappa = \frac{(c_{l,\alpha})_M}{2\pi/\beta}, \tag{3.69}$$

where $(c_{l,\alpha})_M$ is the airfoil section lift curve slope at the considered Mach number. The factor K in (3.62) is equal to one at zero lift and at lift coefficients other than zero it is given by

$$K = \frac{\frac{\partial}{\partial\alpha}(C_L \tan\alpha) - \frac{\partial}{\partial\alpha}(C_D - C_{D,0})}{\frac{\partial}{\partial\alpha}(C_L \tan\alpha) - \frac{\partial}{\partial\alpha}\left(\frac{C_L^2}{\pi A}\right)}, \tag{3.70}$$

and is used to account for the variation of profile drag with lift coefficient. The contribution to the side force moment coefficient was obtained as

$$(\Delta C_y)_{p,W} = (C_{y,p})_W \frac{pb}{2V_\infty}. \tag{3.71}$$

The vertical tail contribution to the derivative $C_{y,p}$ was then calculated as

$$(\Delta C_y)_{p,VT} = (C_y)_{VT} \frac{2\,\mathrm{TAS}}{b}, \tag{3.72}$$

as suggested in [21]. The side force coefficient is a function of the airplane angle of attack and the local side slip angle at the vertical tail. In the aerodynamic databank model, the side force coefficient is obtained from a lookup table with CFD data for the vertical tail. The local side slip angle at the vertical tail was calculated as (3.28).

3.6.3.2 ESDU

The wing contribution to the derivative $C_{y,p}$ was estimated as

$$(C_{y,p})_W = \frac{C_L}{2}\left(\frac{A + \cos\Lambda_{c/4}}{A + 4\cos\Lambda_{c/4}}\right)\tan\Lambda_{c/4} + \frac{C_L}{2A}, \tag{3.73}$$

according to [52]. The first term in (3.73) is derived from the lifting-line theory. The second term in (3.73) accounts for the effects of tip suction. The entire wing contribution to $C_{y,p}$ was obtained from [52, Fig. 2] as a function of the aspect ratio and the quarter-chord sweep of the wing planform. This model of $C_{y,p}$ is valid for low speeds. A correction factor due to compressibility was obtained from [52, Fig. 5] as a function of the aspect ratio, the quarter-chord sweep, and the Mach number.

The fin contribution to $C_{y,p}$, was estimated as

$$(C_{y,p})_F = -(K_1 + K_2 K_3)\frac{S_F h_F}{S_W b} \left(\frac{(z_F\cos\alpha - l_F\sin\alpha)/b - \partial\sigma_W/\partial(pb/V) - \partial\sigma_\alpha/\partial(pb/V)}{(z_F - z_{r,F})/b}\right), \tag{3.74}$$

according to [53]. The factor K_1 was obtained from [53, Fig. 1a] as a function of the fin aspect ratio and the fin quarter-chord sweep angle. The factor K_2 was obtained from [53, Fig. 1b] as a function of the span of the horizontal tail, the fin height, and the fin quarter-chord sweep angle. The factor K_3 was obtained from [53, Fig. 1c] as a function of the height of the intersection of the horizontal tail with the fin and the height of the fin. Furthermore, S_F is the fin area, h_F is the fin height, z_F is the vertical distance between the longitudinal body axis and the CoP of the fin, measured normal to the longitudinal body axis, l_F is the coordinate of the CoP position of the fin measured parallel to the longitudinal body axis, and $z_{r,F}$ is the height of the fin root chord measured from the longitudinal body axis in direction normal to it. Finally, $\partial\sigma_W/\partial(pb/V)$ is the wing sidewash parameter taken as the constant value 0.18, and $\partial\sigma_\alpha/\partial(pb/V)$ is the sidewash parameter obtained from [53, Fig. 2] as a function of $\frac{z_F-(z_F\cos\alpha-l_F\sin\alpha)}{b}$.

3.6.4 Roll rate derivative $C_{r,p}$

3.6.4.1 Datcom

In accordance with [1], $C_{r,p}$ was estimated as

$$(C_{r,p})_W = \left(\frac{\beta C_{r,p}}{\kappa}\right)_{L=0}\left(\frac{\kappa}{\beta}\right)\frac{(C_{L,\alpha})_{C_L}}{(C_{L,\alpha})_{L=0}}\frac{(C_{r,p})_\Gamma}{(C_{r,p})_{\Gamma=0}} + (\Delta C_{r,p})_{drag}, \tag{3.75}$$

where $(C_{L,\alpha})_{C_L}$ is the slope of the wing lift curve at any lift coefficient below stall, $(C_{L,\alpha})_{L=0}$ is the slope of the wing lift curve at zero lift, $\frac{(C_{r,p})_\Gamma}{(C_{r,p})_{\Gamma=0}}$ is the dihedral effect parameter, and $(\Delta C_{r,p})_{drag}$ is the increment in the roll damping derivative due to drag. The dihedral effect parameter is given by

$$\frac{(C_{r,p})_\Gamma}{(C_{r,p})_{\Gamma=0}} = 1 - 2\frac{z}{b/2}\sin\Gamma + 3\left(\frac{z}{b/2}\right)^2\sin^2\Gamma. \tag{3.76}$$

The increment in the roll-damping derivative due to drag is given by

$$(\Delta C_{r,p})_{drag} = \frac{(C_{r,p})_{C_{D,L}}}{C_L^2}C_L^2 - \frac{1}{8}C_{D,0}, \tag{3.77}$$

where $\frac{(C_{r,p})_{C_{D,L}}}{C_L^2}$ is the drag-due-to-lift roll-damping parameter obtained from [1, Fig. 7.1.2.2-24] as a function of A and $\Lambda_{c/4}$. The contribution to the rolling moment coefficient was then calculated as

$$(\Delta C_r)_{p,W} = (C_{r,p})_W\frac{pb}{2V_\infty}. \tag{3.78}$$

The vertical tail contribution to the derivative $C_{r,p}$ was calculated as

$$(\Delta C_r)_{p,VT} = (C_r)_{VT}\frac{2\,\mathrm{TAS}}{b}, \tag{3.79}$$

as suggested in [21]. The rolling moment coefficient is a function of the airplane angle of attack and the local side slip angle at the vertical tail. In the aerodynamic databank, the rolling moment coefficient is obtained from a lookup table with CFD data for the vertical tail. The local side slip angle at the vertical tail was calculated as (3.28).

3.6.4.2 ESDU

The wing contribution to the derivative $C_{r,p}$ was obtained from [54, Fig. 1] as a function of the taper ratio, the Mach number parameter $\beta = \sqrt{1-M^2}$, the aspect ratio, the 2D lift curve slope of the wing section at Mach number, and the sweepback of the quarter-chord line.

The fin contribution to $C_{r,p}$ was obtained from [53] as

$$(C_{r,p})_F = (C_{y,p})_F \frac{(z_F \cos\alpha - l_F \sin\alpha)}{b}. \tag{3.80}$$

3.6.5 Rolling derivative $C_{n,p}$

3.6.5.1 Datcom

In [1], the model for $C_{n,p}$ is

$$(C_{n,p})_W = -C_{r,p}\tan\alpha - K\left(-C_{r,p}\tan\alpha - \left(\frac{C_{n,p}}{C_L}\right)_{C_L=0,\,M} C_L\right) + \left(\frac{\Delta C_{n,p}}{\theta}\right)\theta + \left(\frac{\Delta C_{n,p}}{\left(\frac{\partial\alpha}{\partial\delta}\right)_f \delta_f}\right)\left(\frac{\partial\alpha}{\partial\delta}\right)_f \delta_f, \tag{3.81}$$

where $C_{r,p}$ is the roll damping derivative at the considered Mach number, and K is a dimensionless correction factor used to extrapolate the potential flow values to high lift coefficients given by (3.70). Furthermore, $\left(\frac{C_{n,p}}{C_L}\right)_{C_L=0,\,M}$ is the slope of the yawing moment due to rolling at zero lift given by

$$\left(\frac{C_{n,p}}{C_L}\right)_{C_L=0,\,M} = \left(\frac{A+4\cos\Lambda_{c/4}}{AB+4\cos\Lambda_{c/4}}\right)\left(\frac{AB+\frac{1}{2}\left(AB+\cos\Lambda_{c/4}\right)\tan^2\Lambda_{c/4}}{A+\frac{1}{2}\left(A+\cos\Lambda_{c/4}\right)\tan^2\Lambda_{c/4}}\right)\left(\frac{C_{n,p}}{C_L}\right)_{L=0,\,M=0}, \tag{3.82}$$

where $\left(\frac{C_{n,p}}{C_L}\right)_{L=0,\,M=0}$ is the slope of the low-speed yawing moment due to rolling at zero lift given by

$$\left(\frac{C_{n,p}}{C_L}\right)_{L=0,\,M=0} = -\frac{1}{6}\frac{A+6\left(A+\cos\Lambda_{c/4}\right)\left(\frac{\overline{x}}{\overline{c}}\frac{\tan\Lambda_{c/4}}{A}+\frac{\tan^2\Lambda_{c/4}}{12}\right)}{A+4\cos\Lambda_{c/4}}, \tag{3.83}$$

where $\overline{x}$ is the distance from the CoG to the AC (positive for AC aft of the CoG). Furthermore, in (3.81), C_L is the wing lift coefficient, $\frac{\Delta C_{n,p}}{\theta}$ is the effect of linear

wing twist obtained from [1, Fig. 7.1.2.3-12] as a function of the aspect ratio and the taper ratio, θ is the wing twist between the root and tip in degrees (negative for washout), $\frac{\Delta C_{n,p}}{\left(\frac{\partial\alpha}{\partial\delta}\right)_f \delta_f}$ is the effect of symmetric flap deflection obtained from [1, Fig. 7.1.2.3-13] as a function of the aspect ratio, taper ratio, and the ratio of the total span of flaps or control surfaces to the wing span, and $\left(\frac{\partial\alpha}{\partial\delta}\right)_f$ is the 2D lift effectiveness parameter. The contribution to the yawing moment coefficient was then calculated as

$$(\Delta C_n)_{p,W} = (C_{n,p})_W \frac{pb}{2V_\infty}. \tag{3.84}$$

The vertical tail contribution to the derivative $C_{n,p}$ was calculated as

$$(\Delta C_n)_{p,VT} = (C_n)_{VT} \frac{2\,\mathrm{TAS}}{b}, \tag{3.85}$$

as suggested in [21]. The yawing moment coefficient is a function of the airplane angle of attack and the local side slip angle at the vertical tail. In the aerodynamic databank model, the yawing moment is obtained from a lookup table with CFD data for the vertical tail. The local side slip angle at the vertical tail was calculated as (3.28).

3.6.5.2 ESDU

In [52], the wing contribution to the stability derivative $C_{n,p}$ is estimated as

$$C_{n,p} = C_L \left(\frac{C_{n,p}}{C_L}\right)_0 + \frac{\Delta C_{n,p}}{dC'_D/d\alpha} \frac{dC'_D}{d\alpha}, \tag{3.86}$$

where λ is the taper ratio, and the viscous lift coefficient

$$C'_D = C_D - \frac{C_L^2}{\pi A}. \tag{3.87}$$

The linear contribution to $C_{n,p}$, that is, the first term in (3.86), was obtained from [52, Fig. 1] as a function of the aspect ratio, the quarter-chord sweep, and the ratio $\frac{x_{AC}}{b}$. The nonlinear contribution is due to the effects of flow separation over the wing at moderate to high lift coefficients and is given in terms of the rate of change of viscous drag coefficient with angle of attack, i.e., $\frac{dC'_D}{d\alpha}$. An estimate of $\frac{\Delta C_{n,p}}{dC'_D/d\alpha}$ was obtained from [52, Fig. 2] as a function of the aspect ratio and the quarter-chord sweep of the wing planform.

A correction factor for the first order effects of compressible flow to (3.86), which is valid for low speeds, was obtained from [52, Fig. 4], as a function of the aspect ratio, the quarter-chord sweep, and the Mach number.

The fin contribution to $C_{n,p}$ was obtained from [53] as

$$(C_{n,p})_F = -(C_{y,p})_F \frac{(l_F \cos\alpha - z_F \sin\alpha)}{b}. \tag{3.88}$$

3.6.6 Pitching derivative $C_{D,q}$

3.6.6.1 Datcom

In [1], $C_{D,q}$ is given by

$$(C_{D,q})_W = (C_{D,q})_0(-\theta) + \frac{\partial C_{D,q}}{\partial \alpha_{WB}}\alpha_{WB} + \frac{\partial C_{D,q}}{\partial(\frac{q\bar{c}}{2V})}(\frac{q\bar{c}}{2V}), \tag{3.89}$$

where $(C_{D,q})_0$ is the contribution due to the loading at zero angle of attack obtained from [1, Fig. 7.1.1.3-3a] as a function of wing aspect ratio, taper ratio, and sweep, $\frac{\partial C_{D,q}}{\partial \alpha_{WB}}$ is the contribution due to angle of attack obtained from [1, Fig. 7.1.1.3-7a-7f] as a function of wing aspect ratio, taper ratio, and sweep, and $\frac{\partial C_{D,q}}{\partial(\frac{q\bar{c}}{2V})}$ is the contribution due to the rate of change of pitch obtained from [1, Fig. 7.1.1.3-12a-12f] as a function of wing aspect ratio, taper ratio, and sweep. The contribution to the drag coefficient was then calculated as

$$(\Delta C_D)_{q,W} = (C_{D,q})_W \frac{q\bar{c}}{2V_\infty}. \tag{3.90}$$

The horizontal tail contribution to the derivative $C_{L,q}$ was calculated as

$$(\Delta C_D)_{q,HT} = (C_D)_{HT} \frac{2\,\mathrm{TAS}}{\bar{c}}, \tag{3.91}$$

as suggested in [21]. The drag coefficient is a function of the airplane angle of attack and the local angle of attack at the horizontal tail. In the aerodynamic databank mode, this drag coefficient is obtained from a lookup table with CFD data for the horizontal tail. The local angle of attack at the horizontal tail was calculated as (3.25).

3.6.6.2 ESDU

No method for estimating $C_{D,q}$ is presented in ESDU since this derivative generally is small and has a negligible effect on the longitudinal stability.

3.6.7 Pitch rate derivative $C_{L,q}$

3.6.7.1 Datcom

The wing pitching derivative $C_{L,q}$ is in [1] approximated as

$$(C_{L,q})_W = \left(\frac{1}{2} + \frac{2(x_{AC} - x_{CoG})}{\bar{c}}\right) C_{L,\alpha}, \tag{3.92}$$

where $x_{AC} - x_{CoG}$ is the longitudinal distance between the AC and the CoG, and $C_{L,\alpha}$ is the wing lift-curve at the considered Mach number. The contribution to the rolling moment coefficient was then obtained as

$$(\Delta C_L)_{q,W} = (C_{L,q})_W \frac{q\bar{c}}{2V_\infty}. \tag{3.93}$$

The horizontal tail contribution to the derivative $C_{L,q}$ was calculated as

$$(\Delta C_L)_{q,\,HT} = (C_L)_{HT} \frac{2\,\mathrm{TAS}}{\overline{c}}, \tag{3.94}$$

as suggested in [21]. The lift coefficient is a function of the airplane angle of attack and the local angle of attack at the horizontal tail. In the aerodynamic databank model, this lift coefficient is obtained from a lookup table with CFD data for the horizontal tail. The local angle of attack at the horizontal tail was calculated as (3.24).

3.6.7.2 ESDU

The wing contribution to $C_{L,\,q}$ is in [55] given by

$$(C_{L,\,q})_W = a_{1,\,W} \left(\frac{1}{4} \left(\frac{x_{AC} - 0.25\overline{c}}{\overline{c}} \right) \right) - a_{1,\,W} \left(\frac{x_0 - 0.25\overline{c}}{\overline{c}} \right), \tag{3.95}$$

where $a_{1,\,W}$ is the lift curve slope of the wing, x_{AC} is the longitudinal distance from the leading edge of the aerodynamic mean chord to the wing AC, and x_0 is the longitudinal distance from the leading edge of the aerodynamic mean chord to the moment reference point (positive aft of leading edge of aerodynamic mean chord). The tail contribution to $C_{L,\,q}$ is in [55] given by

$$(C_{L,q})_{HT} = a_{1,HT} \frac{S_{HT} x_{HT}}{S_W \overline{c}}, \tag{3.96}$$

where $a_{1,\,HT}$ is the lift curve slope of the horizontal tail, S_{HT} is the planform area of the horizontal tail, x_{HT} is the longitudinal distance from the quarter-chord point of the MAC of the horizontal tail measured parallel to the body axis (positive aft of the moment reference point) and S_W is the planform area of the wing.

3.6.8 Pitch rate derivative $C_{m,\,q}$

3.6.8.1 Datcom

For a Mach value of approximately 0.2, $C_{m,\,q}$ is according to [1] approximated as

$$(C_{m,\,q})_{M \approx 0.2} = -0.7 c_{l,\,\alpha} \cos \Lambda_{c/4} \left(\frac{A \left(\frac{1}{2} \left(\frac{x_{AC} - x_{CoG}}{\overline{c}} \right) + 2 \left(\frac{x_{AC} - x_{CoG}}{\overline{c}} \right)^2 \right)}{A + 2 \cos \Lambda_{c/4}} + \frac{1}{24} \left(\frac{A^3 \tan^2 \Lambda_{c/4}}{A + 6 \cos \Lambda_{c/4}} \right) + \frac{1}{8} \right). \tag{3.97}$$

For higher subsonic, $C_{m,q}$ is approximated by applying a compressibility correction factor to (3.97) as follow.

$$(C_{m,q})_{M>0.2} = \left(\frac{\frac{A^3 \tan^3 \Lambda_{c/4}}{AB+6\cos\Lambda_{c/4}} + \frac{3}{B}}{\frac{A^3 \tan^3 \Lambda_{c/4}}{A+6\cos\Lambda_{c/4}} + 3} \right) (C_{m,q})_{Ma\approx 0.2} = (C_{m,q})_W. \tag{3.98}$$

The contribution to the pitching moment coefficient was then obtained as

$$(\Delta C_m)_{q,W} = (C_{m,q})_W \frac{q\bar{c}}{2V_\infty}. \tag{3.99}$$

The horizontal tail contribution to the derivative $C_{m,q}$ was calculated as

$$(\Delta C_m)_{q,HT} = (C_m)_{HT} \frac{2\,\mathrm{TAS}}{\bar{c}}, \tag{3.100}$$

as suggested in [21]. The pitching moment coefficient is a function of the airplane angle of attack and the local angle of attack at the horizontal tail. In the aerodynamic databank, this pitching moment coefficient is obtained from a lookup table with CFD data for the horizontal tail. The local angle of attack at the horizontal tail was calculated as (3.24).

3.6.8.2 ESDU

The wing contribution to the derivative $C_{m,q}$ is in [55] estimated as

$$\begin{aligned}(C_{m,q})_W = -a_{1,W}\left(\frac{1}{4}\left(\frac{x_{AC}-0.25\bar{c}}{\bar{c}}\right)+\left(\frac{x_{AC}-0.25\bar{c}}{\bar{c}}\right)^2\right)\\ -F\left(\frac{a_{1,0}\cos\Lambda_{1/4}}{48B}\left(\frac{\beta A^3\tan^2\Lambda_{1/4}}{AB+6\cos\Lambda_{1/4}}+3\right)\right)+a_{1,W}\left(\frac{1}{4}\left(\frac{x_{AC}-0.25\bar{c}}{\bar{c}}\right)\right)\left(\frac{x_0-0.25\bar{c}}{\bar{c}}\right)\\ -a_{1,W}\left(\frac{x_0-x_{AC}}{\bar{c}}\right)\left(\frac{x_0-0.25\bar{c}}{\bar{c}}\right),\end{aligned} \tag{3.101}$$

where F is an empirical correction factor obtained from [55, Fig. 3] as a function of the Mach number parameter β and the aspect ratio, and $a_{1,0}$ is the spanwise average of the 2D lift curve slope of the wing section normal to the wing quarter-chord line.

According to [55], the horizontal tail contribution to $C_{m,q}$ is estimated as

$$(C_{m,q})_{HT} = -a_{1,HT}\frac{S_{HT}x_{HT}^2}{S_W\bar{c}^2}. \tag{3.102}$$

3.6.9 Yaw rate derivative $C_{y,r}$

3.6.9.1 Datcom

No method for estimating the wing contribution to $C_{y,r}$ at subsonic speeds is available in [1] as it is stated that this contribution is relatively small compared to the

tail contribution. The vertical tail contribution to the derivative $C_{y,r}$ was calculated as

$$(C_{y,r})_{VT} = (C_y)_{VT} \frac{2\,\mathrm{TAS}}{b}, \tag{3.103}$$

as suggested in [21]. The side force coefficient is a function of the airplane angle of attack and the local side slip angle at the vertical tail. In the aerodynamic databank model, this side force coefficient is obtained from a lookup table with CFD data for the vertical tail. The local side slip angle at the vertical tail was calculated as (3.27).

3.6.9.2 ESDU

The vertical tail contribution to the stability derivative $C_{y,r}$ was obtained from [56, Fig. A1] as a function of the yawing moment tail arm, the area of the vertical tail, the wing span, and the wing planform area.

3.6.10 Yaw rate derivative $C_{r,r}$

3.6.10.1 Datcom

According to [1], $C_{r,r}$ is nearly proportional to the lift coefficient until maximum lift occurs. The variation of $C_{r,r}$ with lift coefficient is in [1] given by

$$(C_{r,r})_W = C_L \left(\frac{C_{r,r}}{C_L}\right)_{C_L=0,\,M} + (\Delta C_{r,r})_{C_L} + \left(\frac{\Delta C_{r,r}}{\Gamma}\right)\Gamma + \left(\frac{\Delta C_{r,r}}{\theta}\right)\theta + \left(\frac{\Delta C_{r,r}}{\left(\frac{\partial\alpha}{\partial\delta}\right)_f \delta_f}\right)\left(\frac{\partial\alpha}{\partial\delta}\right)_f \delta_f, \tag{3.104}$$

where

$$\left(\frac{C_{r,r}}{C_L}\right)_{L=0,\,M} = \frac{1 + \frac{A(1-B^2)}{2B(AB+2\cos\Lambda_{c/4})} + \frac{AB+2\cos\Lambda_{c/4}}{AB+4\cos\Lambda_{c/4}}\,\frac{\tan^2\Lambda_{c/4}}{8}}{1 + \frac{A+2\cos\Lambda_{c/4}}{A+4\cos\Lambda_{c/4}}\,\frac{\tan^2\Lambda_{c/4}}{8}} \left(\frac{C_{r,r}}{C_L}\right)_{L=0,\,M=0}, \tag{3.105}$$

where $\left(\frac{C_{r,r}}{C_L}\right)_{L=0,\,M=0}$ is the slope of the low-speed rolling moment due to yawing at zero lift obtained from [1, Fig. 7.1.3.2-10] as a function of aspect ratio, sweep of the quarter-chord, and taper ratio, and $(\Delta C_{r,r})_{C_L}$ is a correction factor used to extrapolate the potential flow values of $C_{r,r}$ to higher lift coefficients which in this study is set to zero. Furthermore, $\frac{\Delta C_{r,r}}{\Gamma}$ is the increment in $C_{r,r}$ due to dihedral given by

$$\frac{\Delta C_{r,r}}{\Gamma} = \frac{1}{12}\,\frac{\pi A \sin\Lambda_{c/4}}{A + 4\cos\Lambda_{c/4}}, \tag{3.106}$$

where $\frac{\Delta C_{r,r}}{\theta}$ is the increment in $C_{r,r}$ due to wing twist obtained from [1, Fig. 7.1.3.2-11] as a function of the aspect ratio, taper ratio, and wing twist, and $\frac{\Delta C_{r,r}}{\left(\frac{\partial\alpha}{\partial\delta}\right)_f \delta_f}$ is the

effect of flap deflection obtained from [1, Fig. 7.1.3.2-12] as a function of the aspect ratio, taper ratio, and location of inboard and outboard flaps in percent of semispan. The contribution to the yawing moment coefficient was then obtained as

$$(\Delta C_r)_{r,W} = (C_{r,r})_W \frac{rb}{2V_\infty}. \tag{3.107}$$

The vertical tail contribution to the derivative $C_{r,r}$ was calculated as

$$(\Delta C_r)_{r,VT} = (C_r)_{VT} \frac{2\,\mathrm{TAS}}{b}, \tag{3.108}$$

as suggested in [21]. The yawing moment coefficient is a function of the airplane angle of attack and the local side slip angle at the vertical tail. In the aerodynamic databank model, this yawing moment coefficient is obtained from a lookup table with CFD data for the vertical tail. The local side slip angle at the vertical tail was calculated as (3.27).

3.6.10.2 ESDU

The wing contribution to the stability derivative $C_{r,r}$ was obtained from [57] as

$$(C_{r,r})_W = (C_{r,r})_p + (C_{r,r})_\Gamma + (C_{r,r})_\theta + (C_{r,r})_f, \tag{3.109}$$

where the terms are contributions due to the planform (p), dihedral (Γ), twist (θ), and deflected trailing edge flaps (f). The planform contribution was obtained from [57, Fig. 1a] as a function of the aspect ratio, the taper ratio, the lift coefficient, and the sweepback function obtained from [57, Fig. 1b] as a function of the sweepback of the quarter-chord. The dihedral contribution to $C_{r,r}$ was obtained from [57, Fig. 3] as a function of the sweepback of the quarter-chord line and the dihedral angle. The twist contribution to $C_{r,r}$ was obtained from [57, Fig. 4] as a function of the wing aspect ratio, the taper ratio, and the wing twist. The contribution to $C_{r,r}$ due to deflection of trailing edge flaps was obtained from [57, Fig. 5] as a function of the aspect ratio, the slope of the lift increment curve with flap deflection in 2D flow, the flap deflection, the spanwise distance between the inner ends of the flaps, and the spanwise distance between the outer ends of the flaps.

According to [56], $C_{r,r}$ for the wing and fin was estimated as

$$C_{r,r} = (C_{r,r} - (C_{r,r})_W)_{\alpha=0}(z_F \cos\alpha - l_F \sin\alpha)/z_F, \tag{3.110}$$

where $(C_{r,r} - (C_{r,r})_W)_{\alpha=0}$ was obtained from [56, Fig. A1] as a function of $\frac{l_F z_F S_F}{b^2 S}$.

3.6.11 Yaw rate derivative $C_{n,r}$

3.6.11.1 Datcom

The wing contribution to the yaw damping in the range of lift coefficients for which $C_{n,r}$ varies linearly with C_L consists a contribution from the drag due to lift and a

contribution from the profile drag. In [1], it is given by

$$(C_{n,r})_W = \left(\frac{C_{n,r}}{C_L^2}\right) C_L^2 + \left(\frac{C_{n,r}}{C_{D,0}}\right) C_{D,0}, \tag{3.111}$$

where $\frac{C_{n,r}}{C_L^2}$ is the low-speed drag-due-to-lift yaw damping parameter obtained from [1, Fig. 7.1.3.3-6] as a function of wing aspect ratio, taper ratio, sweepback, and CoG position, $\frac{C_{n,r}}{C_{D,0}}$ is the low-speed profile drag yawing parameter obtained from [1, Fig. 7.1.3.2-7] as a function of the wing aspect ratio, sweep-back, and CoG position, and $C_{D,0}$ is the wing profile drag coefficient given by

$$C_{D,0} = C_D - \frac{C_L^2}{\pi A}. \tag{3.112}$$

The contribution to the yawing moment coefficient was then obtained as

$$(\Delta C_n)_{r,W} = (C_{n,r})_W \frac{rb}{2V_\infty}. \tag{3.113}$$

The vertical tail contribution to the derivative $C_{n,r}$ was calculated as

$$(\Delta C_n)_{r,VT} = (C_n)_{VT} \frac{2\,\mathrm{TAS}}{b}, \tag{3.114}$$

as suggested in [21]. The yawing moment coefficient is a function of the airplane angle of attack and the local side slip angle at the vertical tail. In the aerodynamic databank model, this yawing moment coefficient is obtained from a lookup table with CFD data for the vertical tail. The local side slip angle at the vertical tail was calculated as (3.27).

3.6.11.2 ESDU

The main contribution to the stability derivative $C_{n,r}$ is the vertical tail but also the wing and body gives considerable contributions. The wing contribution to $C_{n,r}$ is in [58] estimated as

$$(C_{n,r})_W = \frac{(C_{n,r})_0}{C_{D,0}} C_{D,0} + \frac{(C_{n,r})_v}{C_L^2} C_L^2, \tag{3.115}$$

where $\frac{(C_{n,r})_0}{C_{D,0}}$ is the contribution due to wing drag at zero lift, obtained from [58, Fig. 1] as a function of the aspect ratio and the taper ratio, and $\frac{(C_{n,r})_v}{C_L^2}$ is the the contribution arising from lift-dependent drag due to trailing vortices, obtained from [58, Fig. 2] as a function of the aspect ratio, taper ratio, and sweepback angle of the quarter-chord line.

The vertical tail contribution to $C_{n,r}$ was obtained from [56, Fig. A1] as a function of $\frac{l_F^2 S_F}{b^2 S}$.

3.7 Ice effect estimation

In this section, the approach to predict the icing effects on the aerodynamics of the considered airplane is described.

The ice effect analysis was limited to an analysis of a 45 minutes holding condition at an altitude of 6000 ft. In accordance with [47], the analysis of the 45 minutes holding included one fast and light flight configuration, and one slow and heavy flight configuration. In the fast and light case, the maximum holding airspeed, minimum operating weight (MOW) and forward CoG, were used to obtain the lowest possible angle of attack. The collection efficiency increases with airplane speed as the chance that the droplets are moving with the air flow along the airfoil decreases with the airplane speed [59]. Furthermore, at a low angle of attack, the ice accretion is greater on the upper surface of the airfoil which is the most critical location of ice accretion in terms of lift and drag penalties. Hence, this configuration may be the most critical.

The speed used in the slow and heavy case is defined as the 1g stall speed times a factor of 1.4, that is, $1.4V_S$, corresponding to the minimum holding speed. The heavy and slow configuration uses the minimum holding speed in combination with maximum takeoff weight (MTOW), and aft CoG. The ice causes the wing to stall at a lower angle of attack or higher air speed compared to a clean wing. It is thus important to evaluate this flight configuration when performing the ice effect analysis.

The 1g stall speed for the heavy case with aft CoG was iteratively determined by trimming the airplane simulation model for climb using a constant thrust of 0.75% of full power for different values of the calibrated air speed. The maximum speed used in the fast and light case was taken as 175 KCAS but varies depending on the specific situation. The aircraft simulation model was then trimmed for level flight at the specific holding speed to obtain the corresponding angle of attack to the different airplane mass properties.

According to [47], a mean effective droplet diameter of 22 μm and a liquid water content of 0.5 g/m^3 with no horizontal extent correction are typically used in the analysis of 45 minutes holding. The values of the atmospheric parameters, including temperature, should represent the critical conditions for the airplane's performance and handling qualities. Critical flight conditions, such as weight and speed for the critical angle of attack, as well as speed and altitude for maximum collection efficiency should be considered, as stated in [47].

In this study, the atmospheric flight conditions were selected in accordance with [47], [60] and the International Standard Atmosphere (ISA) model. The six different atmospheric cases, defined by temperature, LWC value, and MVD value, included in this study are presented in Table 3.2.

Table 3.2: The atmospheric cases

Case	Temperature [°C]	LWC [g/m^3]	MVD [μm]
1	-15	0.3	22
2	-10	0.4	22
3	-5	0.5	22
4	-1	0.6	22
5	-5	0.6	15
6	-5	0.15	40

For a selected holding condition, the lift coefficient as a function of the wing spanwise location was then calculated using AVL. The temperatures were selected according to [60]. The ISA model with a temperature deviation were used to determine the values of the speed of sound, air density, and Reynolds number. The computational cost of the analysis was reduced by performing 2D simulations of ice accretion on the airfoil at a few selected 2D stations along the wing. The 2D angle of attack corresponding to the lift coefficient values obtained from AVL was calculated by using XFOIL. XFOIL is a program developed at MIT for analysis of subsonic isolated airfoils using an inviscid linear-vorticity panel method with a Karman-Tsien compressibility correction [61].

The corresponding ice shapes for the different flight and atmospheric conditions were calculated by using Lewice. Lewice is a software for simulation of ice accretion simulation on aircrafts in flight caused by water droplets from a cloud and is developed by the NASA Glenn Research Center. Because of its versatility, speed, and extensive validation, it is a widely used software in the aerospace industry. The atmospheric condition and the wing span location corresponding to the worst case were identified.

A potential flow field is calculated in Lewice using the Hess-Smith 2D panel method for steady flows [62]. The flow solution is then used to calculate the particle trajectories and the impingement points on the body. The distribution of the droplet impingement on the body serves as an input to the thermodynamic model of the icing, based on the Messinger model [63]. The mass and momentum equations are established for a control volume on the icing surface, with the assumption that all unfrozen water on the surface flows to adjacent control volumes. Furthermore, the Messinger model is steady, hence the icing rate, surface temperature, and runback water flux are constant with a stable growth rate of the ice. By specifying an icing time increment, the ice growth rate at each point on the surface can be interpreted as an ice layer which is added to the body, resulting in the generation of new coordinates. This loop is continued until the desired icing time is reached. Once the ice shape is determined, it can be imported to a CFD software where the aerodynamic coefficients for the icing condition under consideration can be computed.[64]

The input data required by Lewice are the airfoil geometry, the flight configuration, and the atmospheric configuration, including the parameters in Table 3.3.[65]

Table 3.3: The input data to Lewice

Parameter	Unit
Airfoil geometry (x and y coordinates)	
Angle of incidence	°
chord	m
Angle of attack	°
Time	s
True air speed	m/s
Altitude	m
Relative humidity	%
Liquid water content	g/m^3
Mean volume diameter	μm
Static Temperature	°C

To obtain the difference in drag and lift force for the icing scenario, CFD simulations of the airflow around the clean and the iced airfoils were performed. To validate the CFD simulation set-up, the pressure distribution of the clean airfoil for the considered holding speed was compared to the pressure distribution for the case obtained by using XFOIL. The difference in the drag and lift coefficients due to the icing was compared to experimental data from the NASA Glenn Research Center's Icing Research Tunnel [42].

A conservative approach was applied by using the differences in drag and lift for the flight condition generating the most critical icing shape as the difference in drag and lift for the entire wing. These differences in the drag and lift coefficient for the considered holding conditions was finally implemented in the aerodynamic databank. Since there is no weather model implemented in the aerodynamic databank, the ice effect will be analyzed by selecting one of the specified holding conditions when initializing the model.

3.7.1 CFD of the flow over the iced airfoil

The coordinates of the clean airfoil and ice shapes obtained in Lewice were imported to STAR-CCM+ as closed three-dimensional (3D) polyline curves. The 3D sketch was extruded with default settings. Additionally, a domain extending approximately 25 chord lengths out from the airfoil in all directions was created. The domain was extruded 5 m and with the body interaction set to none. The left surface of the domain body was assigned as inlet and the right surface of the domain was assigned as outlet. The angle of attack of the airfoil was set by using the rotation transformation feature, selected as a design parameter. Two new geometry parts were created by selecting the domain and airfoil bodies using default settings. The airfoil was then subtracted from the domain by selecting the domain and airfoil as input parts and the domain as the target part. The subtracted part was then assigned to regions using the option to create a boundary for each part surface.

Next, a new physics continuum was added. The selected models for the continuum were

- Two-dimensional
- Steady
- Gas
- Ideal Gas
- Gradients
- Coupled Flow
- Coupled Energy
- Solution Interpolation
- All y+ Wall Treatment
- Wall Distance
- Standard Spalart-Allmaras
- Spalart-Allmaras Turbulence
- Reynolds-Averaged Navier-Stokes
- Turbulent

The reference pressure was set to atmospheric pressure at the considered altitude. The initial velocity in the physics model was set to the considered holding speed of the airplane. The Spalart–Allmaras (SA) model is a one-equation model which solves a transport equation for the turbulent viscosity. This turbulence model was specifically designed for aerospace applications involving wall-bounded turbulent flows with arbitrary pressure gradients.[66] [67]

In Regions, the boundary of the airfoil was set to wall with a no-slip condition, the thermal condition was set to adiabatic, and the wall surface specification was set to smooth. The blended wall function conditions were the log law offset was set to $E = 9$ and the von Karman constant was set to $\kappa = 0.42$. The inlet and outlet boundaries were set to free stream with the conditions specified in terms of the Mach number, pressure (0 Pa), and ambient temperature. The flow direction was set by components, i.e., $\{x, y\} = \{1, 0\}$. The turbulence condition specification was set to a turbulent viscosity ratio of 10.

A badge for 2D meshing as well as an automated 2D mesh were created for the subtracted part. The mesh settings are presented in Table 3.4.

Table 3.4: The STAR-CCM+ automated mesh (2D) settings

Feature	Value
Mesher	Polygonal mesher
Optional Volume Mesher	Prism Layer Mesher
Base size	0.01 m
Target surface size	100% of base
Minimum surface size	10% of base
Surface growth rate	1.1
Number of prism layers	120
Prism layer stretching	1.05
Prism layer total thickness	600% of base

In Custom Controls, a surface control was used to constrain the element size close to the inlet and outlet of the domain. The target surface size and the minimum surface size were both set to 3 m. Another surface control was used to refine the wake behind the airfoil, using the wake refinement feature. The distance was set to 4 m, the isotropic size was set to 100% of base, and the growth rate was set to 1.1. The mesh around the leading edge was refined using a cylindrical shaped volumetric control with settings adapted to the specific airfoil configuration.

In the report branch, force coefficient reports were created for the drag and lift coefficient of the airfoil. The settings in these reports were either x or y as direction, pressure and shear as force option, 0 Pa as reference pressure, the density at the considered altitude as the reference density, the considered holding speed as the reference velocity, and 1 m^2 as reference area. The reference area was based on the chord length in the lift coefficient calculation as well as in the drag coefficient calculation, since the drag force is mainly due to skin friction.

4

Results

In this chapter, numerical results of this study are presented. The level of comprehensiveness of the aerodynamic databank makes it inconvenient to include all numerical results, hence only representative numerical results, and the numerical results of greatest importance are included in this report. Due to confidentiality reasons, some of the numerical values are removed from the graphs.

4.1 Drag coefficient corrections

The drag polar for respective flap deflection are seen in Figure 4.1. The original CFD data were corrected using performance data to account for the additional drag due to viscous effects which was not resolved in the CFD simulations. The numerical values of the lift and drag coefficients are removed due to confidentiality reasons.

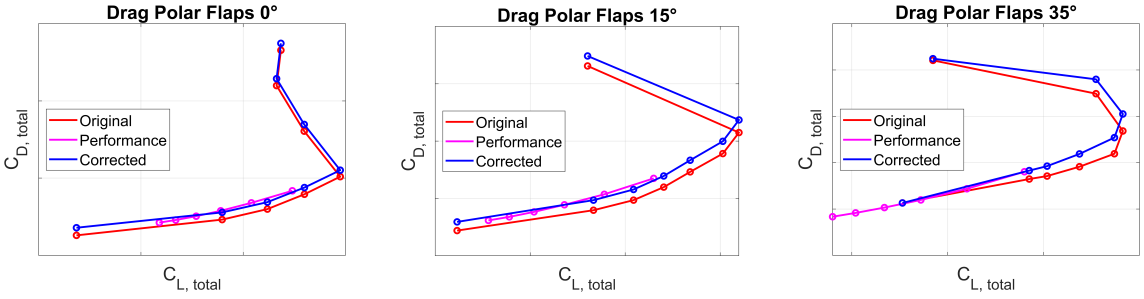

(a) 0° flap deflection **(b)** 15° flap deflection **(c)** 35° flap deflection

Figure 4.1: The drag polar for respective flap deflection

The extrapolated and corrected drag coefficients for respective component as well as the total drag compared to the original CFD data are viewed in Figure 4.2. The numerical values of the drag coefficients are removed due to confidentiality reasons.

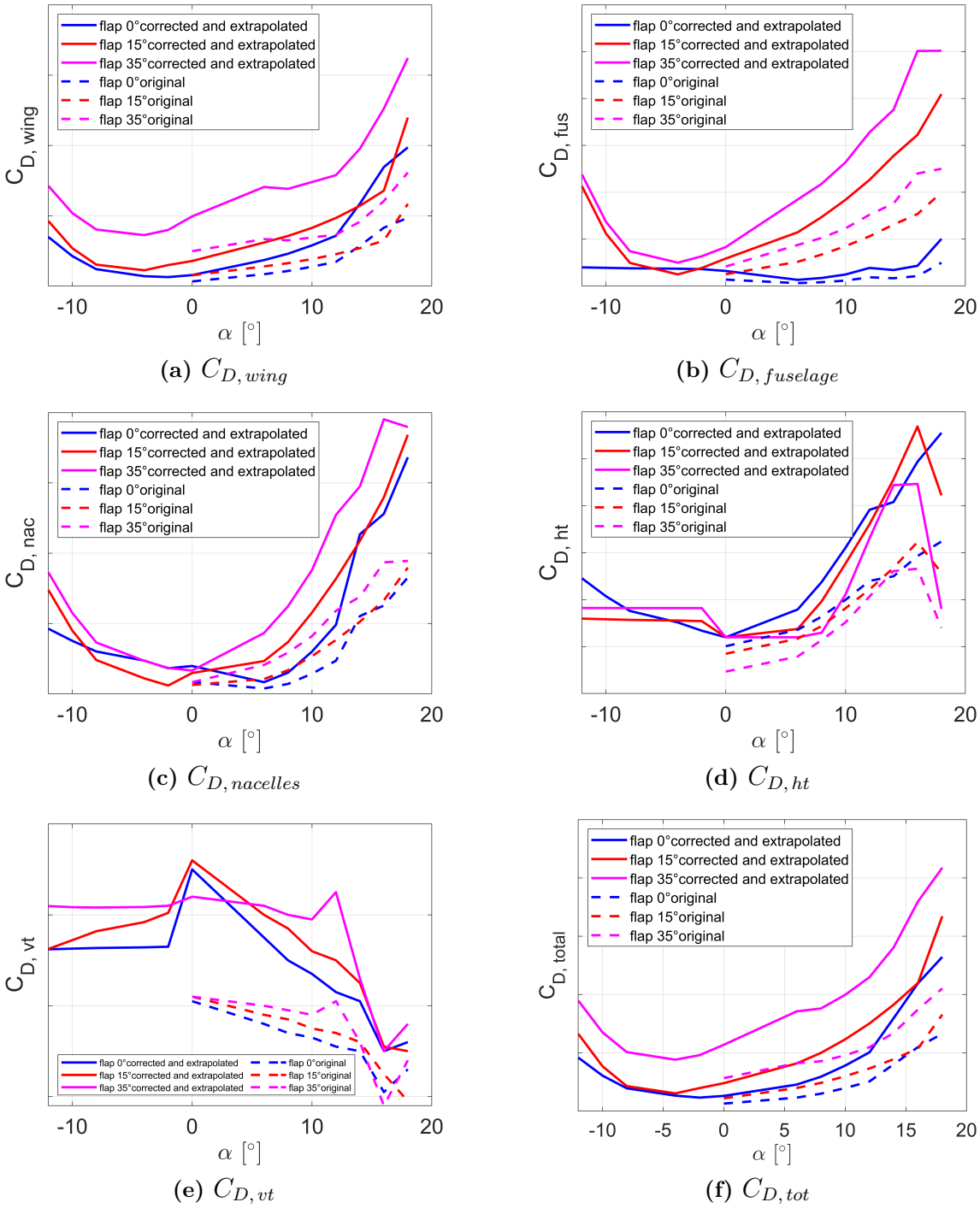

(a) $C_{D,\,wing}$ **(b)** $C_{D,\,fuselage}$

(c) $C_{D,\,nacelles}$ **(d)** $C_{D,\,ht}$

(e) $C_{D,\,vt}$ **(f)** $C_{D,\,tot}$

Figure 4.2: The extrapolated and corrected drag coefficients

4.2 The baseline aerodynamic coefficients

The baseline aerodynamic coefficients are retrieved from CFD-RANS simulations of a sweep of the angle of attack for the different flap deflections. The output from the aerodynamic databank for different flap deflections is seen in Figure 4.3. Since the side slip angle is zero, the side force, rolling moment, and yawing moment coefficients are approximately zero for any angle of attack. The Mach number was set to 0.3 and the mass properties case was heavy aft CoG, see Figure 3.1. The numerical values of the coefficients are removed due to confidentiality reasons.

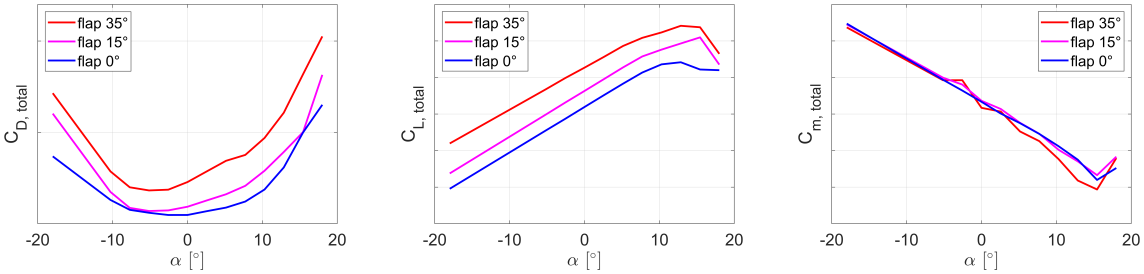

(a) $C_{D,tot}$ vs α **(b)** $C_{L,tot}$ vs α **(c)** $C_{m,tot}$ vs α

Figure 4.3: The baseline aerodynamic coefficients as functions of the angle of attack at different flap deflections

4.3 Side slip contribution

The aerodynamic coefficients as functions of the side slip angle are seen in Figure 4.4. The Mach value was set to 0.3 and the mass properties case is heavy aft CoG, see Figure 3.1. The numerical values of the coefficients are removed due to confidentiality reasons.

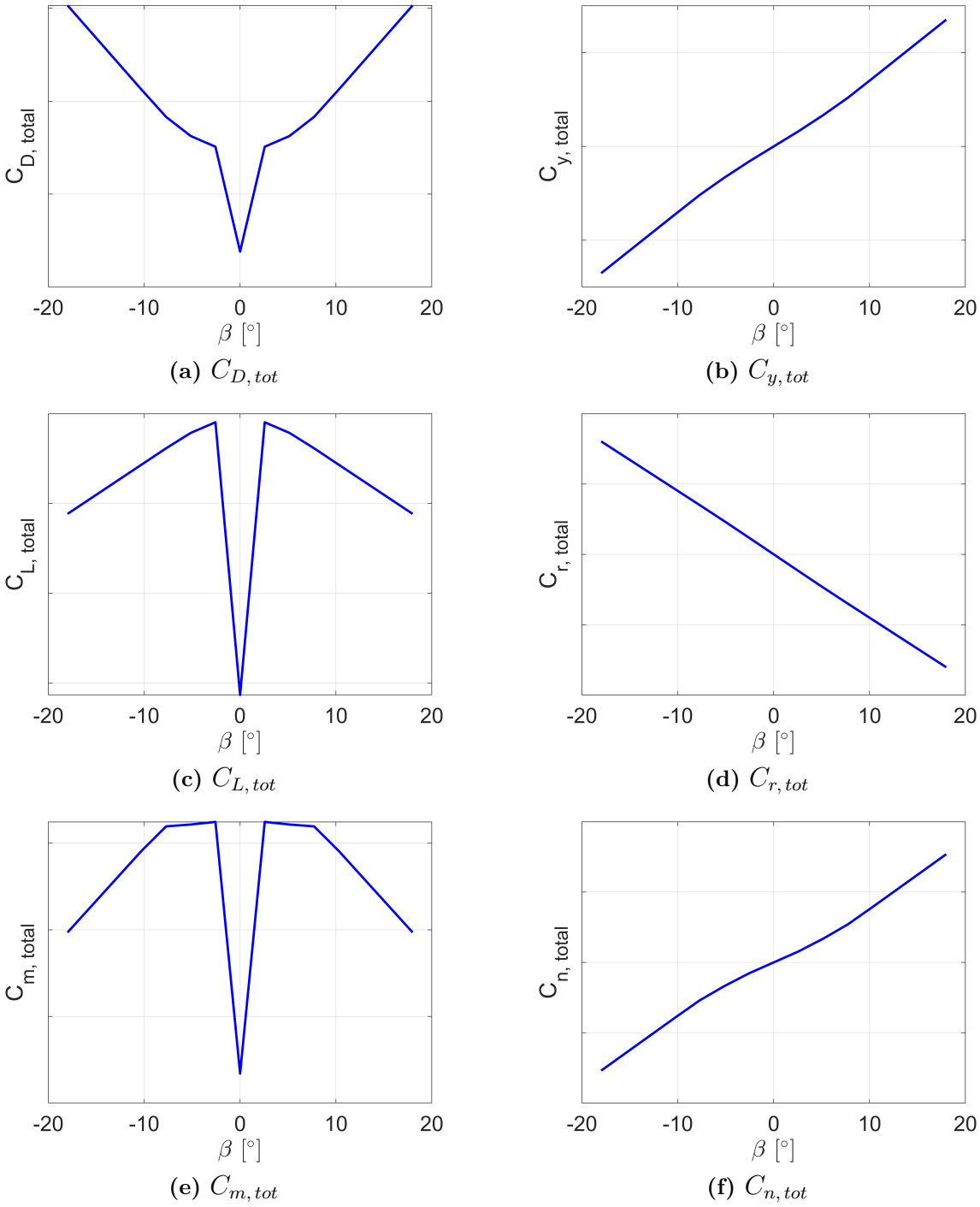

(a) $C_{D,tot}$ **(b)** $C_{y,tot}$

(c) $C_{L,tot}$ **(d)** $C_{r,tot}$

(e) $C_{m,tot}$ **(f)** $C_{n,tot}$

Figure 4.4: The aerodynamic coefficients versus the side slip angle

4.4 Control surface deflections

The Mach number was set to 0.3 and the mass properties case was heavy aft CoG, see Figure 3.1.

4.4.1 Elevator deflection

The effects of elevator deflection on the aerodynamic coefficients versus the side slip angle are seen in Figure 4.5. The elevator deflection does not give any contribution to the side force, rolling moment, and yawing moment coefficients. The numerical values of the coefficients are removed due to confidentiality reasons.

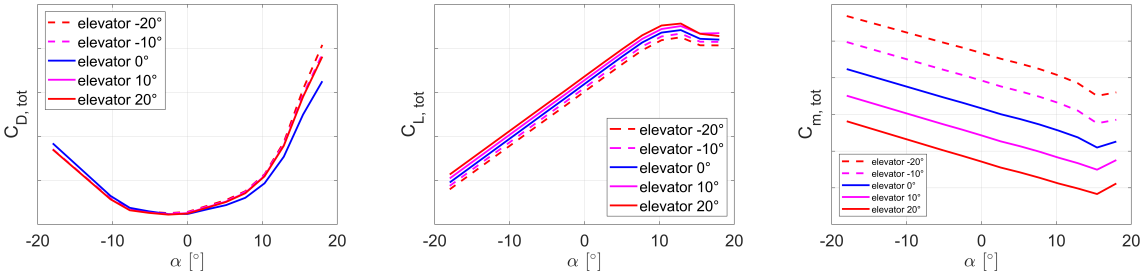

(a) $C_{D,tot}$ vs α **(b)** $C_{L,tot}$ vs α **(c)** $C_{m,tot}$ vs α

Figure 4.5: The effects on the drag, lift, and pitching moment coefficients due to deflection of the elevator

4.4.2 Rudder deflection

The effects of rudder deflection on the aerodynamic coefficients versus the side slip angle are seen in Figure 4.6. The effects on the lift and pitching moment coefficients are negligible. The numerical values of the coefficients are removed due to confidentiality reasons.

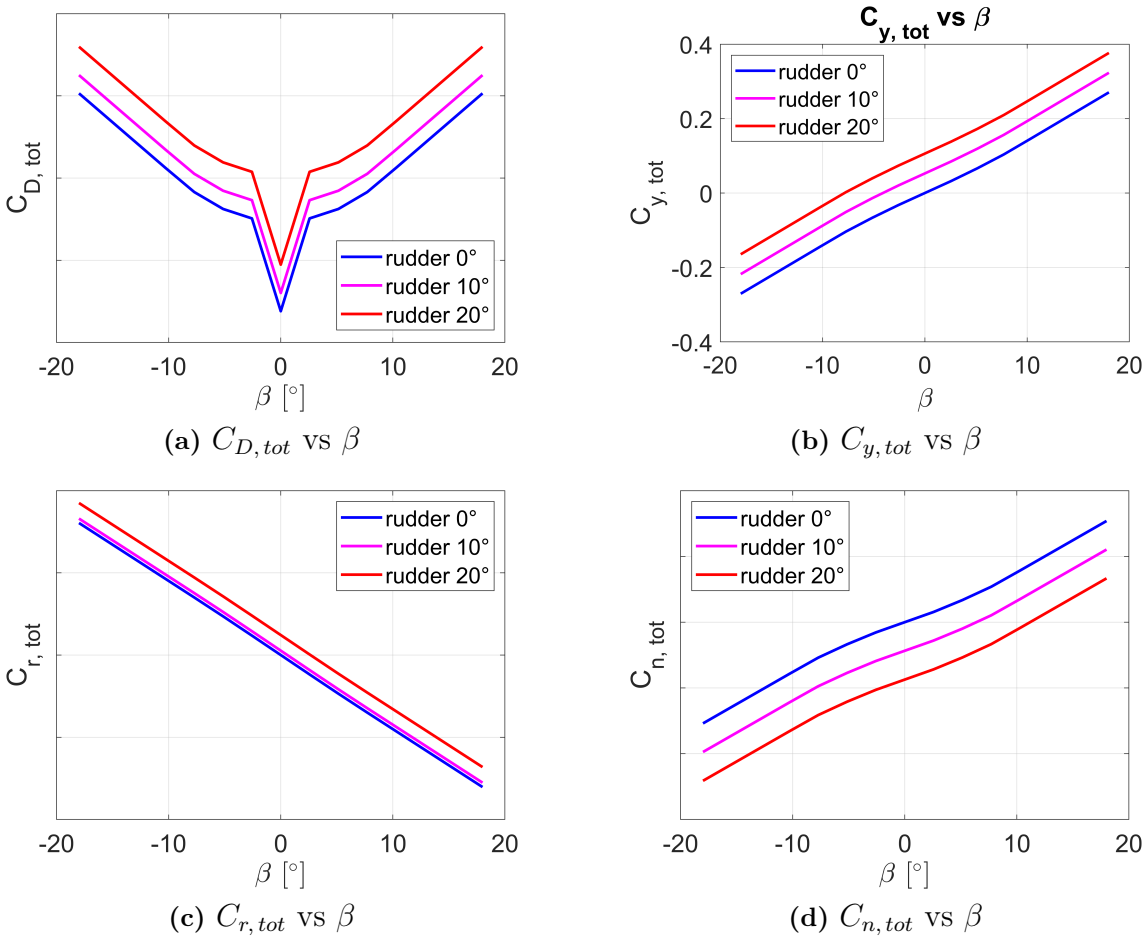

(a) $C_{D,tot}$ vs β

(b) $C_{y,tot}$ vs β

(c) $C_{r,tot}$ vs β

(d) $C_{n,tot}$ vs β

Figure 4.6: The effects of rudder deflections

4.4.3 Aileron deflection

The effect of deflection of the ailerons is seen in Figure 4.7. As mentioned in Section 2.14.1, the ailerons move in the opposite direction to each other in order to create a rolling moment. The effect on the lift, pitching moment, and yawing moment coefficients due to aileron deflection is negligible. The numerical values of the coefficients are removed due to confidentiality reasons.

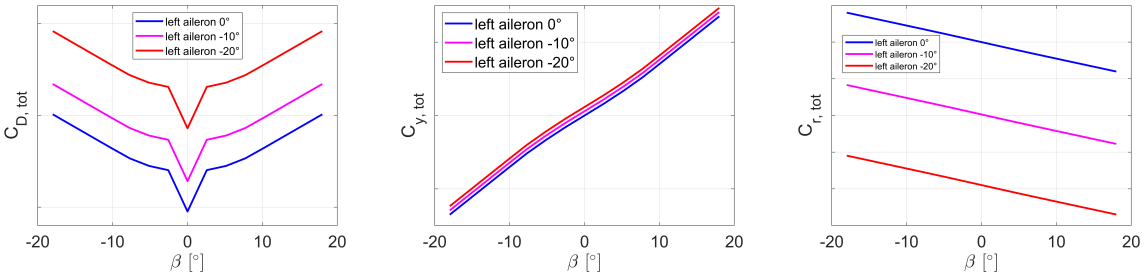

(a) Effect on $C_{D,tot}$ due to ailerons

(b) Effect on $C_{y,tot}$ due to ailerons

(c) Effect on $C_{r,tot}$ due to ailerons

Figure 4.7: The effects on the drag, side force, and rolling moment coefficients due to deflection of the ailerons

4.5 Mach effect

The changes in drag, lift, and pitching moment coefficient due to compressibility are seen in Figure 4.8. The mass properties of the airplane correspond to heavy aft CoG, see Figure 3.1. The numerical values of the coefficients are removed due to confidentiality reasons.

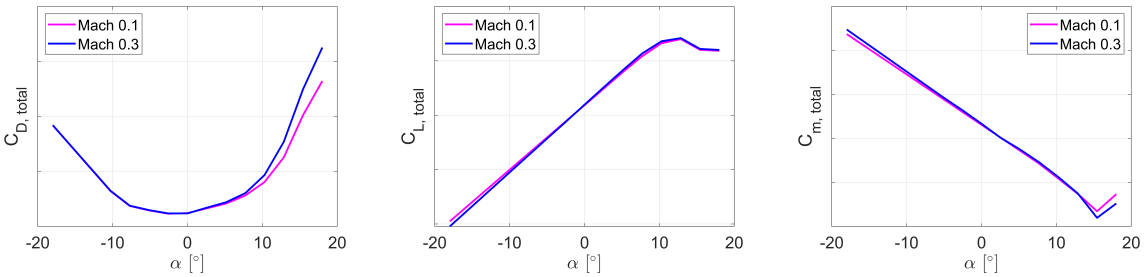

(a) Change in drag coefficient due to compressibility

(b) Change in lift coefficient due to compressibility

(c) Change in pitching moment coefficient due to compressibility

Figure 4.8: The compressibility effect on the drag, lift, and pitching moment coefficients

4.6 Propeller effect

The effect of the propellers on the drag, lift, and pitching moment coefficient, respectively, are seen in Figure 4.9. The power coefficient was set to 0.5 for all four propellers. The Mach number was set to 0.2 and the mass properties correspond to heavy aft CoG, see Figure 3.1. The numerical values of the coefficients are removed due to confidentiality reasons.

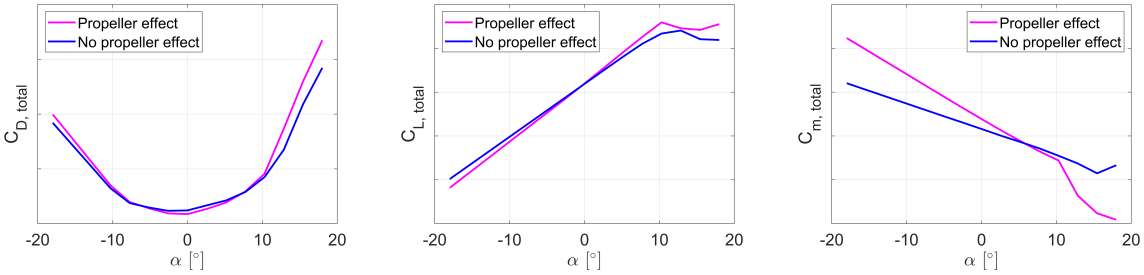

(a) $C_{D,tot}$ vs α **(b)** $C_{L,tot}$ vs α **(c)** $C_{m,tot}$ vs α

Figure 4.9

4.7 Aerodynamic effect of landing gear deployment

The effect on the drag coefficient and the pitching moment coefficient, respectively, due to deployment of the landing gear are seen in Figure 4.10. The Mach number was set to 0.1 and the mass properties case is heavy aft CoG, see Figure 3.1. The numerical values of the coefficients are removed due to confidentiality reasons.

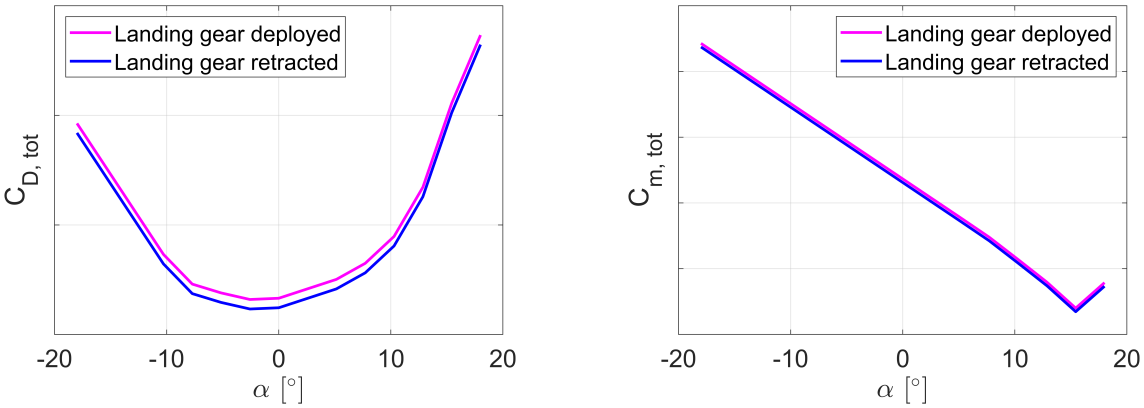

(a) The total drag coefficient

(b) The total pitching moment coefficient

Figure 4.10: The effect on the total drag and pitching moment coefficient, respectively, due to landing gear deployment

4.8 Ground effect

The ground effect on the total drag coefficient at 1 m and 5 m above ground, respectively, is seen in Figure 4.11. The Mach number was set to 0.1 and the mass properties of the airplane were set to heavy aft CoG, see Figure 3.1. The numerical values of the coefficients are removed due to confidentiality reasons. The results are obtained for zero flap deflection.

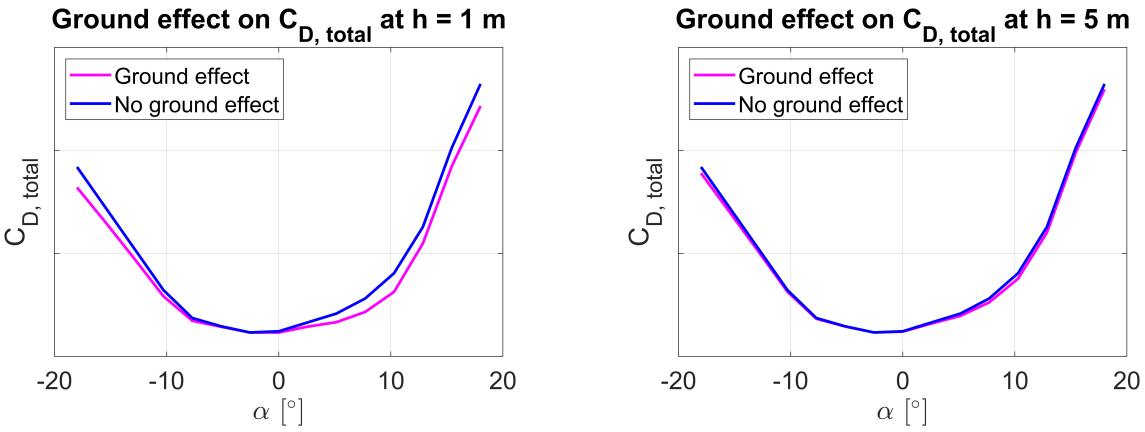

(a) The total drag coefficient at 1 m above ground

(b) The total drag coefficient at 5 m above ground

Figure 4.11: The ground effect on the total drag coefficient

The ground effect on the total lift coefficient at 1 m and 5 m above ground, respectively, is seen in Figure 4.12. The numerical values of the coefficients are removed due to confidentiality reasons. The results are obtained for zero flap deflection.

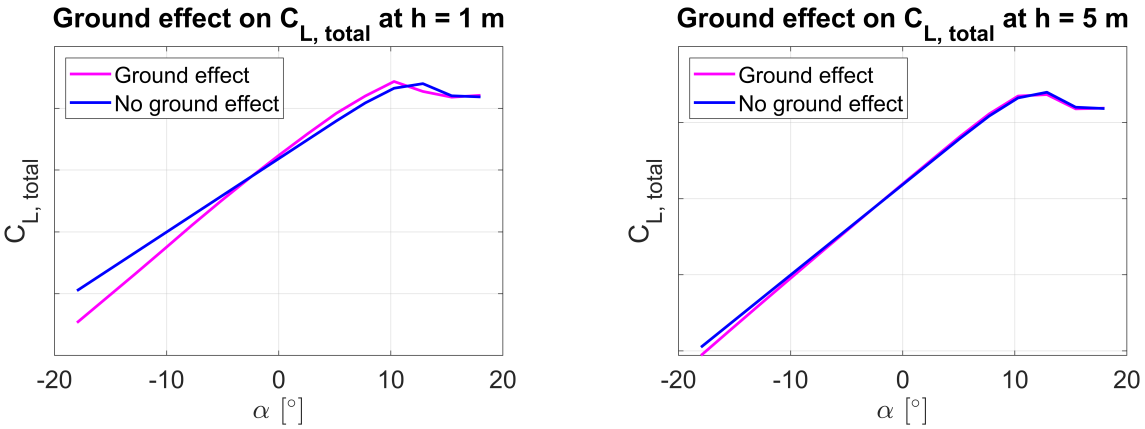

(a) The total lift coefficient at 1 m above ground

(b) The total lift coefficient at 5 m above ground

Figure 4.12: The ground effect on the total lift coefficient

The ground effect on the total pitching moment coefficient at 1 m and 5 m above ground, respectively, is seen in Figure 4.13. The numerical values of the coefficients

are removed due to confidentiality reasons. The results are obtained for zero flap deflection.

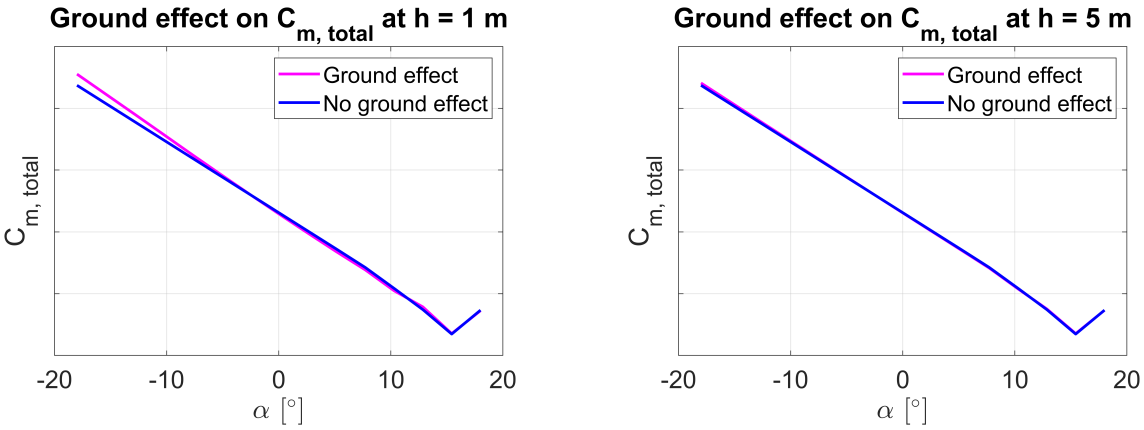

(a) The total pitching moment coefficient at 1 m above ground

(b) The total pitching moment coefficient at 5 m above ground

Figure 4.13: The ground effect on the total pitching moment coefficient

4.9 Stability derivatives

The stability derivatives obtained based on the DATCOM methods [1], the method for the tail contributions found in [21], the ESDU methods, and AVL are presented in this section. All the results of the modeled stability derivatives are based on contributions from the wings and the horizontal or vertical tail, depending on the specific derivative. The ESDU methods for the wing contribution are combined with both the ESDU methods for the tail contribution as well as the method for the tail contributions found in [21]. The Mach number was set to 0.3 and the mass properties case is heavy aft CoG, see Figure 3.1.

The rolling moment derivatives $C_{y,p}$, $C_{r,p}$, and $C_{n,p}$ as a function of the angle of attack for maximum takeoff weight with the CoG at the aft limit are presented in Figure 4.14. The curve denoted ESDU (i) represents a wing contribution obtained from ESDU while the tail contribution was calculated based on the induced side slip angle at the vertical tail defined as (3.28). The curve denoted ESDU (ii) is based on the ESDU equations for the wing and the tail.

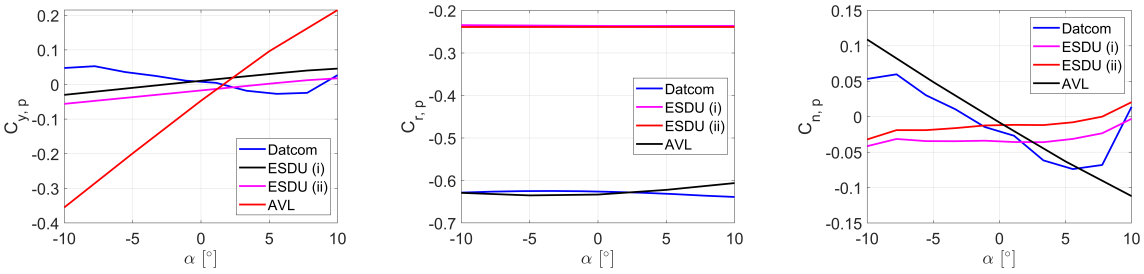

(a) $C_{y,p}$ **(b)** $C_{r,p}$ **(c)** $C_{n,p}$

Figure 4.14: The rolling moment derivatives

The pitching moment derivatives $C_{D,q}$, $C_{L,q}$, and $C_{m,q}$ as a function of the angle of attack for maximum takeoff weight with the CoG at the aft limit are presented in Figure 4.15. The curve denoted ESDU (i) represents a wing contribution obtained from ESDU while the tail contribution was calculated based on the induced angle of attack at the horizontal tail defined as (3.25). The curve denoted ESDU (ii) is based on the ESDU equations for the wing and the tail. The derivative $C_{D,q}$ was only estimated by using the method in [1] for the wing contribution combined with the tail contribution calculated based on the induced angle of attack. No method for estimating $C_{D,q}$ is presented in ESDU, and due to the limitations of the VLM, as described in Section 2.9.1, no estimate of $C_{D,q}$ is provided by AVL.

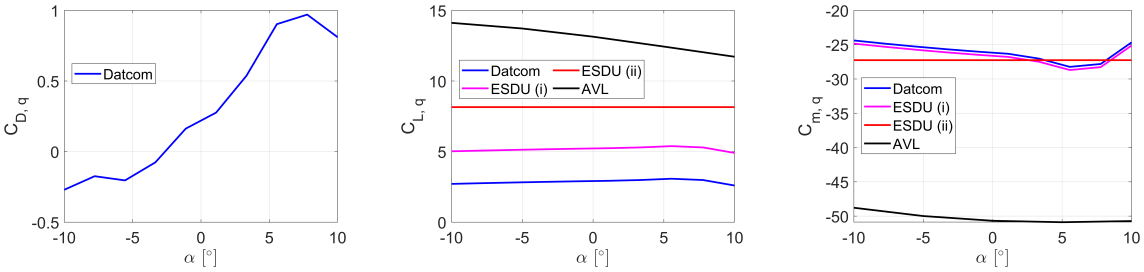

(a) $C_{D,q}$ **(b)** $C_{L,q}$ **(c)** $C_{m,q}$

Figure 4.15: The pitching moment derivatives

The yawing moment derivatives $C_{y,r}$, $C_{r,r}$, and $C_{n,r}$ as a function of the angle of attack for maximum takeoff weight with the CoG at the aft limit are presented in Figure 4.16. The curve denoted ESDU (i) represents a wing contribution obtained from ESDU while the tail contribution was calculated based on the induced side slip angle at the vertical tail defined as (3.29). The curve denoted ESDU (ii) is based on the ESDU equations for the wing and the tail.

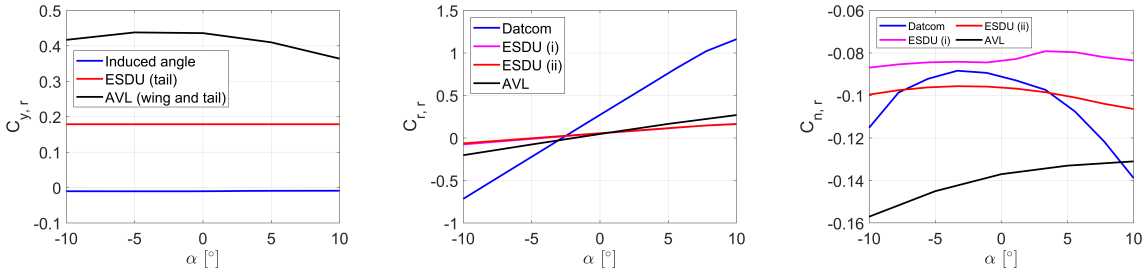

(a) $C_{y,r}$ **(b)** $C_{r,r}$ **(c)** $C_{n,r}$

Figure 4.16: The yawing moment derivatives

4.9.1 Rate of angle of attack derivatives

The rate of angle of attack derivatives based on the contribution from the horizontal tail only, calculated as described in Section 3.6.2, are seen in Figure 4.17.

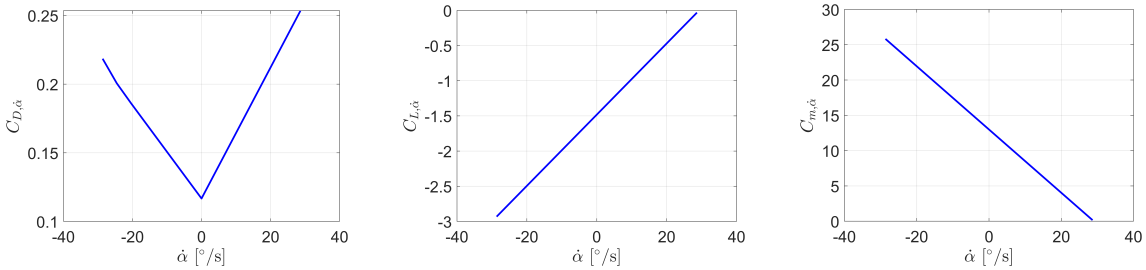

(a) $C_{D,\dot{\alpha}}$ vs $\dot{\alpha}$ **(b)** $C_{L,\dot{\alpha}}$ vs $\dot{\alpha}$ **(c)** $C_{m,\dot{\alpha}}$ vs $\dot{\alpha}$

Figure 4.17: The rate of angle of attack derivatives

4.9.2 Rate of side slip angle derivatives

The rate of side slip angle derivatives based on the contribution from the horizontal tail only, calculated as described in Section 3.6.1, are seen in Figure 4.18.

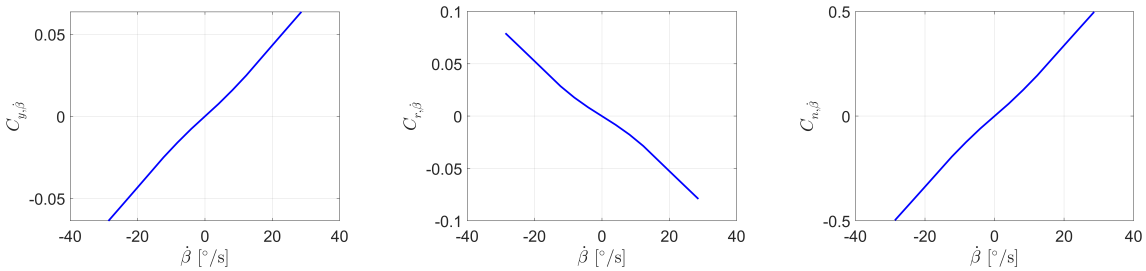

(a) $C_{y,\dot{\beta}}$ vs $\dot{\beta}$ **(b)** $C_{r,\dot{\beta}}$ vs $\dot{\beta}$ **(c)** $C_{n,\dot{\beta}}$ vs $\dot{\beta}$

Figure 4.18: The rate of side slip angle derivatives

4.10 Ice effect on the drag and lift coefficients

The value of the minimum holding speed, used in the slow and heavy holding scenario, was determined to be 142.8 KCAS by using the method described in Section 3.7. The maximum holding speed was set to 175 KCAS, as mentioned in Section 3.7. In conclusion, these holding flight cases were assumed to represent the two worst cases and are presented in Table 4.1.

Table 4.1: The two holding scenarios

Quantity	Slow and heavy	Fast and light
KCAS	142.8	175.0
Mass	MTOW	MOW
CoG	aft	fwd

The corresponding airplane angle of attack for the slow and heavy case was 4.7606°, and for the fast and light case it was 1.4541°. The corresponding 2D angles of attack and 2D lift coefficients $c_l(y)$ at the selected spanwise stations determined by using AVL are presented in Tables 4.2 and 4.3. As AVL does not give reliable results close to the wing tips, the station along the wing furthest out from the root was set to about $0.75b/2$. The most extreme angle of attack values was selected, corresponding to 5.0611° (Station b) in the slow and heavy case, and 1.2790° (Station f) in the fast and light case. These 2D angle of attack values were used in the CFD simulations of the two holding cases.

Table 4.2: The selected stations along the wing and the corresponding 2D lift coefficient and 2D angle of attack, slow and heavy configuration

Station	Chord [m]	$c_l(y)$	2D α [°]
a	2.1490	0.7598	5.0154
b	2.0730	0.7654	5.0611
c	1.9694	0.7488	4.9258
d	1.8658	0.7113	4.6201
e	1.7622	0.6635	4.2307
f	1.6566	0.6064	3.7659

Table 4.3: The selected stations along the wing and the corresponding 2D lift coefficient and 2D angle of attack, fast and light configuration

Station	Chord [m]	$c_l(y)$	2D α [°]
a	2.1490	0.4668	2.6309
b	2.0730	0.4666	2.6292
c	1.9694	0.4449	2.4529
d	1.8658	0.4047	2.1264
e	1.7622	0.3531	1.7075
f	1.6566	0.3003	1.2790

The most severe ice shapes obtained from Lewice for the different flight configurations and spanwise stations were identified. The worst atmospheric case for both flight configurations was identified as Case 3 in Table 3.2. Hence, the ambient air temperature used for the CFD simulations was set to -5 °C. The spanwise station related to the most severe ice shape was for both cases identified as Station f.

The other atmospheric values needed for the CFD simulations and XFOIL were obtained from the ISA model and are seen in Table 4.4.

Table 4.4: The atmospheric values at 6000 ft and at a temperature of -5 °C

Quantity	Slow and heavy	Fast and light
Density [kg/m^3]	1.055	1.055
Dynamic viscosity [Pa·s]	$1.6912{\cdot}10^{-5}$	$1.6912{\cdot}10^{-5}$
Absolute pressure [Pa]	81205	81205
Mach number	0.2408	0.2949
Reynolds number	$4.9310{\cdot}10^{6}$	$6.0387{\cdot}10^{6}$

4.10.1 CFD results of the slow and heavy 45 minutes holding scenario

The most severe ice shape in the slow and heavy case determined by using Lewice is seen in Figure 4.19.

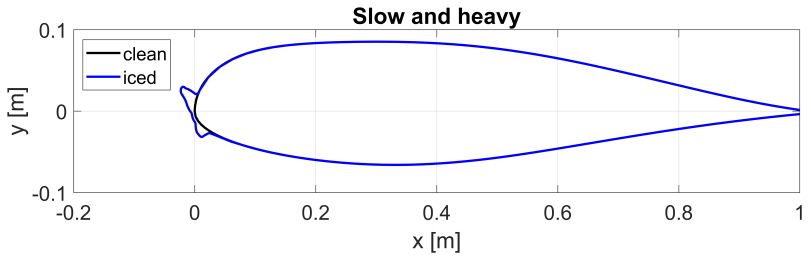

Figure 4.19: The most severe ice shape in the slow and heavy 45 minutes holding case

The velocity vector field around the airfoil for the slow and heavy case obtained from STAR-CCM+ is seen in Figure 4.20.

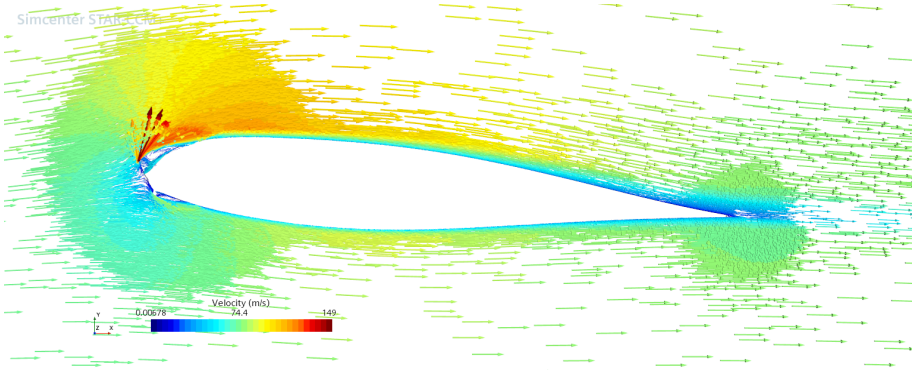

(a) Velocity vector field over the iced airfoil

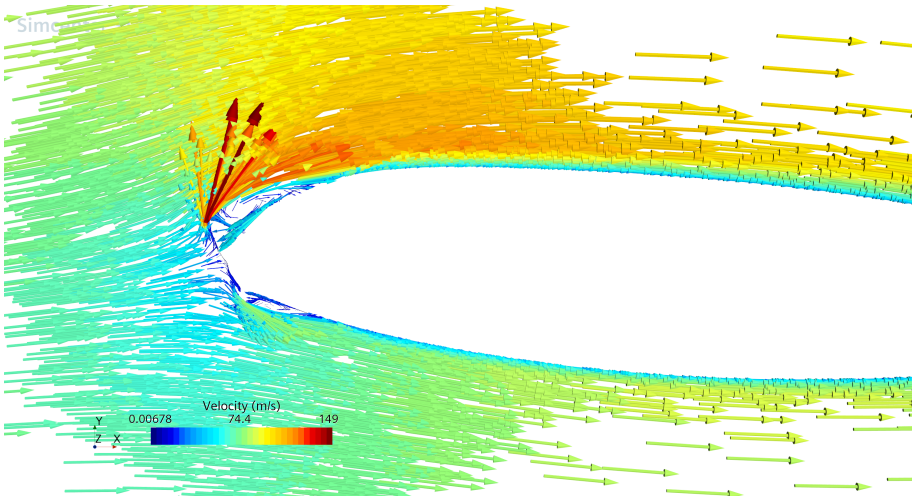

(b) Zoomed view of the leading edge of the velocity vector field over the iced airfoil

Figure 4.20: The velocity vector field around the airfoil in the slow and heavy 45 minutes holding case

The pressure distributions around the clean and iced airfoil in the fast and light case, obtained from STAR-CCM+ and XFOIL, are viewed in Figure 4.21.

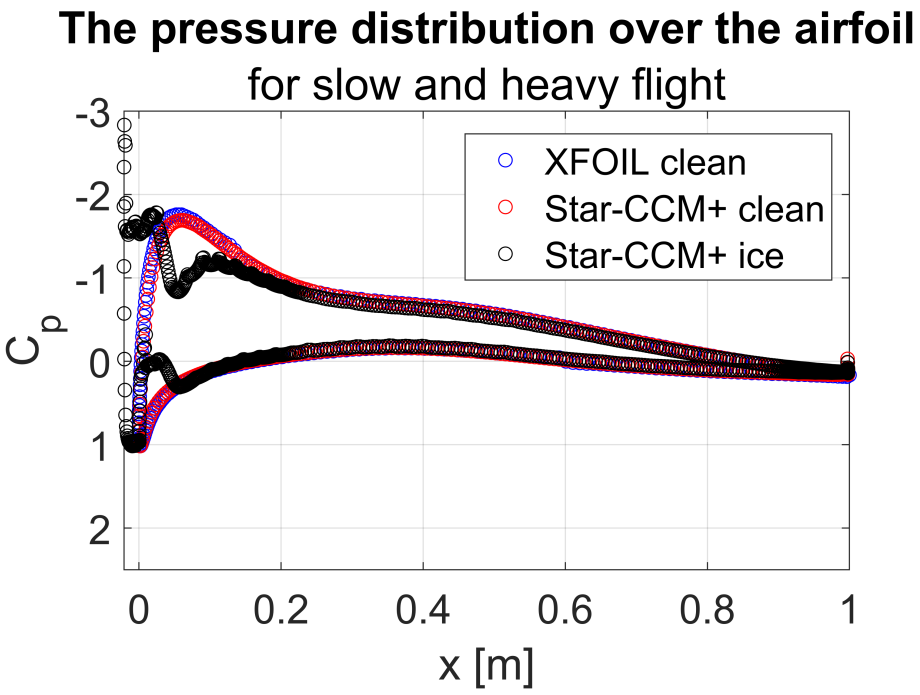

Figure 4.21: The distribution of the pressure coefficient around the airfoil in the slow and heavy case

In Table 4.5, the differences in the drag and lift for the slow and heavy holding scenario are presented.

Table 4.5: The difference in drag and lift coefficient due to icing accretion during 45 minutes holding with a slow and heavy flight condition

Case	c_d	c_l
Slow and heavy clean	0.0109	0.5890
XFOIL clean	0.0073	0.6131
Slow and heavy iced	0.0639	0.5562
Difference [%]	488	-6

In [42], the ice shape in Run 072695.01 for a business jet is comparable to the ice shape obtained in the slow and heavy case in this study. The difference in drag for the Run 072695.01 in [42] is viewed in Table 4.6.

Table 4.6: The difference in drag coefficient due to icing accretion for the business jet studied in [42]

Case	c_d
Clean	0.0093
Iced	0.0258
Difference [%]	177

4.10.2 CFD results of the fast and light 45 minutes holding scenario

The most severe ice shape in the slow and heavy case determined by using Lewice is seen in Figure 4.22.

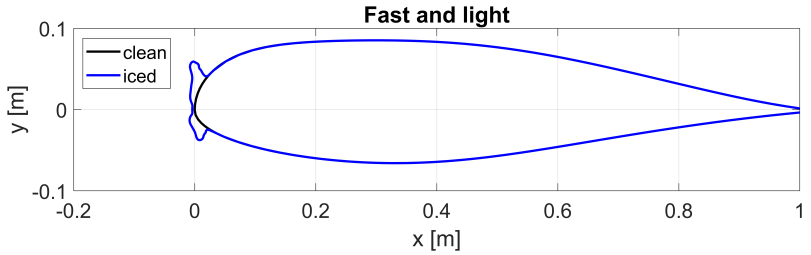

Figure 4.22: The most severe ice shape in the fast and light 45 minutes holding case

The velocity vector field around the airfoil for the fast and light case obtained from STAR-CCM+ is seen in Figure 4.23.

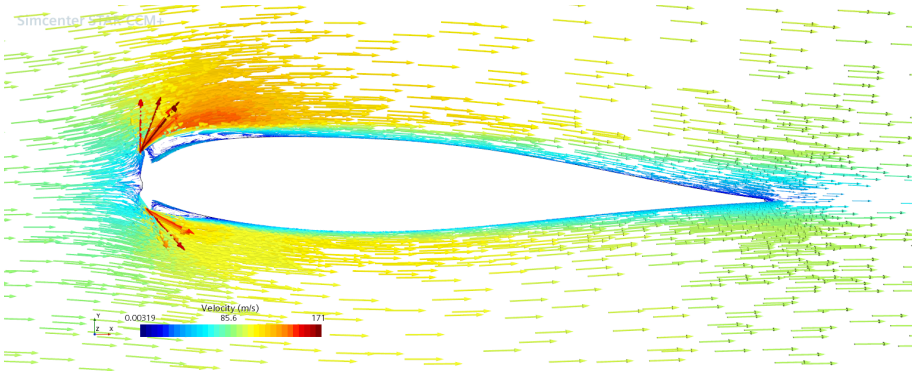

(a) Velocity vector field over the iced airfoil

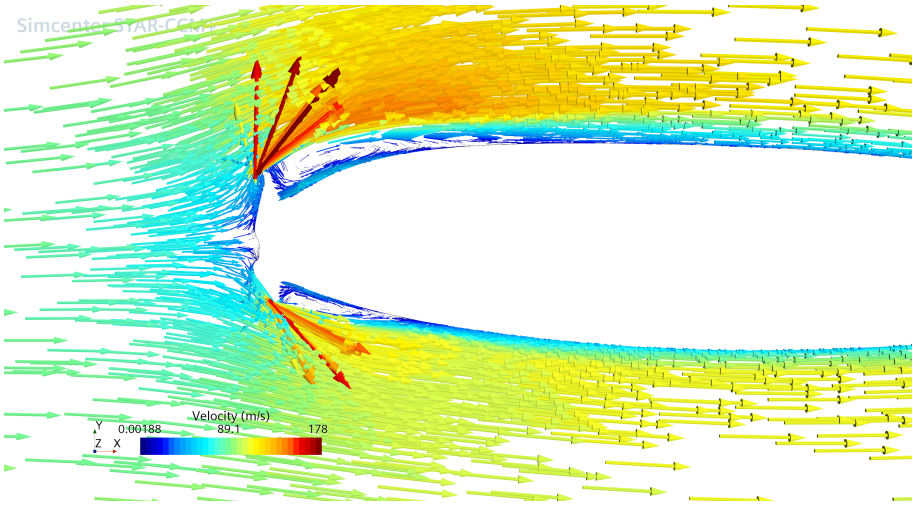

(b) Zoomed view of the leading edge of the velocity vector field over the iced airfoil

Figure 4.23: The velocity vector field around the airfoil in the fast and light 45 minutes holding case

The pressure distributions around the clean and iced airfoil in the fast and light case, obtained from STAR-CCM+ and XFOIL, are viewed in Figure 4.24.

In Table 4.7, the differences in the drag and lift for the fast and light holding scenario are presented.

Table 4.7: The difference in drag and lift coefficient due to icing accretion during 45 minutes holding with a fast and light flight condition

Case	c_d	c_l
Fast and light clean	0.0097	0.2985
XFOIL clean	0.0064	0.3105
Fast and light iced	0.0360	0.2420
Difference [%]	270	-19

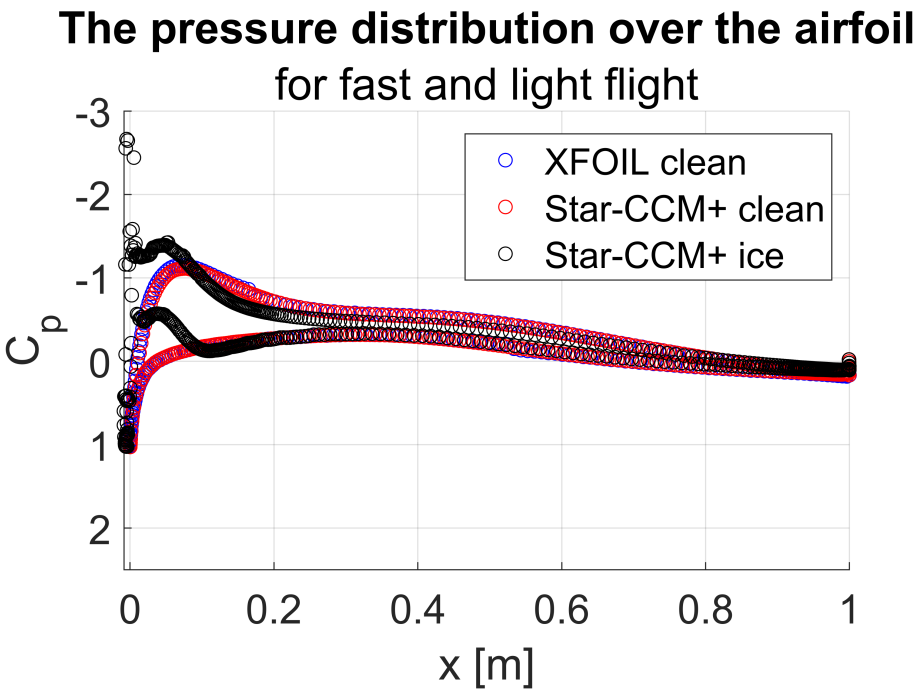

Figure 4.24: The distribution of the pressure coefficient around the airfoil in the fast and light case

A similar iced shape obtained for the fast and light flight scenario was found in Run 072895.05 in [42] and the difference in drag is viewed in Table 4.8.

Table 4.8: The difference in drag coefficient due to icing accretion for the business jet studied in [42]

Case	c_d
Clean	0.0082
Iced	0.0264
Difference [%]	222

5
Discussion

The first part of this chapter includes a discussion about the architecture of the databank and the general methods used in this study. The second part of this chapter involves a discussion regarding the numerical results of the study.

5.1 Discussion of the databank architecture and the general methods

In this study, it was proven that Simulink is a suitable software for modeling and simulation of the airplane. It provides a complete overview of the 6DOF model and a highly modular architecture. Furthermore, Simulink provides functions for e.g., trimming, linearization, and stability analysis, which are useful when performing flight simulations. However, to increase the modularity of the model and to simplify for modifications of the model, it is recommended to implement the aerodynamic databank model through code instead of using Simulink blocks. Also, the aerodynamic databank subsystem, and the methods for estimating the stability derivatives in particular, are faster and more convenient to implement by programming. The compatibility between the aerodynamic databank and the other subsystems of the 6DOF model can be ensured by using the MATLAB Function block in Simulink, which can handle MATLAB code as well as Python code.

Due to relatively unstructured CFD data files, it was not straightforward to read the content of these files in MATLAB. It is therefore recommended to generate the future CFD data in a format that is easy to handle in the postprocessing and by the aerodynamic databank model. The same applies to the geometrical input data, obtained from the CAD model of the airplane. This is of great importance as the airplane design is continuously evolving.

Wind tunnel testing will be performed in order to validate, complement, and increase the accuracy of the CFD data as well as the models in the aerodynamic databank. The wind tunnel experiments complement the CFD simulations in cases when CFD may give low accuracy, e.g., at sharp angles of the geometry, aeroelastic problems, and high angles of attack. Due to the differences in breakdown and coverage between the CFD and wind tunnel data, the aerodynamic databank model cannot automatically be used also for the wind tunnel data. These modifications of the architecture and models of the aerodynamic databank are assigned to future studies.

The component buildup approach was proven to be a qualified method for creating the aerodynamic databank. It was easy to add different aerodynamic effects and analyze these individual contributions to the aerodynamic coefficients. The approach has a relatively low computational cost while maintaining sufficient fidelity. Furthermore, the component buildup approach supports the process of merging the CFD data with aerodynamic models.

The trim function which was developed in parallel with this study is based on a MATLAB function called findopOptions which finds operating points using the gradient descent algorithm. This optimization method requires the entire 6DOF model to be continuous in order to give satisfactory results. Due to this, problems were encountered when running the full 6DOF model, and Simulink blocks such as the saturation block needed to be removed. Regarding the executing time of the 6DOF airplane model simulations, it is important to create a model that is as simple as possible without compromising its fidelity. Extensive use of interpolation and extrapolation algorithms gives longer simulation running times compared to a model containing more data points. On the contrary, large data structs can also be a disadvantage in terms of software performance.

Another problem that was encountered in the development process of the aerodynamic databank model was related to the choice of interpolation method. First, Akima spline was used for interpolation of the lookup tables in the aerodynamic databank model. The Akima spline is a piecewise function consisting of a set of third order polynomials [68]. The slope at the junction points is locally determined under special conditions. It is less sensitive to outliers than other cubic splines which have a tendency to oscillate near an outlier. The objective of this interpolation method is to obtain more accurate curve fitting to curves where the second derivative is rapidly varying. In this study, the Akima spline did not perform well in some interpolations of lookup tables. For consistency and reliability, linear interpolation was globally applied in the lookup tables in the aerodynamic databank model.

Extrapolation of a fitted regression model can lead to wrong and erroneous estimations if the assumed relationship does not hold in the region of extrapolation. For this reason, it can be dangerous to use extrapolation to predict values of data points beyond the range of the given data. In general, all extrapolation made in this study needs to be further validated by e.g., CFD simulations.

An idea for further development of the aerodynamic databank model is to incorporate machine learning and data mining techniques to reduce the computational cost related to aerodynamic analysis. In [69], it was proposed to replace the CFD solver with a surrogate model. It was shown that these techniques are feasible and potentially beneficial for aerodynamic analysis of airplane configurations. In [70], a study involving the application of artificial neural networks for prediction of aerodynamic coefficients was presented. The results proved that an artificial neural network is an efficient method to interpolate across sparse data.

5.2 Discussion of the resulting contributions to the total aerodynamic coefficients

Overall, the output from the aerodynamic databank model gives feasible results. In this section, the contributions to the total aerodynamic coefficients are discussed.

As seen in Figure 4.2, the extrapolation of the drag coefficient curve of the wing, fuselage, and nacelles, respectively, gives realistic behavior for the negative angles of attack. However, the curves of the drag coefficients of the horizontal and vertical tail have less realistic behavior and indicates that additional CFD simulations are required. The curves of the total baseline aerodynamic coefficients, seen in Figure 4.3, have realistic shapes. However, the total pitching moment curve has some relatively sharp turns close to zero angle of attack which indicates that more data points are needed to accurately model the behavior.

Several of the curves of the aerodynamic coefficients that are calculated as functions of the side slip angle exhibit singularities which are unrealistic and a larger number of data points would give a more accurate result. In general, the results of the contributions to the aerodynamic coefficients due to control surface deflections follow the expected behaviors, as described in Chapter 2.

Regarding the results of the modeling of the Mach effect, see Figure 4.8, the total lift and pitching moment coefficients exhibit expected behaviors. It is however expected that the compressibility will have an effect on the total drag coefficient also at negative values of the angle of attack. To evaluate this uncertainty, CFD simulations of negative angle of attack configurations at a relatively high Mach number need to be performed.

As expected, an increase of the power coefficient gives an increase in drag at positive angles of attack, as seen in Figure 4.9b. It also gives a relatively large contribution to the pitching moment, as explained in Section 2.16, and as seen in Figure 4.9c. At high angles of attack, a high power coefficient gives a significant increase of the drag coefficient due to the propeller slipstream, as seen in Figure 4.9a. However, at low angles of attack, the total drag coefficient is decreased. In proximity to the propellers, the drag is reduced due to the increased leading edge suction peaks induced by the propellers. The distribution of the drag around the propellers is essentially distinguished by a lower local drag in the upwash regions of the propellers and a higher local drag in the downwash region. If the former contribution exceed the latter, the total drag of the airplane is reduced.

Regarding the prediction of the changes in drag and pitching moment coefficients due to deployment of the landing gear, the reference areas are estimated based on a few approximate measurements of the landing gear. In order to increase the accuracy of this prediction, it is recommended to calculate the reference areas directly in the computer aided design (CAD) software. The results of the ground effect modeling show, see Figure 4.11, 4.12, and 4.13, that all of the curves exhibit the expected

effects. However, the magnitudes of these effects need to be validated.

The values of the stability derivatives differs more or less between the different estimation methods. The stability derivatives which have similar values from DATCOM, ESDU, and AVL, may have a relatively high degree of statistical significance. However, the DATCOM and ESDU methods are in some cases nearly identical and can be seen as one and the same method. Thus, the results of the validation of the stability derivatives may be deceptive. In other studies, e.g., [71] and [72], DATCOM and AVL have also given values of the stability derivatives that differ up to about 50%. The fuselage and nacelles have not been accounted for when calculating the stability derivatives in this study. Although it is the wing and empennage that gives the largest contributions to the stability derivatives, the disregard of the fuselage and nacelles may give erroneous predictions of the stability derivatives. For this reason, a validation analysis including the effects of the fuselage and nacelles needs to be performed. The true values of the stability derivatives will be determined first once a flight test of the actual airplane is performed. One alternative method for estimating the stability derivatives more accurately is to perform unsteady CFD simulations. Considering the most important stability derivatives, it is recommended to perform CFD simulations to further analyze the values of these.

As mentioned in Section 1.3, the stability analysis based on the stability derivatives was not a part of this study. By only observing the values of the stability derivatives, some conclusions can still be made. The roll damping derivative provides a damping rolling moment as long as it is positive, as mentioned in Section 2.19.2.3. The roll damping derivative has a negative value, as seen in Figure 4.14b, and does not dampen the rolling moment acting on the airplane, indicating that the handling quality requirements may not be fulfilled. In Figure 4.15c, it is seen that the pitch damping derivative takes a large negative value disregarding the angle of attack and the method by which it is calculated. This is desirable in order to obtain a well-damped pitching motion of the airplane such that acceptable stability and control characteristics and handling qualities of the airplane are achieved, as mentioned in Section 2.19.1.3. As stated in Section 2.19.2.4, the yaw damping derivative should have a negative value in order to dampen the Dutch roll motion of the airplane. The value of the yaw damping derivative is indeed negative, as seen in Figure 4.16c. However, the magnitude may preferably be larger to obtaine a sufficient effect on the airplane flying qualities. These conclusions are preliminary and further analysis of the stability derivatives is required.

As seen in Figure 4.21 and Figure 4.24, the surface pressure distributions of clean airfoil configurations obtained from Star-CCM+ agrees well with the results obtained from XFOIL. In both cases, it is observed that the ice accretion gives pressure distributions such that the aerodynamic efficiency of the airfoil decreases. As viewed in Figure 4.20 and Figure 4.23, the ice formations severely disrupt the airflow, resulting in significant performance degradation. In both cases, a wake region is observed behind the ice formation, where the velocity vectors visualize the recirculating flow. The CFD simulations of the iced airfoils are approximate and a higher degree of

resolution is recommended for more reliable results. The icing effect on the 45 minutes holding condition needs further evaluation in terms of comprehensiveness of atmospheric conditions and flight scenarios. The predicted differences in drag and lift due to icing disagree with the experimental values found in [42], particularly in the slow and heavy case. These differences in the predictions of the drag reduction may however be due to the differences in airfoil and ice shapes, as the cases in this study are not completely comparable to the experimental cases.

6
Conclusions

The aerodynamic databank model provides the required aerodynamic forces and moments with sufficient fidelity for analysis of the airplane performance, stability, control, and handling qualities in the conceptual design phase. Utilization of the aerodynamic databank model in the detailed design phase requires validation of the CFD data as well as the fidelity of the selected methods for modeling of aerodynamic effects.

The future work required to validate and increase the accuracy of the aerodynamic databank model primarily involves running additional CFD simulations, particularly of the currently extrapolated data points, the empennage aerodynamic coefficients, the landing gear influence on the aerodynamics, the ice effect, and potentially of the most critical stability derivatives. Wind tunnel experiments also plays an important role in the validation process. Further evaluation of the ice effect, in accordance with the certification requirements, must be conducted. When gathering new aerodynamic data for the aerodynamic databank model, it is important to first establish a suitable and consistent format of the files which will contain the collected data. This will speed up the postprocessing of the aerodynamic data and will simplify the import of the data in the aerodynamic databank model.

As explained in Chapter 5, it is recommended to create the aerodynamic databank model by using code instead of a block diagram. This is a faster way to develop the aerodynamic databank model, increases its modularity, and enables quick changes of the model. To secure reliable communication with the other subsystems in the 6DOF airplane model, it is recommended that the programming language is MATLAB or Python. In the conceptual design phase, the design of the airplane is continuously evolving, and since many methods that are used in the aerodynamic databank model requires geometrical data of the airplane, it is important to impose a simple and reliable procedure to import and update these data.

The wide scope of this master's thesis work in combination with the temporal limitation of five months implicate limitations regarding the details in the modeling and evaluation of the individual aerodynamic effects included in the study. Moreover, an in-depth study of any of these aerodynamic effects would demand highly accurate numerical solutions for the air flow around the airplane. Such analysis could be used for validation of the methods used in this study. To fulfill the aim of this study, the accuracy of individual aerodynamic effects had to be balanced by the comprehensiveness of the aerodynamic databank model as a whole. In conclusion,

the aerodynamic databank model that was developed in this master thesis work can serve as an aid for development of a new airplane.

Bibliography

[1] R. D. Finck, *USAF Stability and control DATCOM*. Wright-Patterson Air Force Base, OH, USA: Air Force Wright Aeronautical Laboratories, 1977.

[2] *ESDU*, 2022. Accessed: May 4 2022. [Online]. Available: https://www.ihsesdu.com/cgi-bin/ps.pl?sess=unlicensed_1220505075900fdh&t=gen&p=home.

[3] B. Graver, K. Zhang, and D. Rutherford, *CO2 emissions from commercial aviation, 2018*. International Council on Clean Transportation, 2018. Accessed on: Jan. 17, 2021. [Online]. Available: https://theicct.org/sites/default/files/publications/ICCT_CO2-commercl-aviation-2018_20190918.pdf.

[4] International Air Transport Association, *Resolution on the Industry's Committment to Reach Net Zero Emissions by 2050*, 2021. Accessed on: Jan. 17, 2021. [Online]. Available: https://www.iata.org/contentassets/dcd25da635cd4c3697b5d0d8ae32e159/iata-agm-resolution-on-net-zero-carbon-emissions.pdf.

[5] Swedavia, *The change is already underway*, Accessed on: Jan. 17, 2021. [Online]. Available: https://www.swedavia.com/the-change-is-already-underway/.

[6] Avinor, *Electric Aviation*, Accessed on: Jan. 17, 2021. [Online]. Available: https://avinor.no/en/corporate/klima/electric-aviation/electric-aviation.

[7] Wayne Durham, *Aircraft flight dynamics and control*, 1st ed. Chichester, United Kingdom: John Wiley Sons, 2013.

[8] *Definition of Streamlines*. NASA Glenn Research Center, Accessed on: May 9, 2022. [Online]. Available: https://www.grc.nasa.gov/www/k-12/airplane/stream.html.

[9] T. A. Talay, *Introduction to the Aerodynamics of Flight*. Hampton, VA, USA: NASA Langley Research Center, 1975. Accessed: May 4 2022. [Online]. Available: https://ntrs.nasa.gov/api/citations/19760003955/downloads/19760003955.pdf.

[10] J. Anderson, *Fundamentals of Aerodynamics*, 6th ed. 2 Penn Plaza, New York, NY, USA: McGraw-Hill Education, 2017. Accessed: May 2 2022. [Online]. Available: https://aviationdose.com/wp-content/uploads/2020/01/Fundamentals-of-aerodynamics-6-Edition.pdf.

[11] *Dynamic Pressure*. NASA Glenn Research Center, Accessed on: May 9, 2022. [Online]. Available: https://www.grc.nasa.gov/www/k-12/airplane/dynpress.html.

[12] N. Hall, *Euler Equations*, 2021. Accessed: May 30 2022. [Online]. Available: https://www.grc.nasa.gov/www/k-12/airplane/eulereqs.html.

[13] N. Hall, *Navier-Stokes Equations*, 2021. Accessed: May 30 2022. [Online]. Available: https://www.grc.nasa.gov/www/k-12/airplane/nseqs.html.

[14] L. Davidson, *Fluid mechanics, turbulent flow and turbulence modeling*. 2022. Accessed: May 16 2022. [Online]. Available: http://www.tfd.chalmers.se/~lada/postscript_files/solids-and-fluids_turbulent-flow_turbulence-modelling.pdf.

[15] J. Roskam, *Airplane Flight Dynamics and Automatic Flight Controls*. Lawrence, KS, USA: Design, Analysis and Research Corporation, 2003.

[16] J. D. Anderson, Jr., *Modern compressible flow*, 3rd ed. Boston, MA, USA: McGraw-Hill, 2002.

[17] T. Snyder and A. Povitsky, *Far-Field Induced Drag Prediction Using VorticityConfinement Technique*, 2014. Accessed: May 3 2022. [Online]. Available: https://www.researchgate.net/publication/272702469_Far-Field_Induced_Drag_Prediction_Using_Vorticity_Confinement_Technique.

[18] *Vortex-lattice utilization*, Hampton, VA, USA, 1976. Accessed: May 3 2022. [Online]. Available: https://ntrs.nasa.gov/api/citations/19760021075/downloads/19760021075.pdf.

[19] M. Drela and H. Youngren, *AVL 3.40 User Primer*, 2022. Accessed: May 4 2022. [Online]. Available: https://web.mit.edu/drela/Public/web/avl/avl_doc.txt.

[20] L. L. Erickson, *Panel Methods - An Introduction*. Moffett Field, CA, USA: NASA Ames Research Center, 1990. Accessed: May 23 2022. [Online]. Available: https://ntrs.nasa.gov/api/citations/19910009745/downloads/19910009745.pdf.

[21] B. L. Stevens, F. L. Lewis, and E. N. Johnson, *Aircraft Control and Simulation: Dynamics, Control Design, and Autonomous Systems*, 3rd ed. Hoboken, NJ, USA: John Wiley Sons, 2015.

[22] *Airplane Flying Handbook*. Oklahoma City, OK, USA: United States Department of Transportation, Federal Aviation Administration, Airman Testing Standards Branch, 2021. [Online]. Available: https://www.faa.gov/regulations_policies/handbooks_manuals/aviation/airplane_handbook/media/00_afh_full.pdf.

[23] R. C. Nelson, *Flight Stability and Automatic Control*. New York, NY, USA: McGraw-Hill Companies, 1998.

[24] J. Roskam, *Airplane Design Part VI: Preliminary Calculation of Aerodynamic, Thrust and Power Characteristics*. Lawrence, KS, USA: Design, Analysis and Research Corporation, 2004.

[25] E. J. Hopkins, *Charts for predicting turbulent skin friction from the van Driest method (II)*. Moffett Field, CA, USA: NASA Ames Research Center, 1972. Accessed: April 29 2022. [Online]. Available: https://ntrs.nasa.gov/citations/19730001588.

[26] D. P. Raymer, *Aircraft Design: A Conceptual Approach*, 6th ed., J. A. Schetz, Ed. Washington, D.C., USA: AIAA, 2018.

[27] L. R. Wootton, *The Effect of Compressibility on the Maximum Lift Coefficient of Aerofoils at Subsonic Airspeeds*, 1967. Accessed: May 11 2022. [Online]. Available: https://www.cambridge.org/core/journals/aeronautical-journal/article/abs/effect-of-compressibility-on-the-maximum-lift-coefficient-of-aerofoils-at-subsonic-airspeeds/3C98204D29AC24F8147C6C250947764F.

[28] S. Gudmundsson, *General Aviation Aircraft Design*, 1st ed. Boston, MA, USA: Butterworth-Heinemann, 2014. Accessed: May 11 2022. [Online]. Available: https://www.sciencedirect.com/science/article/pii/B9780123973085000040.

[29] *Downwash effects on lift*. National Aeronautics and Space Administration Glenn Research Center, Accessed on: Feb. 13, 2022. [Online]. Available: https://www.grc.nasa.gov/www/k-12/airplane/downwash.html.

[30] M. V. Cook, *Flight dynamics principles: a linear systems approach to aircraft stability and control*, 3rd ed. Oxford, United Kingdom: Elsevier Butterworth-Heinemann, 2013.

[31] M. Carley, *Aircraft Stability and Control*. Claverton Down, Bath, United Kingdom: University of Bath, 2017. Accessed: May 4 2022. [Online]. Available: https://people.bath.ac.uk/ensmjc/Notes/stability.pdf.

[32] *CS-23 Amendment 5 and AMC GM to CS-23 Issue 3*. European Union Aviation Safety Agency, 2020. Accessed: Mars 2 2022. [Online]. Available: https://www.easa.europa.eu/downloads/116297/en.

[33] H. S. Fletcher, *Comparison of several methods for estimating low-speed stability derivatives for two airplane configurations*. Hampton, VA, USA: Langley Research Center, 1971. Accessed: May 4 2022.

[34] *Pilot's Handbook of Aeronautical Knowledge*. Oklahoma City, OK, USA: United States Department of Transportation, Federal Aviation Administration, Airman Testing Standards Branch, 2016. [Online]. Available: https://www.faa.gov/sites/faa.gov/files/2022-03/pilot_handbook.pdf.

[35] *ESDU 86021 Introduction to aerodynamic derivatives, equations of motion and stability (including the classical criteria of longitudinal stability and control, and description of the lateral modes of motion)*, 1986. Accessed: May 17 2022.

[36] *ESDU 83026 Contribution of body to yawing moment and sideforce derivatives due to rate of yaw, $(N_r)_B$ and $(Y_r)_B$*, 1983. Accessed: April 25 2022.

[37] T. P. Ratvasky, B. P. Barnhart, and S. Lee, "Current Methods for Modeling and Simulating Icing Effects on Aircraft Performance, Stability and Control," presented at the AIAA Atmospheric Flight Mechanics Conference and Exhibit, Honolulu, HI, USA, Aug. 18-21, 2008. Accessed: Mars 2 2022. [Online]. Available: https://ntrs.nasa.gov/api/citations/20090005992/downloads/20090005992.pdf.

[38] M. K. Politovich, *Encyclopedia of Atmospheric Sciences*, J. R. Holton, J. A. Curry, and J. A. Pyle, Eds. San Diego, CA, USA: Academic Press, 2003. Accessed: Mars 30 2022. Vol. 1, ch. Aircraft Icing. [Online]. Available: https://www.sciencedirect.com/science/article/pii/B0122270908000555.

[39] A. Heinrich *et al.*, *Aircraft Icing Handbook*. Atlantic City International Airport, NJ, USA: Federal Aviation Administration Technical Center, United

States Department of Transportation, 1991. Accessed: April 28 2022. Vol. 1. [Online]. Available: http://www.tc.faa.gov/its/worldpac/techrpt/ct888-1.pdf.

[40] K. J. Finstad, E. P. Lozowski, and L. Makkonen, "On the Median Volume Diameter Approximation for Droplet Collsion Efficiency," *Journal of the Atmospheric Sciences*, vol. 45, no. 24, pp. 4008–4012, 1988. Accessed: Mars 29 2022. [Online]. Available: https://journals.ametsoc.org/view/journals/atsc/45/24/1520-0469_1988_045_4008_otmvda_2_0_co_2.xml?tab_body=pdf.

[41] A. Tafferner *et al.*, "ADWICE: Advanced Diagnosis and Warning System for Aircraft Icing Environments," *Weather and Forecasting*, vol. 18, no. 2, pp. 184–203, 2003. Accessed: Mars 23 2022. [Online]. Available: https://journals.ametsoc.org/view/journals/wefo/18/2/1520-0434_2003_018_0184_aadaws_2_0_co_2.xml?tab_body=pdf.

[42] H. E. Addy Jr., *Ice Accretions and Icing Effects for Modern Airfoils*. NASA Glenn Research Center, Cleveland, OH, USA: Federal Aviation Administration, United States Department of Transportation, 2000. Accessed: April 5 2022. [Online]. Available: https://ntrs.nasa.gov/api/citations/20000044552/downloads/20000044552.pdf.

[43] M. K. Politovich, "Aircraft Icing Caused by Large Supercooled Droplets," *Journal of Applied Meterology*, vol. 28, pp. 856–868, 1989. Accessed: Mars 30 2022. [Online]. Available: https://journals.ametsoc.org/view/journals/apme/28/9/1520-0450_1989_028_0856_aicbls_2_0_co_2.xml?tab_body=pdf.

[44] *Appendix C to Part 25*. Washington, DC, USA: Federal Aviation Administration, United States Department of Transportation, 2022. Accessed: Mars 29 2022. [Online]. Available: https://www.ecfr.gov/current/title-14/chapter-I/subchapter-C/part-25/appendix-Appendix%5C%20C%5C%20to%5C%20Part%5C%2025.

[45] H. E. Addy Jr., *Easy Access Rules for Normal, Utility, Aerobatic and Commuter Category Aeroplanes (CS-23) (Amendment 1)*. European Aviation Safety Agency, 2018. Accessed: April 7 2022. [Online]. Available: https://www.easa.europa.eu/sites/default/files/dfu/CS-23%5C%20Amendment%5C%201.pdf.

[46] A. R. Jones and W. Lewis, *Recommended Values of Meteorological Factors to be Considered in the Design of Aircraft Ice-Prevention Equipment*. Moffett Field, CA, USA: National Advisory Committee for Aeronautics, Ames Aeronautical Laboratory, 1949. Accessed: Mars 29 2022. [Online]. Available: https://ntrs.nasa.gov/api/citations/19930082528/downloads/19930082528.pdf.

[47] C. L. Smalley, *Advisory Circular Certification of Part 23 Airplanes for Flight in Icing Conditions*, K. Smith, Ed. Federal Aviation Administration, United States Department of Transportation, 2007. Accessed: April 7 2022. [Online]. Available: https://www.faa.gov/documentLibrary/media/Advisory_Circular/AC_23.1419-2D_Incl_Chg_1.pdf.

[48] R. S. Sliff, *Advisory Circular Aircraft Ice Protection*. Federal Aviation Administration, United States Department of Transportation, 1971. Accessed: April

7 2022. [Online]. Available: https://www.faa.gov/documentLibrary/media/Advisory_Circular/AC_2--73.pdf.

[49] J.-L. Boiffier, *The dynamics of flight The Equations*. Baffins Lane, Chichester, West Sussex, England: John Wiley and Sons, 1998.

[50] W. Mason, *Program FRICTION*, P. Buller, Ed. Virginia Tech, Blackburg, VA, USA: Virginia Tech Aerodynamics and Design Software Collection, 2006. Accessed: April 29 2022. [Online]. Available: http://www.dept.aoe.vt.edu/~mason/Mason_f/MRsoft.html.

[51] S. Pinzón, *Introduction to Vortex Lattice Theory*, 2015. Accessed: April 29 2022. [Online]. Available: https://www.researchgate.net/publication/314277432_Introduccion_a_la_teoria_VLM_Vortex_Lattice_Theory.

[52] *ESDU 81014 Contribution of wing planform to derivatives of yawing moment and sideforce due to roll rate at subsonic speeds, $(N_p)_w$ and $(Y_p)_w$*, 1981. Accessed: April 20 2022.

[53] *ESDU 83006 Contribution of fin to sideforce, yawing moment and rolling moment derivatives due to rate of roll, $(Y_p)_F$, $(N_p)_F$, $(L_p)_F$, in the presence of body, wing and tailplane*, 1983. Accessed: May 12 2022.

[54] *ESDU Aircraft 06.01.01*, Accessed: April 20 2022.

[55] *ESDU 90010 Pitching moment and lift force derivatives due to rate of pitch for aircraft at subsonic speeds*, 1990. Accessed: April 20 2022.

[56] *ESDU 82017 Estimation of sideforce, yawing moment and rolling moment derivatives due to rate of yaw for complete aircraft at subsonic speeds*, 1984. Accessed: April 20 2022.

[57] *ESDU 72021 Effect of wing on rolling moment due to yawing*, 1972. Accessed: April 20 2022.

[58] *ESDU 71017 Aero-normalized stability derivatives: effect of wing on yawing moment due to yawing*, 1971. Accessed: April 20 2022.

[59] M. B. Bragg and E. Loth, *Effects of large-droplet ice accretion on airfoil and wing aerodynamics and control*. Office of Aviation Research, Washington, DC, USA: Federal Aviation Administration, United States Department of Transportation, 2000. Accessed: April 28 2022. [Online]. Available: https://www.faa.gov/aircraft/air_cert/design_approvals/small_airplanes/icing_protection_systems/faa_documents/media/aceReportAR-00-14.pdf.

[60] R. K. Jeck, *Icing Design Envelopes (14 CFR Parts 25 and 29, Appendix C) Converted to a Distance-Based Format*. Atlantic City International Airport, NJ, USA: Federal Aviation Administration, Airport, Aircraft Safety, Research, and Development, William J. Hughes Technical Center, 2002. Accessed: Mars 29 2022. [Online]. Available: https://www.faa.gov/aircraft/air_cert/design_approvals/small_airplanes/icing_protection_systems/faa_documents/media/acereportar-00-30.pdf.

[61] M. Drela, *XFOIL: An Analysis and Design System for Low Reynolds Number Airfoils*. Heidelberg, Germany: Springer-Verlag, 1989. Accessed: Mars 29 2022. [Online]. Available: https://link.springer.com/chapter/10.1007/978-3-642-84010-4_1.

[62] J. L. Hess and A. M. O. Smith, *Calculation of potential flow about arbitrary bodies*, 1967. Accessed: May 22 2022. [Online]. Available: https://www.sciencedirect.com/science/article/abs/pii/0376042167900036.

[63] B. L. Messinger, *Equilibrium Temperature of an Unheated Icing Surface as a Function of Air Speed*, 1952. Accessed: May 19 2022. [Online]. Available: https://arc.aiaa.org/doi/10.2514/8.2520.

[64] A. Gupta, L. N. Sankar, and R. E. Kreeger, "Application of Extended Messinger Models to Complex Geometries," AeroTech, 2020. Accessed: April 6 2022. [Online]. Available: https://ntrs.nasa.gov/api/citations/20200001854/downloads/20200001854.pdf?msclkid=155e9891b4ec11ec8c17078ad84a5c56.

[65] J. W. Kim *et al.*, "Ice Accretion Modeling using an Eulerian Approach for Droplet Impingement," Grapevine, TX, USA: presented at the 51st AIAA Aerospace Sciences Meeting, Jan. 7-10, 2013. Accessed: April 5 2022. [Online]. Available: https://arc.aiaa.org/doi/pdf/10.2514/6.2013-246.

[66] P. R. Spalart and S. A. Allmaras, "A one-equation turbulence model for aerodynamic flows," presented at the AIAA 30th Aerospace Sciences Meeting and Exhibit, Reno, NV, USA, Jan. 6-9, 1992. Accessed: May 31 2022. [Online]. Available: https://turbmodels.larc.nasa.gov/Papers/RechAerosp_1994_SpalartAllmaras.pdf.

[67] S. A. Allmaras, F. T. Johson, and P. R. Spalart, "Modifications and Clarifications for the Implementation of the Spalart-Allmaras Turbulence Model," presented at the seventh International Conference on Computational Fluid Dynamics (ICCFD7), Big Island, HI, USA, July 9-13, 2012. Accessed: May 31 2022. [Online]. Available: https://www.iccfd.org/iccfd7/assets/pdf/papers/ICCFD7-1902_paper.pdf.

[68] H. Akima, "A new method of interpolation and smooth curve fitting based on local procedures," *Journal of the Association for Computing Machinery*, vol. 17, no. 4, pp. 589–602, 1970. Accessed: Feb 25 2022. [Online]. Available: https://doi.org/10.1145/114697.116810.

[69] C. Paulete-Periáñez, E. Andrés-Perez, and C. Lozano, "Surrogate modelling for aerodynamic coefficients prediction in aeronautical configurations," presented at the 8th European Conference for Aeronautics and Space Sciences, Madrid, Spain, July 1-4, 2019. Accessed: May 31 2022. [Online]. Available: https://ntrs.nasa.gov/api/citations/20030022753/downloads/20030022753.pdf.

[70] T. Rajkumar and J. Bardina, "Prediction of Aerodynamic Coefficients using Neural Networks for Sparse Data," presented at the 15th International Florida Artificial Intelligence Research Society Conference, Pensacola, FL, USA, May 14-16, 2002. Accessed: May 31 2022. [Online]. Available: https://ntrs.nasa.gov/api/citations/20030022753/downloads/20030022753.pdf.

[71] D. Royer, "Design of an Automatic Landing System for the Meridian UAV using Fuzzy Logic," MSc thesis, University of Kansas, 2010. Accessed: May 26 2022. [Online]. Available: https://kuscholarworks.ku.edu/bitstream/handle/1808/6290/Royer_ku_0099M_10895_DATA_1.pdf?sequence=1&isAllowed=y.

[72] V. Cipolla, K. Abu Salem, and F. Bachi, "Method for preliminary stability analysis of PrandtlPlane aircraft in subsonic conditions," presented at the 7th EASN International Conference on Innovation in European Aeronautics Research, Warsaw, Poland, Sep. 26-29, 2017. Accessed: May 26 2022. [Online]. Available: https://www.researchgate.net/publication/321759656_METHOD_FOR_PRELIMINARY_STABILITY_ANALYSIS_OF_PRANDTLPLANE_AIRCRAFT_IN_SUBSONIC_CONDITIONS.

DEPARTMENT OF SOME SUBJECT OR TECHNOLOGY
CHALMERS UNIVERSITY OF TECHNOLOGY
Gothenburg, Sweden
www.chalmers.se

CHALMERS
UNIVERSITY OF TECHNOLOGY